Exploitation and Mitigation of Multipath in Complex Wave Propagation Environments for Target Detection, Tracking, and Communication

by

Fikadu Tafes Dagefu

A dissertation submitted in partial fulfillment
of the requirements for the degree of
Doctor of Philosophy
(Electrical Engineering)
in The University of Michigan
2012

Doctoral Committee:

Professor Kamal Sarabandi, Chair
Professor David R. Dowling
Associate Professor Anthony Grbic
Professor Eric Michielssen
Associate Research Scientist Adib Y. Nashashibi

To the memories of my parents, Ayalnesh Gessesse and Tafes Dagefu,
and my nephew Ebenezer Deribe.

ACKNOWLEDGEMENTS

I am blessed to have a very loving and supportive family. I would like to thank my parents for their sacrifices and for instilling in me at an early age the value of education and hardwork. I would like to thank my brothers and the rest of my family, Shiferaw Dagefu, Deribe Dagefu, Woubishet Dagefu, Melaku Dagefu, Ebenezer Deribe, Kidist Tesfaye, Sirgut Abate,Yanet Deribe, Yeabtsega Woubishet and Abigail Woubishet for their love and support. Without them, I would not be where I am today.

I have had the privilege of working with my research advisor and dissertation committee chair Dr. Kamal Sarabandi. I want to thank him for his continuous support, invaluable guidance and mentorship. Needless to say, I have benefited greatly from his seemingly endless knowledge and passion for research. I would also like to thank the rest of my thesis committee, Dr. Eric Michielssen, Dr. David R. Dowling, Dr. Anthony Grbic and Dr. Adib Nashashibi for their insightful suggestions in the completion of this work. I also want to thank Dr. Leland Pierce for his advise and help. Dr. Mircea D. Driga who taught me my first course in Electromagnetics at the University of Texas at Austin and all my teachers at my previous schools deserve my sincere thanks.

I would like to express my appreciation to my friends and colleagues at the University of Michigan. I especially want to thank Dr. Jungsuek Oh, Dr. Adel Elsherbini, Dr. DaHan Laio, Dr. Michael Thiel, Dr. Juseop Lee, Dr. Mehrnoosh Vahidpour, Dr.

Jacquelyn A. Vitaz, Dr. Wonbin Hong, Dr. Farhad Bayatpur, Dr. Amelia Burkle, Dr. Mojtaba Dehmollaian, Dr. Arezou Edalati, Dr. Xueyang Duan, Dr. Yuriy Goykhman, Dr. Mark Haynes, Dr. Scott Rudolph, Dr. Alireza Tabatabaeenejad, Dr. Lin Van Nieuwstadt, Dr. Onur Bakir, Dr. Xinen Zhu, Dr. Morteza Nick, Dr. Felipe Valdes, Dr. Jia-Shiang Fu, Dr. Chih-Hao Kuo, Michael Benson, Young Jun Song, Meysam Moallem, Hatim Bukhari, Sangjo Choi, Mani Kashanianfard, Hamid Nejati, Jiangfeng Wu, Jihun Choi, Armin Jam, Amr Ibrhaim, Morteza Sheikhsofla, Amit Patel, Mohammadreza Imani, Gurkan Gok, Pelumi Osoba, Luis Gomez, Abdulkadir Yucel, Victor Lee, Waleed Alomar, Mariko Burgin, Jane Whitcomb, Ruzbeh Akbar, Chris Berry, Ning Wang, Tolga Yardimci and Abdi M. Zeynu. I also want to thank Xi Lin and Megan J. Roberts for reviewing parts of this thesis.

I have been fortunate to have many wonderful people around me including all SMES-G members and all my friends in the Ann Arbor area. I want to especially thank Emuye Asfaw, Dereje Gessese, Rahel Gebremedhin, Aklilu Tizazu, Berhangebriel Asefa, Betrework Tizazu, Fikadu Gessesse, Ermias Tesfagiorgis, Yonas Tefera, Yared Tefera, Yohannes Yoseph and Yohanes Giday.

Finally, I want to thank US Army research laboratory and MIT Lincoln laboratory for their financial support that made it possible to carry out the work presented in this thesis.

TABLE OF CONTENTS

LIST OF FIGURES

Figure

LIST OF TABLES

Table

LIST OF APPENDICES

Appendix

CHAPTER I

Introduction

1.1 Motivation

State-of-the-art systems that are used for detection, tracking and communication applications have many drawbacks when such systems are utilized in complex and highly cluttered environments. As an example, Global Positioning System (GPS) either completely fails or have very poor resolution under foliage, indoors, inside tunnels and in highly cluttered urban environments. Also, for power limited ad hoc wireless networks in complex propagation environments, various phenomena including multipath, attenuation, diffraction from sharp corners and edges and scattering from other obstacles contribute to the fading and distortion of electromagnetic waves that severely limit the coverage and reliability of the wireless service. The signal that arrives at a receiver, for a wireless system operating in such environment, is the sum of the direct path between transmit(Tx) and receive(Rx) antennas attenuated by penetrable objects as well as signal components scattered by nearby obstacles. Because of the difference in path length among the various signal components and in the absence of a direct signal, the received electric field will have uneven spatial distribution and significant fluctuations. This phenomenon is called fast fading and results in intermittent signal drop-off causing the communication channel to be unreliable.

The work presented in this thesis considers two classes of challenging problems. The first focus of the work pertains to developing radio frequency (RF) based techniques that exploit and/or mitigate the effect of scattering from surrounding obstacles in the environment of interest for localization, tracking and communication applications in indoor and urban environments. The second problem of interest is related to the detection and localization of buried targets. In this case radar based schemes which utilize electromagnetic waves scattered by the object in the presence of other scatterers surrounding the object are more appropriate. It should be noted that in this thesis detection refers to the ability to determine whether there is a target or not.

An ensemble of small robotic platforms deployed in complex propagation environments as depicted in Fig. 1.1 can be used to describe the various aspects of the work. The envisioned system consists of robotic platforms which are equipped with miniaturized antennas for sensing, navigation and communication purposes. The robotic platforms could be flyers and crawlers (deployed in indoor and urban environments for various military and civilian applications) and robotic rovers (for subsurface detection and localization of buried objects). In addition to the challenges associated with the presence of clutter, the fact that the antennas in such systems are very close to the ground ($\leq \lambda$ above ground) presents another challenge since conventional propagation modeling approaches such as Ray tracing have significant inaccuracies when used for near-ground propagation characterization. Localization and tracking approaches based on RF signals transmitted by a miniaturized antenna integrated on the object of interest could be useful for applications such as robot-assisted fire and earthquake rescue missions, user position estimation in mobile communications and for security systems. A vital military application includes enhancing tactical sit-

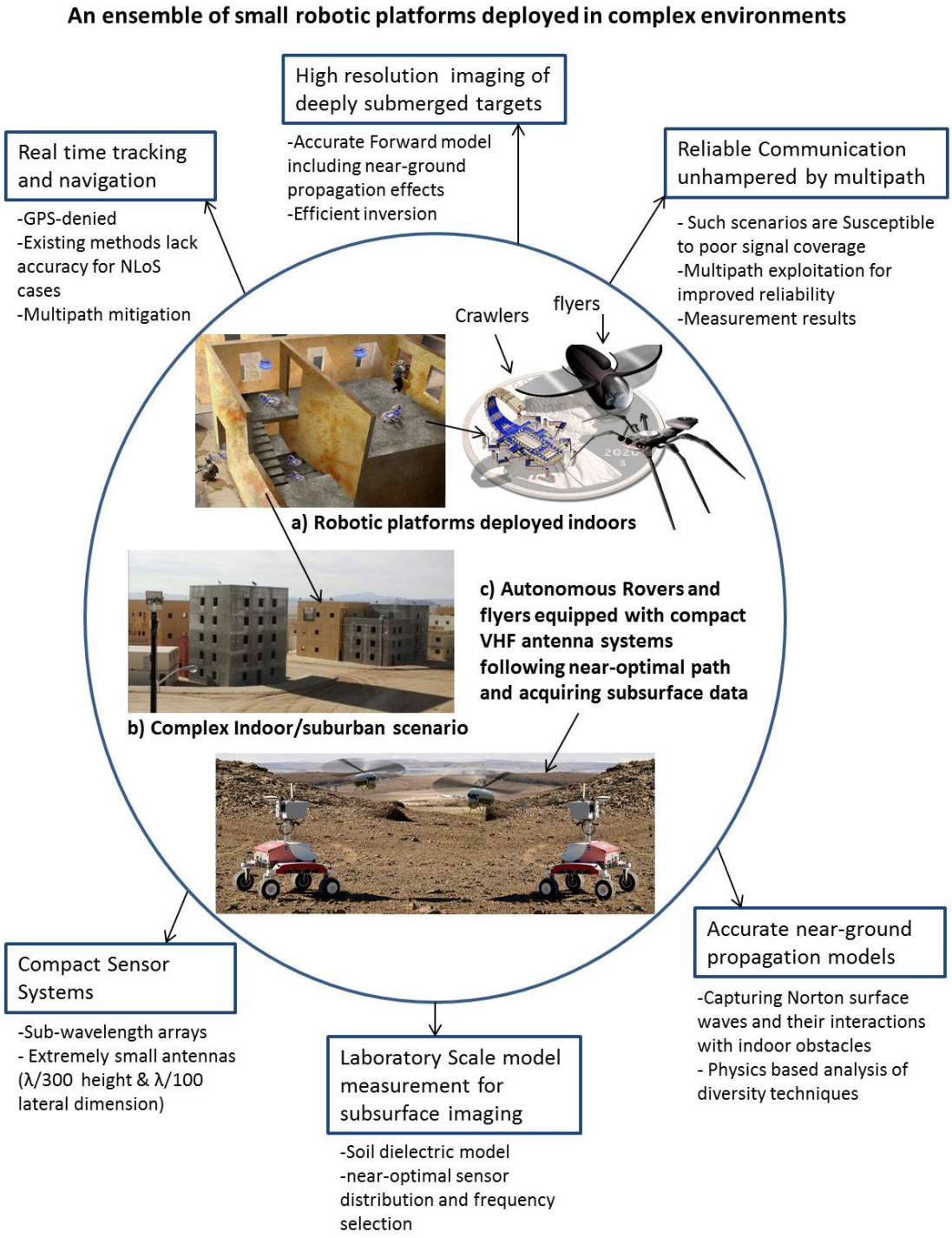

Figure 1.1: An ensemble of very small robotic platforms(e.g. flyers,crawlers) equipped with miniaturized sensors deployed in complex propagation scenarios for Military (intelligence gathering, situational awareness in urban warfare) or civilian applications (rescue missions,monitoring hazardous environments, Images borrowed from [4]-[5]

uational awareness in urban warfare. One specific application of interest pertains to assisting the aforementioned robotic platform in real-time high-resolution navigation in these cluttered environments.

High resolution subsurface detection and imaging techniques are sought for various military and homeland security applications including the detection of landmines, Unexploded Ordnance (UXO), clandestine tunnels and weapons facilities. The detection of buried pipelines, wires and cables, and rescue missions under collapsed buildings are examples of civilian applications. In many scenarios, the depth of the various targets that need to be localized could vary from a few centimeters for shallow targets (e.g. landmines) to several meters for targets that are deeply-submerged (tunnels,UXO, etc.). The challenge with detecting shallow targets mainly has to do with the fact that the air-ground reflection will make it difficult to isolate the signal scattered by the target [1]-[3]. Due to soil inhomogeneity and soil moisture content, electromagnetic signals (especially at high frequencies) experience significant attenuation, reflection and scattering in subsurface environments making the detection/imaging of deeply submerged targets difficult. Traditional ground penetrating radars (GPRs) do not provide adequate imaging resolution and/or sufficient depth which renders them of limited use in the considered applications.

As it was alluded to earlier, the approaches pursued in this work are primarily intended for applications in complex propagation and scattering environments for which the Tx and Rx antenna heights maybe a fraction of the wavelength. This entails developing efficient and accurate propagation and scattering models for near-ground sensors deployed in complex environments including indoor, urban and subsurface environments. In the first part of this work an efficient semi-analytic propagation model that fully accounts for near-ground propagation effects and their inter-

actions with indoor scatterers such as building walls and furniture is proposed. Such a model is useful because existing ray tracing routines which are commonly used for indoor field prediction, are inadequate for evaluating signal coverage of transceiver nodes close to the ground ($< \lambda$ above ground) since such routines neglect higher order surface waves and are inadequate to treat finite-sized and possible irregular-shaped obstacles at VHF and UHF bands. The proposed model addresses these issues and has been validated by full-wave simulation results and laboratory measurements. An accurate scattering model for a target buried in realistic subsurface environment, modeled as a vertically stratified medium is also presented.

In the second part of this work, a sub-wavelength source tracking system utilizing highly miniaturized antennas in the HF range for applications in GPS-challenged environments including indoor and urban scenarios is proposed. The propagation model described above and other numerical models are used to investigate wave propagation and scattering in complex indoor scenarios as a function of frequency and to validate direction finding in the HF range in multipath environments. At such low frequencies, accurate measurement of the phase difference between the signals at the Rx antenna elements having very small baseline is challenging. To address this issue, a biomimetic circuit that mimics the hearing mechanism of a fly (Ormia Ochracea) is utilized to ease the measurement of small phase differences. A system prototype is realized and tested in realistic environments.

In the third part of the work, a high resolution subsurface imaging technique for detection and localization of deeply submerged targets is proposed. The approach is based on distributed near-ground sensor networks that utilize ultra-wideband waveforms in the Very High Frequency (VHF) range. The subsurface scattering model alluded to earlier is utilized as a forward model. Also, an efficient inversion technique

that uses ultra-wideband near-field focusing is proposed. Numerical models and a laboratory scaled model measurements are used for validation and analysis.

In the last part of the work, a new physics-based technique to analyze antenna diversity systems is proposed. The approach takes into account the complex radiation pattern of the Tx and Rx diversity antenna systems in conjunction with an accurate, deterministic, coherent, and polarization preserving propagation model for a complex multipath scenario. The approach is utilized to investigate advantages offered by a common aperture pattern diversity antenna systems. A co-located, compact radiation pattern diversity system prototype is realized and characterized by the proposed technique as well as measurement results and the improvement in channel reliability is quantified via complex correlation coefficient and diversity gain.

1.2 Previous work

1.2.1 Indoor Wave Propagation Models

Electromagnetic field prediction models for indoor and urban environments have several applications including wireless channel characterization, radar through-wall imaging and distributed sensor networks for environmental and subsurface sensing [7]-[8]. Through-wall imaging and detection techniques, which have applications in many areas including fire and earthquake rescue missions and security systems (detection of intruders), often require a fast and accurate forward model which takes into account scattering from indoor obstacles. Another application pertains to positioning and tracking of robotic platforms deployed in complex environments including urban and indoor scenarios for military applications to enhance tactical situational awareness. A specific example of this is assisting the aforementioned platform in high-resolution navigation. There are also other military applications including sensor networks deployed in the battlefield for communications between soldiers on the

ground. Examples of such systems that researchers have been working on include the Self-Healing Minefield (SHM) system sponsored by U.S. Defense Advanced Research Projects Agency(DARPA) [9] which is an anti-vehicle landmine system that utilizes a networked communication among the various mines and the Networked Embedded Systems Technology (NEST) which is also a DARPA program intended to be deployed in various environments [10]. The antennas used in such systems are often very close to the ground. For example, the antenna height of the SHM system is 7 cm [11]. One of the main goals of this thesis is to present an indoor wave propagation model that accurately captures the Norton surface waves that are dominant at low transceiver heights.

In the literature, various indoor field prediction models have been presented. Ray tracing routines are used as the primary methods to predict field coverage in indoor and urban settings [12]-[22]. In [23], a hybrid technique that combines a full-wave approach with ray tracing is developed. In [24], a path loss prediction model that utilizes a parabolic approximation of the Helmholtz equation is proposed. There are also various high-frequency techniques including the Geometrical theory of diffraction (GTD) and Uniform theory of diffraction (UTD) that are devised to include diffraction effects from edges and corners [25]-[27]. Geometrical optics alone does not take into account finiteness and possible irregularities of building walls and other indoor scatterers. This is because of the inherent assumption used when the Fresnel reflection and transmission coefficients are derived in which the building wall is treated as an infinite homogeneous dielectric slab.

Several researchers have focused on developing indoor field prediction models that are based on measurement results especially for lower frequency applications [28]-[34]. Although models based on measurement could give a more accurate estimate

of the received field compared to ray tracing routines, the drawback of such models is the fact that they are site-specific and hence are not versatile. Also, developing a measurement-based model is expensive and does not provide insight into the various scattering mechanisms. Pure numerical solvers that are based on methods such as Method of Moments(MoM),Finite element method (FEM),Finite-difference time-domain (FDTD), etc. are usually not preferred due to the high computational cost resulting from the large size of realistic indoor propagation scenarios in terms of wavelength. These methods are limited to low frequencies and small building scenarios and require high-performance computers. Furthermore, the existing models including the various ray tracing and hybrid techniques are inadequate for evaluating the signal coverage for near-ground networks since the scattered wave from the ground is only approximated by using the Fresnel reflection coefficient neglecting the higher order Norton surface waves.

1.2.2 Source tracking in Multipath Environments

Available techniques for direction finding that are based on time-of-arrival (TOA), time-difference-of-arrival (TDOA) and received signal strength indicator (RSSI) often involve complex algorithms [35]-[41]. TOA and TDOA based approaches also have an inherent issue associated with clock drift [41]. Angle of arrival (AOA) based methods are relatively simple (with some complexity related to antenna calibration) and can be reliably used to determine the direction of a source [42]-[43]. Hybrid approaches that combine AOA and TDOA techniques have also been reported [44]-[45]. In GPS-denied environments such as indoor and urban scenarios the task of localizing and tracking an RF source is even more challenging because of multipath. The level of multipath increases significantly at frequencies utilized in conventional wireless systems (2-5GHz range) or even in the VHF range compared to the HF band

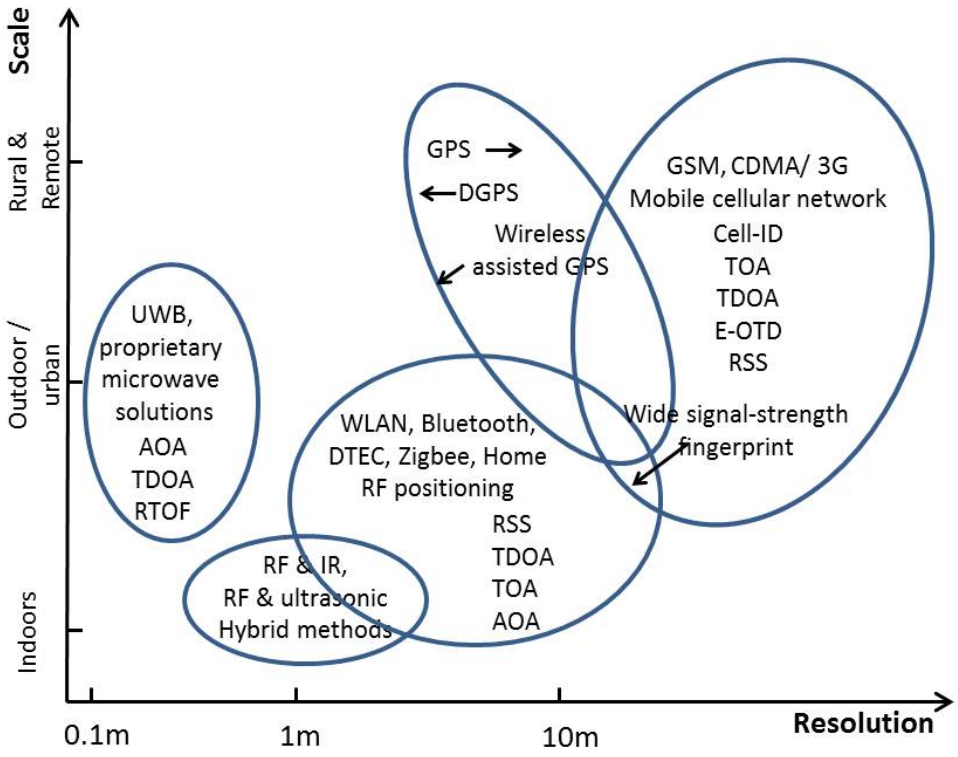

Figure 1.2: Available Indoor localization and positioning systems, diagram borrowed from [39]

[46]-[47]. Given a Tx and Rx antenna system located in a multipath environment, the signal at the Rx antenna consists of the direct, reflected, diffracted and multiply scattered components from the objects within the environment. The path lengths of multiply scattered fields can be quite different from other field components (direct). A full-wave analysis of multipath levels in indoor scenarios is presented in chapter III. Several researchers have worked on ultrawideband (UWB) systems and different signal processing algorithms for non-line-of-sight (NLOS) source localization [48]-[51]. Other approaches include Vision-based position estimation and tracking based on sensors integrated in the environment itself [52]-[53].

1.2.3 Subsurface Imaging

Since the invention of Radar (RAdio Detection And Ranging) before World War II, Scientists have made great strides in the last century developing highly sophisti-

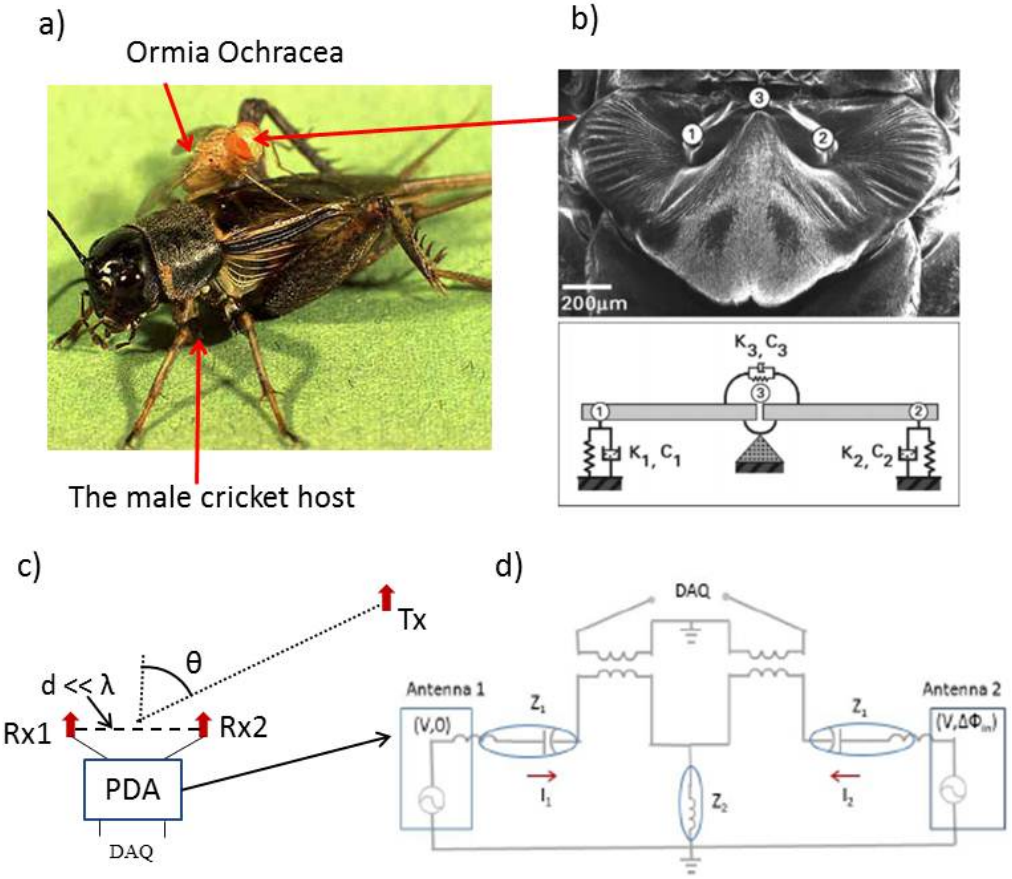

Figure 1.3: Ormia uses a pair of mechanically coupled ears to localize the male cricket using the crickets chirp (4.8KHz). Finding a host cricket is vital for the fly′s survival. Ormia′s directional accuracy is about 2°(similar to a human ear). Ormia′s ears are separated by 1.2mm ($\lambda/60$ at 4.8KHz) . The figure shows: a) the Parasitoid fly Ormia Ochracea and its cricket host, b) Ormia′s coupled ears and its mechanical model, and c) a schematic of the electrical analogous of Ormia′s coupled ears showing the use of a phase difference amplification (PDA) circuit and d) a first order circuit realization of the PDA circuit that mimics Ormia′s coupled ears utilized in the system presented in Chapter III[Images in a) and b) are from [93]].

cated radar based systems for a variety of civilian and military applications. Today, such systems are being used in air traffic control, weather prediction, radar astronomy, air-defense and antimissile systems. Another application of interest is in the area of subsurface imaging. While it is possible to image planets, stars and galaxies with relatively high resolution, imaging even a few meters into the earth has proven to be very difficult. A significant amount of work has been devoted towards development of various techniques to image targets and underground structures by making use of electromagnetic signals including active sensor systems such as GPR and passive sensors such as magnetometers [54]-[63]. Other techniques include electro-optical infrared sensors and electromagnetic induction (EMI) [64]. Several researchers have focused on developing hardware and signal processing for mono-static and bi-static radar systems for subsurface detection. In [65], a multi-static GPR system using beamforming is presented. Other researchers developed various inversion algorithms and carried out experiments for multi-static imaging systems [66]-[70]. In many of the current approaches, the inefficiencies include poor resolution, high false alarm rates caused by man-made or naturally occurring clutter, and challenges associated with detecting deeply submerged targets. It should also be noted that many of the available techniques are not ideal for quick detection in large areas contaminated with mines or UXO. One area that is seldom addressed has to do with the optimal distribution of the sensors or receiving points. Basically, given N number of sensors along with the choice of polarization for each sensor, the goal becomes how to best arrange the sensors to cover the largest possible area while achieving the best resolution and minimizing the direct coupling among transmitting and receiving antennas.

1.2.4 Diversity Systems

An aspect of wireless communication that is of paramount importance is reliable connectivity unhampered by signal fading caused by scatterers such as walls, buildings and other obstacles. As mentioned before, an inherent challenge associated with indoor communication channels is fast fading which results in intermittent signal drop-off making the communication channel unreliable. A viable approach to mitigate fast fading is the use of antenna diversity systems. Antenna Diversity is a communication method utilizing multiple antennas to receive and/or transmit signals to capture statistically independent copies of the signal to compensate for the multipath interferences.

In the literature, there are five different types of diversity techniques that can be used to improve channel reliability: spatial, temporal, polarization, frequency, and radiation pattern. Of these, only spatial, polarization and pattern make for a practical implementation in WLAN antenna systems. In [71], an analysis of a spatial diversity system based on simulations and measurements is presented. The performance of a dual-antenna handset for which different antenna types were utilized is investigated with particular focus on industrial, scientific, and medical (ISM) band [72]. In [73], a test system to experimentally determine the complex correlation coefficient between two antenna branches is proposed and was utilized to evaluate the polarization diversity performance of different antenna pairs in Rayleigh and Rician distributions which are often used to model indoor environments. In [74], experiments where antenna separation, polarization, and pattern were varied independently were carried out and the performance of the diversity system is analyzed. Other researchers have also reported analysis results of various diversity systems based on measurement and stochastic indoor propagation models [75]-[78]. For small wireless devices, spatial

diversity scheme is not an option due to limited space on such devices. In a highly multipath environment where signal fading is strong and signal's direction of arrival to the receiver is diverse, radiation pattern diversity is most suitable. Radiation diversity often refers to antenna systems composed of two or more arrays with beams pointing in different directions to collect statistically independent rays arriving from different directions. Again for small wireless platforms such solution is not appropriate. Small common aperture antennas with multiple feed that can produce almost orthogonal radiation patterns are envisioned for these applications [79].

1.3 Dissertation Overview

The dissertation explores various Radio frequency based techniques that exploit and/or mitigate multipath effects in complex propagation and scattering environments for target detection, tracking and wireless communication applications. This entails developing efficient and accurate propagation and scattering models for near-ground sensors deployed in complex environments including indoor and subsurface environments. A block diagram summarizing the various components of the work is given in Fig. 1.4. Following is an overview of each chapter in more detail.

Chapter II: Near-ground Wave Propagation Model for Indoor Scenarios

This chapter presents an efficient semi-analytic model for near-ground wave propagation in indoor scenarios is presented. For transceivers deployed in indoor environments on or near the ground, since RF wave propagation is dominated by Norton surface waves, these higher order waves and their interactions with building walls and other indoor obstacles have to be captured for accurate field calculations. Existing ray tracing routines which are commonly used for indoor field prediction, are inad-

equate for evaluating signal coverage of transceiver nodes very close to the ground (less than a wavelength above ground) since such routines neglect higher order surface waves. In addition, geometrical optics alone is inadequate to treat finite-size and possible irregular-shaped obstacles at low radio frequencies (VHF and lower UHF). Our approach for calculation of near-ground wave propagation and scattering is based on a hybrid physical optics and asymptotic expansion of dyadic Green's function for a half-space dielectric medium. Equivalence principle in conjunction with physical optics approximation is utilized to handle scattered field from building walls which are the dominant scatterers in indoor settings. The proposed approach is validated for various indoor propagation scenarios by using both measurement results and full-wave numerical solvers.

Chapter III: Sub-wavelength Source Tracking in GPS-challenged Environments

In this chapter, a Sub-wavelength source tracking system utilizing highly miniaturized antennas in the HF range for applications in GPS-denied environments including indoor and urban scenarios is proposed. A technique that combines a high resolution direction finding and radio triangulation utilizing a compact transmit (Tx) and receive (Rx) antenna system is pursued. Numerical models are used to investigate wave propagation and scattering in complex indoor scenarios as a function of frequency. We choose HF band to minimize attenuation through walls and multipath in indoor environments. In order to achieve a compact system, a low-profile and highly miniaturized antenna ($\lambda/300$ height and $\lambda/100$ lateral dimensions at 20MHz) having omnidirectional, vertically polarized field is designed. At such low frequencies, accurate measurement of the phase difference between the signals at the Rx antennas having very small baseline is challenging. To address this issue, a biomimetic cir-

cuit that mimics the hearing mechanism of a fly (Ormia Ochracea) is utilized (See Fig. 1.3). With this circuit, very small phase differences are amplified to measurable values. The numerical simulations are used to analyze direction of arrival retrieval and source localization in highly cluttered environments. A compact system prototype is also realized and source tracking in complex indoor scenarios is successfully demonstrated.

Chapter IV: Subsurface Imaging based on Distributed Near-ground Sensors

This chapter discusses a high resolution subsurface imaging technique based on distributed near-ground sensor networks that utilizes ultra-wideband waveforms in the Very High Frequency (VHF) range is presented. An accurate scattering model for a target buried in realistic subsurface environment, modeled as a vertically stratified medium,is presented first. Then an inversion technique that uses ultra-wideband near-field focusing is described. The signal penetration depth as a function of frequency and various subsurface parameters is calculated based on the developed forward model. The imaging resolution as it relates to the accuracy of background retrieval is also analyzed. A semi-empirical soil dielectric model that was originally developed for the Ultra High Frequency (UHF) band is modified and validated at the VHF range with measured results available in the literature. For a given soil textural composition and frequency, the model predicts the real and imaginary parts of the dielectric constant as a function of volumetric moisture content (MV) of soil. This soil dielectric model is utilized to make the inversion more efficient. To address the challenge associated with the design of compact and ultra-wideband VHF antennas, a scheme utilizing multiple antennas and reduced number of frequency points is proposed. The sensor arrangement both in terms of spatial distribution and polarization

of each antenna as it relates to the lateral resolution as well as minimizing the direct coupling between the Tx and Rx antennas is analyzed. The proposed subsurface imaging approach is validated based on numerical techniques and a laboratory scale model measurement results.

Chapter V: Measurements and Physics-based Analysis of Co-located Antenna Pattern Diversity System

The focus of this chapter is to investigate the advantages offered by radiation pattern diversity using a new physics-based diversity analysis technique and measurement results. Unlike techniques that utilize polarization and/or spatial diversity, radiation pattern diversity offers a unique opportunity to achieve compact diversity antenna systems especially with the advent of enabling antenna miniaturization techniques. In this work, a co-located antenna radiation pattern diversity system is proposed and its performance is analyzed using an accurate physics-based diversity analysis technique. The proposed analysis technique utilizes an efficient deterministic propagation model modified by incorporating the complex gain of the Tx and the complex effective height of the Rx antennas into the rays launched and received by the antennas in a coherent manner. The proposed system is realized and tested in complex indoor scenarios based on which complex correlation coefficients between various channels and the effective diversity gain are computed to quantify the improvement in channel reliability.

The thesis concludes by summarizing the academic contributions of the work and discussing possible future work related to the topic.

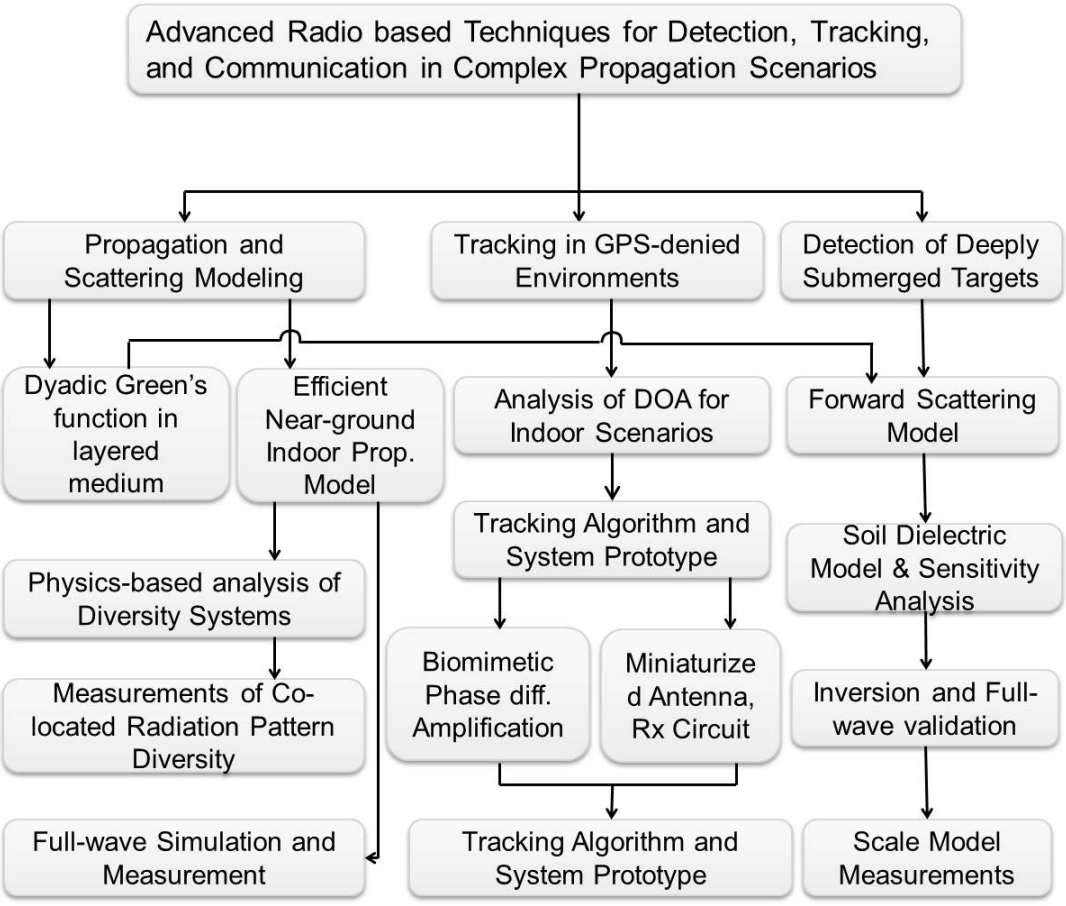

Figure 1.4: Thesis flowchart.

CHAPTER II

Near-ground Wave Propagation Model for Indoor Scenarios

2.1 Introduction

In this chapter, an efficient semi-analytic near-ground wave propagation model for indoor scenarios is proposed. The method is based on asymptotic behavior of dyadic Green's function for a half-space dielectric in conjunction with a physical optics approximation to handle scattered field from various indoor obstacles. Dielectric building walls, which are the most commonly encountered features in indoor and urban settings, are modeled as dielectric blocks whose effective dielectric constants are calculated based on the electromagnetic characteristics of the building materials. The field scattered by building walls and other indoor obstacles that are in the line of sight of the transmitter is computed by first approximating the total fields inside the dielectric medium using physical optics and then applying equivalence principle. The dielectric scatterers are then replaced by polarization currents which are used to calculate the first order scattered field. Geometric optics in conjunction with the Green's function is used to account for multiple reflections from the shadowed walls up to any desired order.

In the following sections, we describe the proposed approach and discuss how the

various components of the electric field are calculated in 2D for a simple wall-ground geometry followed by the extension of the 2D model to 3D multi-wall scenarios. The implementation and validation of the proposed technique by using numerical solvers followed by the comparison of Norton waves and the scattered field component from furniture are discussed. Also, time-domain analysis of the received field, which is useful to get an insight into the various scattering mechanisms, is presented. The accuracy and computational efficiency of the proposed technique is compared to that of ray tracing and a full-wave solver. Finally, measurement results from controlled laboratory measurements are used to further investigate the accuracy of the proposed technique. In all the formulations and discussions to follow e^{iwt} time variation convention is assumed.

2.2 Norton Surface waves

As it was alluded to in the previous section, for near-ground transceivers even without the presence of building walls, wave propagation is dominated by the Norton surface waves due to the near cancelation of the direct field with the GO reflected field (see Fig. 2.1), which are the first two terms in equation (2.1). The third term is particularly important at lower RF bands for ad hoc communication scenarios.

$$E_{total}^{No\ wall} = E_{direct} + E_{reflected}^{GO} + E_{ground}^{Norton} \tag{2.1}$$

Since Norton waves vary as a function of the sum of the heights of the Tx and Rx antennas, the ratio of the Norton waves to the GO components ($E_{direct} + E_{reflected}^{GO}$) is plotted against the sum of the transmitter height and receiver height (zs+zo) in terms

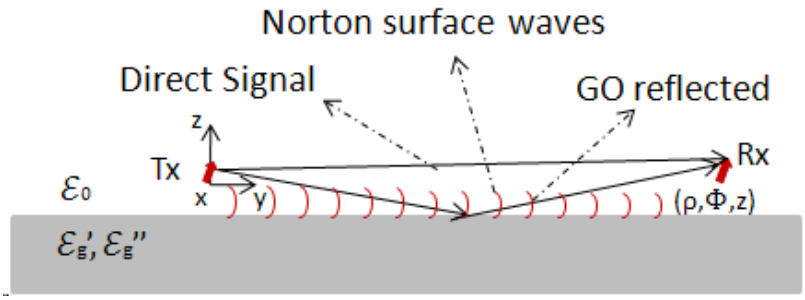

Figure 2.1: A schematic of a near-ground Tx and Rx antennas on top of a dielectric half-space showing the direct, the GO-reflected and the Norton surface waves.

of wavelength as can be seen in Fig. 2.2. It should be noted that, $'zo + zs'$, shown in terms of wavelength (in the X-axis), is calculated independently for each frequency. So, when the curve for the 30 MHz case is plotted, it's against the height in terms of wavelength at 30MHz. The curves for the other frequencies are plotted in a similar fashion. As can be seen in the plot, the Norton waves are dominant independent of frequency as long as the transceiver height is small in terms of wavelength. The slight variation in the ratio (E_{NW}/E_{GO}) is caused by the change in the imaginary part of the dielectric constant as a function of frequency.

Based on the above analysis, we see that the higher order Norton waves and their interactions with building walls and other indoor obstacles have to be taken into account for accurate field calculation. Despite the extensive research that has been carried out recently in the area of indoor field prediction modeling, to our knowledge, an accurate and computationally efficient technique that fully takes into account these higher order Norton waves and can be applied for characterizing near-ground wave propagation especially in indoor scenarios is not available.

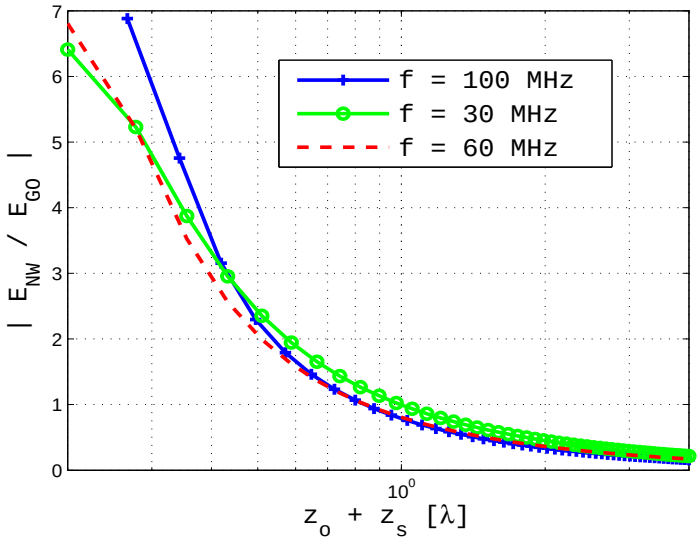

Figure 2.2: The ratio of the higher order Norton surface waves contribution (E_{NW}) to GO component (E_{GO}) of the received field plotted against the sum of R_x height (z_0) and T_x height (z_s). The antennas are located above a half-space dielectric medium (as shown in Fig. 2.1), $\epsilon_{rg} = 4$ and $\sigma = 0.01$ S/m. The Tx antenna in this simulation is horizontally polarized.

2.3 Semi-analytic near-ground propagation model in indoor scenarios

In this Section, an efficient semi-analytic approach to calculate the received electric field in an indoor setting where both the transmitting and receiving antennas are located in close proximity to the ground (less than a wavelength above ground) is presented. It should be noted that, even though the focus here is on near-ground transceiver nodes, the formulation is general and is valid for arbitrary transceiver node heights. We first briefly describe the derivation of the asymptotic computation of the Green's function followed by the description of the approach we pursued to calculate the various components of the received field for a case where the Tx and Rx antennas are located on either side of a single dielectric building wall. The extension of the method to multi-wall scenarios will be discussed in the later part of this section.

The classic problem of calculation of the electric field radiated by an infinitesimal

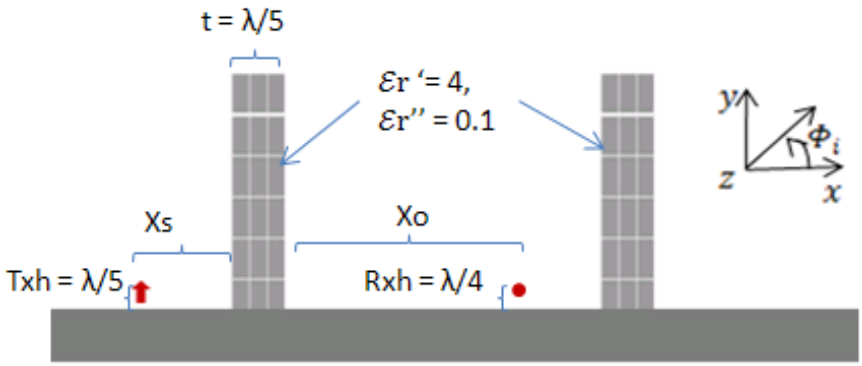

Figure 2.3: A schematic showing the dielectric ground and building walls and a transmitting antenna and observation point

dipole located above a half-space medium has been investigated extensively [29-32]. The available solutions, however, involve the well known Sommerfeld integrals which are of the type given in equation (2.3) and are difficult to evaluate due the presence of poles and oscillatory properties of the integrals. Various exact and asymptotic solutions have been proposed to solve this issue. In [80], a method called the exact image theory is used to derive explicit expressions for fields radiated by dipoles above impedance surfaces. Asymptotic and ray tracing based approaches to efficiently calculate the field radiated by a dipole above a half-space and multi-layer cases have also been proposed [81]-[82].

For transceivers located in indoor scenarios, like the example shown in Fig. 2.3, the total electric field observed at the location of the receiver, can be decomposed into three components as given in the equation below. In the discussion below, the locations (in the rectangular coordinate system) of the Tx and Rx antennas is (x_s, y_s, z_s) and (x_o, y_o, z_o), respectively.

$$E_{total} = E_{direct} + E^{ground}_{scattered} + E^{walls}_{scattered} \tag{2.2}$$

The first component is the field at the location of the receiving antenna if only the Tx and Rx antennas are present in free space. When the ground and the building walls are introduced, the second and third components are created, respectively. The field component scattered by the walls (the third term in equation (2.2)) includes both the reflected (or transmitted) component depending on where the receiver is located and diffracted components from the edges of the walls. Of course, the waves scattered by the ground, walls and other possible obstacles also interact with each other resulting in multiple scattering components. So, the scattered field components are not completely independent. As it was alluded to in the previous section, commonly used indoor field prediction techniques include the field component scattered by the ground by a first order approximation which includes the GO reflected field from the ground and the direct component neglecting the higher order Norton surface waves. Various approaches to calculate Norton surface waves have been described in [83] - [85]. In order to efficiently calculate the field coverage in indoor propagation scenarios, our approach utilizes a fast and accurate computation of dyadic Green's function for a half-space dielectric medium ($\overline{\overline{G}}_{00}$) as derived by Liao et al [83].

The derivation of this solution begins with the two-fold integral form of the dyadic Green's function which does not have a closed form solution [86]. After applying a change of variable, for the setup shown in Fig. 2.1, the scattered field from the ground at the location of the receiver (for $z_s > z_o$) can be written in terms of k_ρ (the component of the wave vector in the $\vec{\rho}$ direction in cylindrical coordinate system) and Bessel functions as given in (2.3) which involves the well-known Sommerfeld integral.

$$E_{ij}^{scattered} = \frac{-\omega\mu_o I_o l_i}{8\pi}\int_0^\infty f_{ij}(k_\rho)e^{ik_{oz}(z_o+z_s)}d_{k_\rho}, \tag{2.3}$$

In the above equation, the function f_{ij} is expressed in terms of k_ρ and Bessel functions. The indices i and j are the polarizations of the Tx and Rx antennas, respectively. $I_o\vec{I} = I_o(l_x\vec{x} + l_y\vec{x} + l_z\vec{z})$, ω and μ_o are the current moment vector, the angular frequency and free space permeability, respectively. Also, the following equation relates k_ρ and k_{oz} to the wave vector.

$$k_o^2 = k_\rho^2 + k_{oz}^2 \tag{2.4}$$

After applying yet another change of variable in (2.3) for k_ρ ($k_\rho = k_o \sin\omega$), we use Hankel's functions to extend the limits of integration (from $-\infty$ to $+\infty$). The asymptotic forms of Hankel's functions for large arguments are then applied. Finally, the method of saddle point integration is used to get the saddle point contribution up to second order (E_{sp}) by using

$$E_{ij}^{sp} = \frac{-k_o^3\eta_o I_o l_i}{8\pi}e^{ik_o\rho}[\frac{f_{ij}(w_s)}{ik_o\rho} + \frac{\frac{f_{ij}''(w_s)}{2} + \frac{f_{ij}(w_s)}{8}}{(ik_o\rho)^2}], \tag{2.5}$$

where, w_s,η_o and k_o are the saddle point, the free space impedance and the wave number, respectively. As validated in the original work, it turns out that this contribution, when added to the direct signal, results in an accurate approximation of the received field in the presence of the ground. The first term in equation (2.5) is

the Fresnel reflection contribution while the second term is known as Norton surface waves and become dominant when the transceiver height is small in terms of wavelength. The saddle point ($w = w_s$) is calculated using the following relations. Analytic expressions for f_{ij} are included in Appendix A. R is the distance between the transmitter and receiver antennas.

$$\sin(w_s) = \frac{\rho}{R} \tag{2.6}$$

$$\cos(w_s) = \frac{z_o + z_s}{R} \tag{2.7}$$

$$R^2 = \rho^2 + (z_o - z_s)^2 \tag{2.8}$$

To get the total field components that make up the dyadic Green's function ($\overline{\overline{G}}_{00}$), the direct signal components have to be added to the scattered components discussed above. Finally, the dyadic Green's function can be written as given below.

$$\overline{\overline{G}}_{00} = \frac{1}{jk\eta_o} \begin{bmatrix} E_{xx} & E_{yx} & E_{zx} \\ E_{xy} & E_{yy} & E_{zy} \\ E_{xz} & E_{yz} & E_{zz} \end{bmatrix} \tag{2.9}$$

It should be noted that even if the derivation is for the case where the receiver is above the source ($z_s > z_o$), the Green's function for the other case ($z_s < z_o$) can

be found by applying the principle of reciprocity which is mathematically equivalent to performing the complex transpose of the expression given in equation (2.9). This Green's fucntion is used throughout the rest of the derivations. By making use of $\overline{\overline{G}}_{00}$ when calculating the wave radiated by the transmitting antenna, the background propagation medium is changed from free space to a half-space dielectric. This step enables us to include the first two components of the total field given in (2.2).

2.4 Calculating scattering from indoor obstacles

In this subsection, a way to efficiently calculate the field component scattered by indoor obstacles such as building walls,ceilings and furniture (which is the third term in (2.2)) will be developed. The approach we pursued to calculate this component is by making use of physical optics approximation and volume equivalence principle in conjunction with the Green's function that was discussed. Let's first consider the problem geometry shown in Fig. 2.3 with a single dielectric building wall disregarding for now the second wall and any additional scatterers and discuss a way of calculating the scattered field by this wall. It should be noted that the field scattered by the building wall is computed in the presence of the ground. The extension of the method to a multi-wall or more realistic indoor propagation scenarios will follow.

Volumetric polarization currents which will be used to replace the various dielectric scatterers are determined by the incident field from the transmitting antenna, boundary conditions on the wall surface and dielectric properties of the building wall. The effective dielectric properties of typical building walls such as brick or cinderblock can be measured or calculated based on available dielectric mixing models [87]- [88]. Once the geometry and dielectric properties of the building walls are

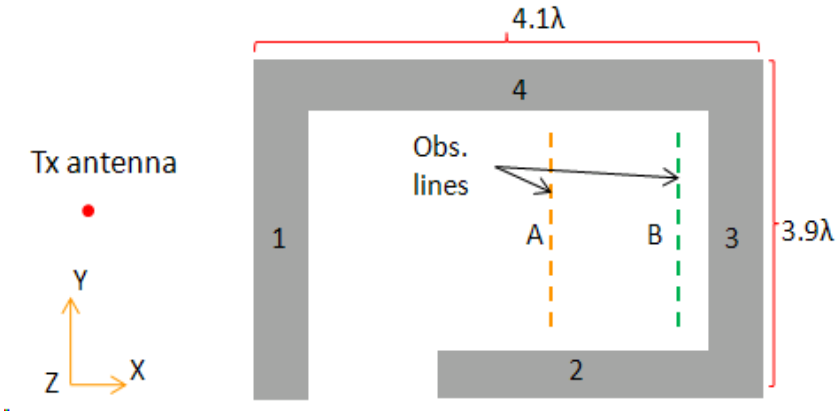

Figure 2.4: A schematic (top view) of multi-wall indoor propagation scenario showing the Tx antenna and the observation point (ground not shown)

known, the first step is to calculate the incident electric field on the surface of the wall that is in the direct view of the transmitter. For a given antenna with known current distribution $\vec{J}$, the incident field on the wall surface can be calculated using:

$$\vec{E}_{inc} = jk\eta_o \iiint \vec{J}(r')\overline{\overline{G}}_{00}(r, r')d_{r'}. \tag{2.10}$$

The incident field will then be decomposed into TE and TM components by using the following procedure:

$$\vec{E}_{inc}^{TM} = \vec{E}_{inc}.(\frac{\vec{ki} \times \vec{n_w}}{|\vec{ki} \times \vec{n_w}|} \times \vec{ki}), \tag{2.11}$$

$$\vec{E}_{inc}^{TE} = \vec{E}_{inc}.\frac{\vec{ki} \times \vec{n_w}}{|\vec{ki} \times \vec{n_w}|}. \tag{2.12}$$

Here, $\vec{ki}$ is the unit vector in the direction of the incident field and $\vec{n_w}$ is the unit vector in the direction of the source and normal to the wall directly illuminated by

the antenna. Once we have the TE and TM components of the incident field on the wall surface, we will then use them to approximate the fields inside the dielectric wall using physical optics approximation. The total field inside the wall is calculated locally assuming the wall is infinite and illuminated by a plane wave. It should be noted that this assumption will require that the Tx antenna be in the far-field region relative to the point in question inside the wall. The expressions for the total field inside the wall surface for the TE_z case are given in (2.13) and (2.14) below. Similar expressions can be found for the TM_z case by applying the principle of Duality.

$$E_x = \frac{-k_y}{\omega \epsilon_w}(A_w e^{ik_{wx}x} + B_w e^{-ik_{wx}x})e^{ik_y y}, \tag{2.13}$$

$$E_y = \frac{-k_{wx}}{\omega \epsilon_w}(A_w e^{ik_{wx}x} - B_w e^{-ik_{wx}x})e^{ik_y y}, \tag{2.14}$$

where, k_{wi} (i =x,y or z) are the components of the propagation constant in the wall (k_w). A_w and B_w are given by

$$B_w = \frac{T_{TE} E_{inc}^{TE}}{1 - R_{TE}^2 e^{i2k_{wx}d}}, \tag{2.15}$$

$$A_w = B_w R_{TE} e^{i2k_{wx}d}, \tag{2.16}$$

$$T_{TE} = \frac{2k_{ox}}{k_{wx} + k_{ox}}, \tag{2.17}$$

$$R_{TE} = \frac{k_{wx} - k_{ox}}{k_{wx} + k_{ox}}, \tag{2.18}$$

$$k_w^2 = k_{wx}^2 + k_{wy}^2 + k_{wz}^2 \;\; \& \;\; k_w = w\sqrt{\mu\epsilon_w}. \tag{2.19}$$

In the above equations, d is the thickness of the wall. Having calculated the total fields inside the wall, we can obtain volumetric polarization currents based on the dielectric properties of the wall. The equation relating the total electric field inside the wall and the polarization current is given below.

$$\vec{J}_{ep} = -iw\epsilon_o(\epsilon_{rw} - 1)\vec{E} \tag{2.20}$$

The final step in calculating the scattered field by the building wall is to propagate the fields from the polarization currents using (2.10). Both the propagation from the source to the wall surface and the forward propagation of the field of the polarization currents to the observation point are calculated by taking the near-ground propagation effects into account. This method takes into account the Norton surface waves which affect the volumetric polarization currents of the wall and hence the scattered field by the building wall.

For an indoor propagation scenario such as the setup shown in Fig. 2.4, the way the scattered field from each wall is calculated in the semi-analytic model is as follows: First the volumetric polarization currents for the walls in the direct view of

the transmitter are computed by following the procedures outlined above. Then, the field from these currents and the current on the transmitting antenna are computed using $\overline{\overline{G}}_{00}$ for any observation point within or outside the building. Finally, geometric optics is used to account for the shadowed walls. Basically near-ground fields from the source and the lit wall/s are reflected/transmitted at the specular points on the shadowed walls according to the Fresnel law of reflection and transmission to account for walls that are not in the direct view of the transmitter. This process can be followed multiple times to capture all multipath among the building walls. Since Norton waves decay very fast with propagation distance, one simplifying feature of near-ground propagation is that the convergence in field calculation is reached much faster than ordinary ray tracing. Simulations show that one or two iterations are sufficient to reach convergence. This approximation appears to be more accurate away from the edges of the walls and corners, as the near-field edge effects are not properly accounted for in our model.

2.5 Numerical Validation and analysis

To validate the proposed hybrid model, a full-wave simulation is first used for the 2D wall-ground case. Numerical validation for a more complex indoor scenario in the 3D case is also presented. Time-domain analysis of the received field is performed in order to understand the various propagation mechanisms. Comparison of the scattered field component by a furniture against the contribution of Norton waves to the total electric field is presented. To assess the accuracy of the proposed technique as compared to ray tracing, error comparison against a ray tracing routine is discussed. Simulation results using a commercial FDTD solver is used as a reference in the error

analysis. Also, the errors in the comparisons of the simulation results are explained by pointing out the various assumptions and approximations.

2.5.1 Validation of the 2D single wall-ground scenario

First, a single wall building geometry as shown in Fig. 2.3 (with one wall) in 2D where the length of the wall (along z direction) was assumed to have an infinite extent. As it is a 2D case, a line source of constant current with vertical polarization (y-directed) is used as a source which is placed 40λ away from the first wall. The observation point is varied on the other side of the wall along the X axis while keeping the height of the receiver the same. This scenario is simulated using both the semi-analytic technique and a 2D numerical solver based on the Nystrom method [89].

The electric field calculated based on the two methods is plotted against the distances of the observation points from the first wall (denoted by Xo in Fig. 2.3. Two cases are considered where different heights of the transceivers is used. In the first case (shown in Fig. 2.5 and Fig. 2.6), the heights of the transmitter and receiver are $z_s = 0.2\lambda$ and $z_o = 0.25\lambda$, respectively. In this case, the Tx and Rx heights are well within the height limits where the Norton waves become dominant. In the second case (Fig. 2.7), the Tx and Rx heights were increased to $z_s = 0.53\lambda$ and $z_o = 0.47\lambda$ in which case the Norton waves are still significant but not as dominant as the first case. In both cases, the dielectric constant for the wall and the ground is chosen to be 4 + 0.1j and the frequency is 200MHz. The dielectric constants used for the wall and the ground are the same because of the limitations imposed by the numerical code we used for validation which was originally developed for simulation

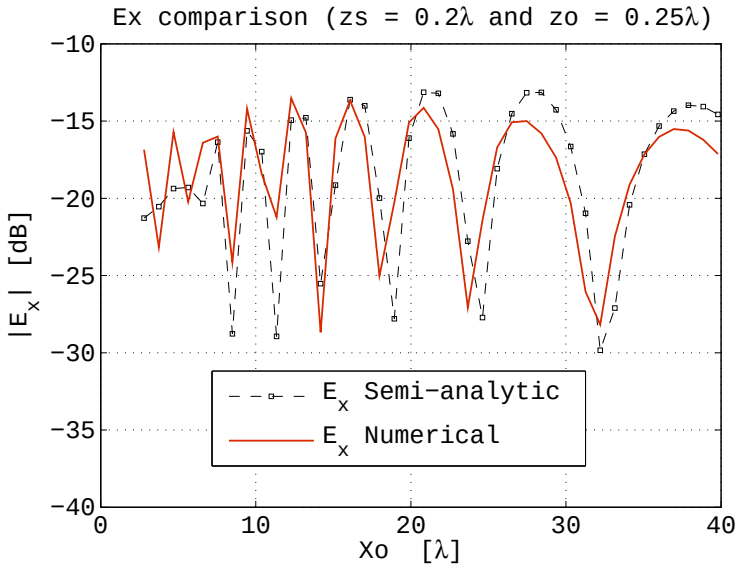

Figure 2.5: Comparison of received electric for the single wall ground geometry (2D case) between the proposed technique and a numerical solution.

of propagation above rough surfaces [89].

For both scenarios, the components of the electric field computed using the proposed method show good agreements with that of the full-wave solution. However, there is about a maximum of 2dB error and a slight shift in the maxima and minima where the errors are also higher. The discrepancies occur because of the approximations used both in the proposed semi-analytic technique and the full-wave solution. First, in the semi-analytic technique, the calculation of the polarization currents for the dielectric wall is not exact. This is because when the total field inside the wall is computed, the wall is treated as an infinite dielectric slab which introduces an error in the total electric field inside the wall since the contributions to the field by any reflections from the wall edges are not accounted for. The second reason has to do with the accuracy of the full-wave model. To create the vertical wall structure, we are using a very large slope in the Nystrom model for dielectric surfaces. This creates inaccuracy in the calculated surface currents near the edges and corners. It should

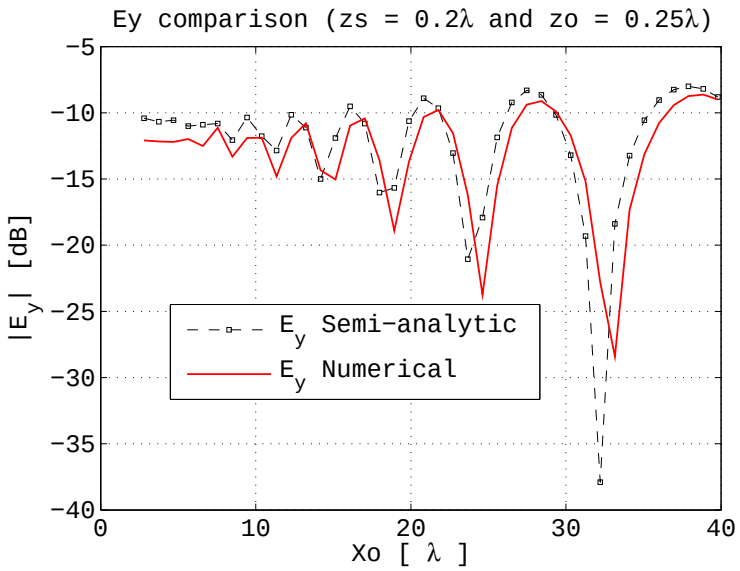

Figure 2.6: Comparison of received electric for the single wall ground geometry (2D case) between the proposed technique and a numerical solution.

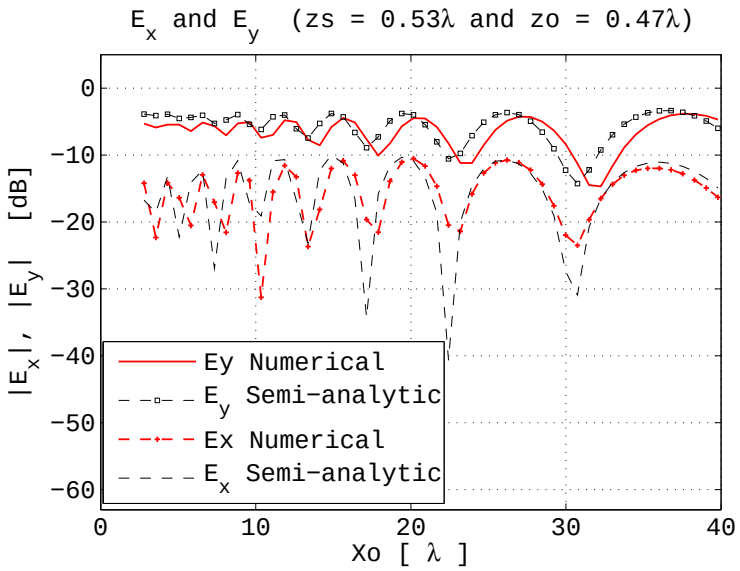

Figure 2.7: Comparison of received electric for the single wall ground geometry (2D case) between the proposed technique and a numerical solution.

be noted that the error in the Nystrom approach is very small and this solution is discussed extensively and validated in the original work [38]. So, it makes sense to use it to validate our proposed approach. As can be seen in Fig. 2.5, 2.6 and 2.7 the two independent methods are in good agreement.

2.5.2 How do Norton waves and scattering from furniture compare?

Having validated our proposed model for a single wall-ground geometry, we will proceed to show the significance of the Norton waves specifically for near-ground sensors in indoor scenarios. The careful reader might wonder how important taking the Norton waves into account is, specifically for indoor propagation environments. Here we will show that the Norton waves are actually more vital for accurate prediction of the electric field received by near-ground sensors than the inclusion of indoor obstacles such as furniture. To demonstrate this we carried out simulations to compare the Norton component to scattering from a wooden table. The setup of the simulation is given below.

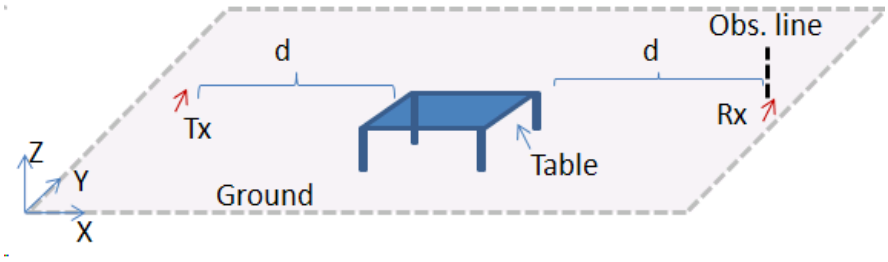

Figure 2.8: Geometry used for the simulation for analysis of scattering from a wooden table. The dimensions of the table top is (2m by 2m by 0.1m and each table leg is 1m long having a diameter of 0.1m. The frequency of simulation is 300 MHz.

In the first simulation, a horizontally polarized Tx antenna is positioned just above a half-space dielectric (as shown in Fig. 2.8) and the electric field at the location of the receiver is calculated for various points along the Z-axis. In the second

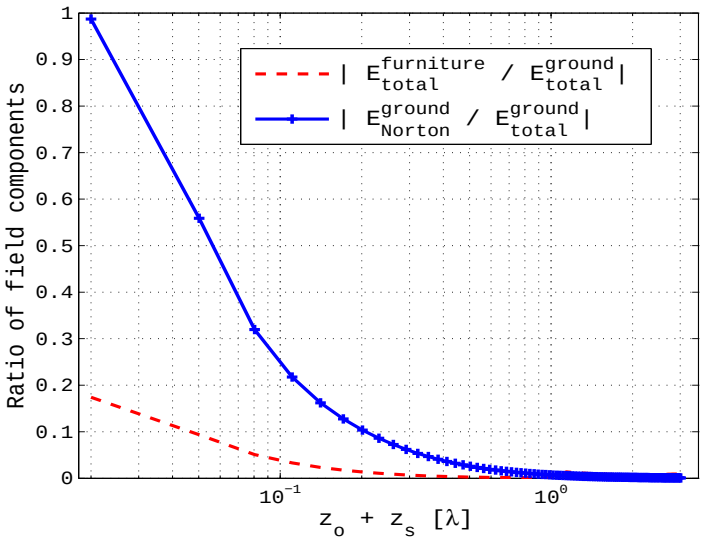

Figure 2.9: Comparison of the effect of Norton waves and scattering from a furniture (a table). The dielectric constant of the ground was assumed to be $\epsilon_{rg} = 4 + j0.5995$ and that of the wooden furniture is $\epsilon_{rg} = 1.4 + j0.0728$. The simulation frequency is 300 MHz.

simulation, we introduced a wooden table which we modeled by a thin homogeneous dielectric box and four cylindrically-shaped dielectrics for the top part and the four legs, respectively. The dielectric constant of the table is assumed to be $\epsilon_{rg} = 1.4 + 0.0728j$. The dimensions of the table top is (2λ by 2λ by 0.1λ) and the each table leg is 1λ long having a diameter of 0.1λ. For this simulation d is chosen to be 25λ (Fig. 2.8). The table is positioned in the path of the direct signal from the Tx antenna to the Rx antenna so that the maximum effect of the table is included.

The scattered field from the table is calculated by using the Born approximation where the total field inside the dielectric (table) is assumed to be the same as the total field in the absence of the table. The total field inside the wooden table is then used to calculate the volumetric polarization currents which are then used to predict the field component that is scattered by the table. This approximation is justified because the dielectric constant of the wooden table is relatively small. In addition, this approximation overestimates the exact total field inside the wooden table. Therefore,

the scattered field calculated using this method will be an overestimation of the exact scattered electric field. If this estimate is much less than the Norton component, then we can confidently say that the exact field scattered by the table would also be much less than the Norton contribution. The ratio of the Norton component to the total received field is shown in Fig. 2.9 (solid curve). The dashed curve in Fig. 2.9 shows the ratio of the field scattered by the furniture to the total field received in the presence of the ground (without the furniture). The main point of this analysis is to show that, for near-ground transceivers, taking into account the Norton waves is much more important than the inclusion of scattering from furniture. So, by adding the Norton waves and utilizing physical and geometrical optics type approaches to take into account scattered field from relatively large indoor scatterers (building walls), we can significantly improve the accuracy of the predicted electric field compared to what the usual ray tracing approach provides. This comparison will be discussed in more detail later in this section.

2.5.3 Time-domain analysis of the received field

Analyzing the time domain characteristics of the technique is vital because it provides insight into the various scattering mechanisms. This knowledge can be applied to further refine the field prediction technique by focusing on the dominant contributions. In this analysis, the electric field for fixed source and observation points is computed in time-domain for a single wall-ground scenario like the one shown in Fig. 2.3 (with one wall). For this simulation, a vertical dipole positioned $10m$ away from the first wall is used as a Tx antenna and the observation point is $9.7m$ away from the other side of the wall. The heights of the Tx and Rx antennas are

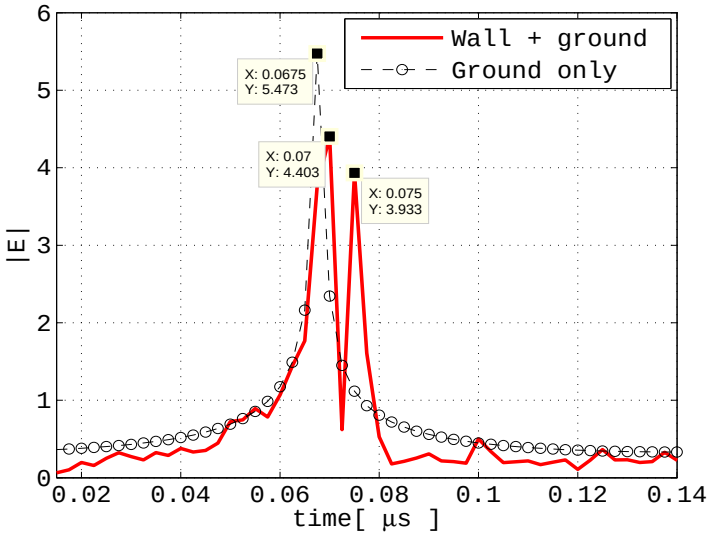

Figure 2.10: Magnitude of the total electric field in time domain for a single wall-ground geometry as compared to the case where only the ground is considered.

$0.11m$ and $0.1m$, respectively. The wall extends from $x_w = 10m$ to $x_w = 10.5m$ and its height is $3m$. The dielectric constants of both the wall and the ground are chosen to be $\epsilon_r = 4.5 + 1.189j$. To calculate the time domain signal accurately, first the field at the observation point is computed as a function of frequency (at several frequency points). Then, the Inverse Fourier Transform is applied to the frequency domain field data. It should be noted that sufficient bandwidth and number of frequency points are needed to recover the time-domain signal accurately. The bandwidth dictates the spatial resolution in time-domain and the frequency step determines the time extent of the resulting time-domain signal. This means that if the bandwidth is too small, it won't be possible to differentiate the direct and diffracted components. Therefore, large bandwidth and very fine frequency step are needed. The frequency range used for this simulation is 5MHz - 405MHz with 60 frequency points.

Table 2.1: Comparison of the peak delays.

	$d_{act}[m]$	$d_{est}[m]$	Physical mechanism
Peak 1	20.20	20.25	Direct signal with ground and wall
Peak 2	22.33	22.50	Diffracted by the top edge of the wall

As shown in Fig. 2.10, two major peaks are found in the time domain plot of the received field. First, the actual distances (d_{act}) for both the direct and diffracted paths are calculated from the geometry used in the simulation and the estimated distances (d_{est}) for both paths are also calculated from the the time delays of the peaks. Table 2.1 summarizes distances from the source to the receiver calculated based on the geometry and peak delays from the simulation for both the direct and diffracted signal paths. The first peak corresponds to the signal that is directly coupled between the transmitter and receiver through the wall in the presence of the ground. The second peak corresponds to the field diffracted by the top edge of the building wall. In both cases, there is a small error between the estimated and the actual distances (0.25% for the direct and 0.74% for the diffracted signals). This error is caused by the approximate calculation of the distances for both paths. This analysis is useful for applications where we want to separate the constituent components. For example, it becomes very useful when laboratory measurements are used for validation of the proposed technique to separate the multipath from the desired signal.

2.5.4 Semi-analytic vs. Full-wave vs. Ray tracing

A multi-wall scenario where an infinitesimal dipole located just above the ground and is radiating outside a room consisting of four walls is simulated based on the proposed semi-analytic technique. The same propagation scenario is also simulated using a commercial full-wave solver (FDTD based solver named Semcad X) and a ray tracing routine. This comparison serves two purposes. The Semcad X results validate the proposed technique while comparison with ray tracing shows the im-

provements that the new technique offers especially for near-ground propagation in indoor scenarios.

For this particular simulation, as can be seen in Fig. 2.4, the setup is as follows. The room is 3.9λ by 4.1λ and all four walls have heights of 2.56λ and thickness 0.2λ. The Tx antenna is located 15λ away from the first wall and its height is 0.25λ. The electromagnetic properties used in this simulation for all the walls and the ground are $\epsilon_r = 4.5$ and $\sigma = 0.02$. The frequency used for this simulation is 300MHz. It should be noted that the effects of doors, windows and other indoor obstacles are not included in this implementation, but these changes can be integrated in our model. The errors for both the semi-analytic (SA) and ray tracing (RT) techniques are calculated based on the following equation. E_{FW} represents the electric field computed based on the full-wave solver.

$$error_{RT,SA} = \frac{|E_{RT,SA} - E_{FW}|}{|E_{FW}|} \tag{2.21}$$

The errors in the predicted electric field from the two methods are computed and plotted against position for the observation lines shown in Fig. 2.4 (Traces A and B). As can be seen in Fig. 2.11, the proposed approach has errors that are much lower than that of ray tracing. Of course, as the transceiver heights increase, the errors in the predicted electric fields by the two methods will be similar because the Norton waves become less significant at higher heights.

In addition, simulations showed that the proposed semi-analytic technique is more than 5 times faster than the full-wave solver. Similar to the 2D single wall case dis-

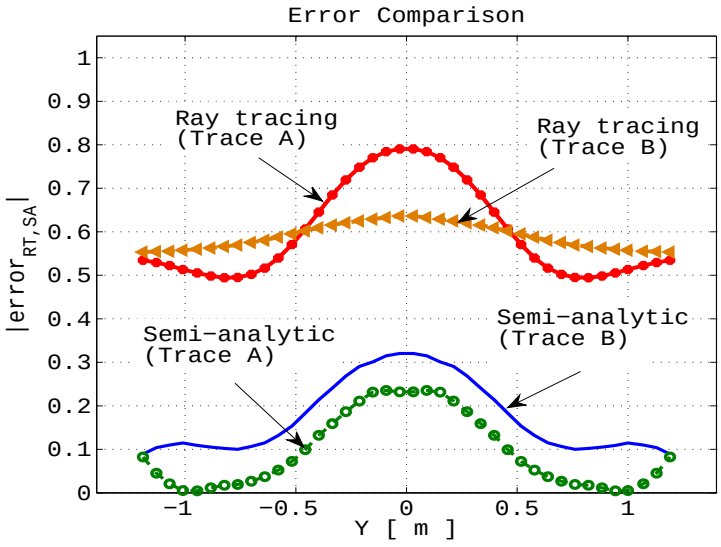

Figure 2.11: The error introduced by using the semi-analytic method and ray tracing. For this simulation, a full-wave FDTD solver is used as a reference. The observation lines (Traces A and B) are shown in Fig. 2.4.

cussed, the discrepancies between the full-wave solution and that of the new technique is due to the various approximations made which are discussed in Section 2.5.1. In addition, the approach used to include scattering from walls that are not in the line of sight of the Tx antenna (walls 2,3 and 4 in Fig. 2.4) is essentially geometrical optics with the exception that the Norton waves are taken into account. This approximation also contributes to the discrepancies between the proposed method and the numerical result.

2.6 Measurement Results

To further examine the validity of the proposed approach comparison against measurements under laboratory controlled environment is carried out. Controlled experiments under laboratory conditions are preferred over realistic settings as all the experimental parameters are well-characterized and features that can lead to

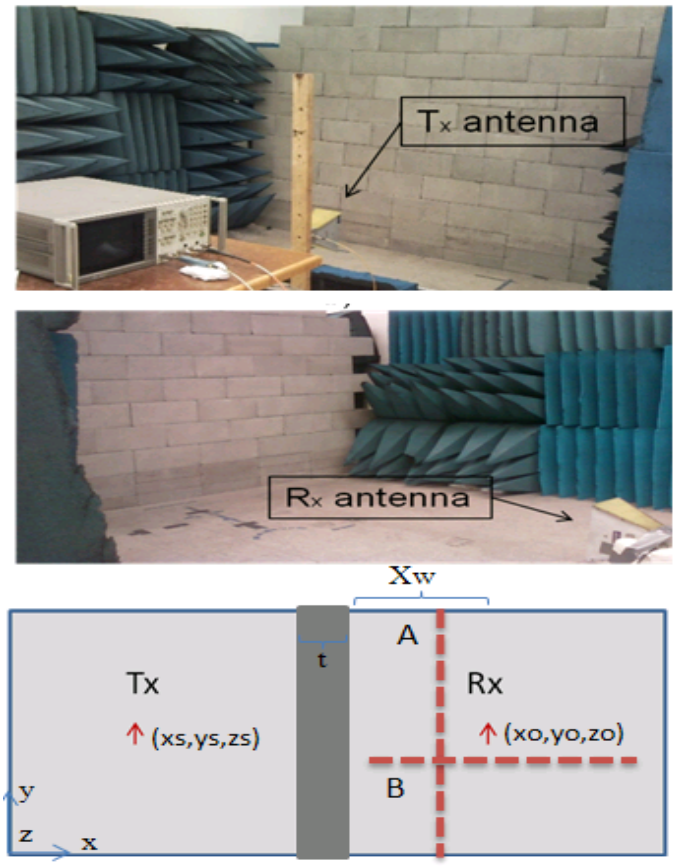

Figure 2.12: Measurement setup consisting of concrete wall, network analyzer, Tx antenna (on one side of the wall) and Rx antenna (the other side of the wall). The dimensions of the wall are: $h = 1.56m$, $L = 2.56m$ and $t = 0.09m$.

uncertainty in the measurements can be suppressed or removed. As shown in Fig. 2.12, the experimental setup consists of a single wall build out of concrete blocks and two horn antennas used as Tx and Rx antennas positioned on either side of the wall. The length, height and thickness of the wall are 2.56m,1.56m and 0.09m, respectively. The antennas are connected to the two channels of a network analyzer via long cables. The real part of the dielectric constant and the conductivity of concrete are assumed to be 4.5 and 0.02S/m, respectively. The Tx antenna is positioned 1.74m away from the wall. The received electric fields are recorded for various points by moving the receiver along traces A and B shown in Fig. 2.12. In the first case (a), the path is along the x-axis where $y_s = 1.37m$, $y_o = 1.37m$, $z_s = 0.24m$ and $z_o = 0.20m$. In

the second case (b), the trace is along the y-axis for which $z_s = 0.24m$, $x_w = 0.91m$ and $z_o = 0.20m$. The final case (c) is the same as (b) but with different transceiver heights ($z_s = 0.87m$ and $z_o = 0.79m$). Both the Tx and Rx antennas are oriented to provide vertical polarizations. The whole setup is surrounded by absorbers to minimize unwanted scattering from other objects in the laboratory.

For the setup described above, the ratio of the signal at the receiving channel of the network analyzer to the signal at the transmitting channel (S21) is measured from 1GHz to 5GHz with 20MHz frequency step. It should be noted that due to limitations imposed by the size of low frequency wideband antennas and the large size of the overall measurement setup (for low frequency measurements), we resorted to performing a scaled measurement at higher frequencies. The downside to using this method is that at these frequencies, the lowest antenna height (measured from the phase center) is limited by the size of the ultra-wideband double-ridge horn antennas we used which are higher than the Tx and Rx antenna height values at which the Norton waves are dominant. However, since our method is still valid for any transceiver height, the scaled measurements can be used to demonstrate the accuracy of the proposed field prediction model compared to actual measurements. All measurements are performed first in the presence of the concrete wall. Then, a second set of measurements are performed without the wall to establish a reference for calibration.

The acquired field data needs to be calibrated before comparing it with results from the semi-analytic technique. As it was alluded to in Section 3, the results from the time-domain analysis become helpful for calibration of the measured results. The goal is to remove unwanted multiple reflections from other scatterers in the labora-

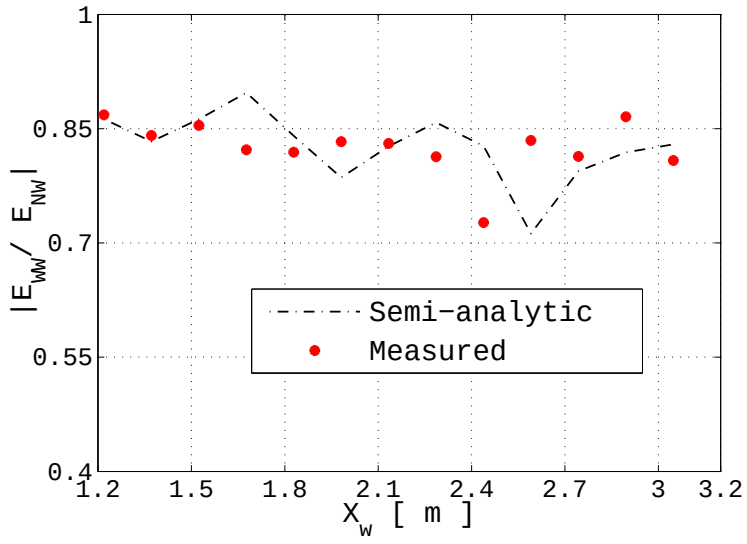

Figure 2.13: Field magnitude comparison between the the proposed semi-analytic method and measured values when Tx is moved along path B ($ys = 1.37m$, $yo = 1.37m$ and $zs = 0.24m$) as shown in Fig. 2.10

tory since isolating the effect of the wall on the received field is what we want to achieve. Based on the conclusions drawn from the analysis in Section 2.5.3, the dominant components for a single wall-ground set up are isolated in the measurement results. First the frequency domain data is converted to time domain by taking its Inverse Fourier Transform. Then, time-domain gating is performed by which components of the signal that are from unwanted scatterers are removed and the Fourier Transform is applied to the gated signal to obtain the frequency domain response of the transmission through the wall (E_{ww}). The same procedure is applied to the signal measured without the wall (E_{nw}). Finally, the resulting data is calibrated by dividing the transmission measurement obtained with the wall by that obtained without the wall.

The comparisons between the proposed approach and the measurements are shown in Fig. 2.13, 2.14 and 2.15 where good agreements are demonstrated with about 10% error in all three cases. The cause of the discrepancies include the following: 1) the

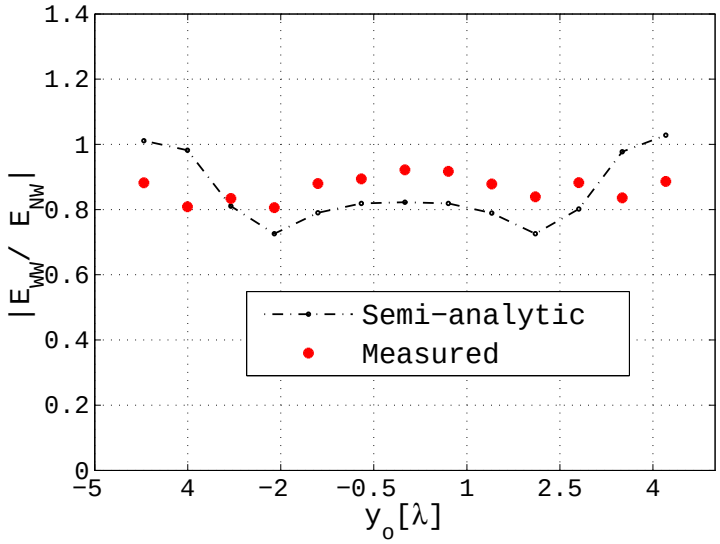

Figure 2.14: Field magnitude comparison between the the proposed semi-analytic method and measured values when Tx is moved along path A ($zs = 0.24m$, $xs = 0.91m$ and $zo = 0.20m$) as shown in Fig. 2.10

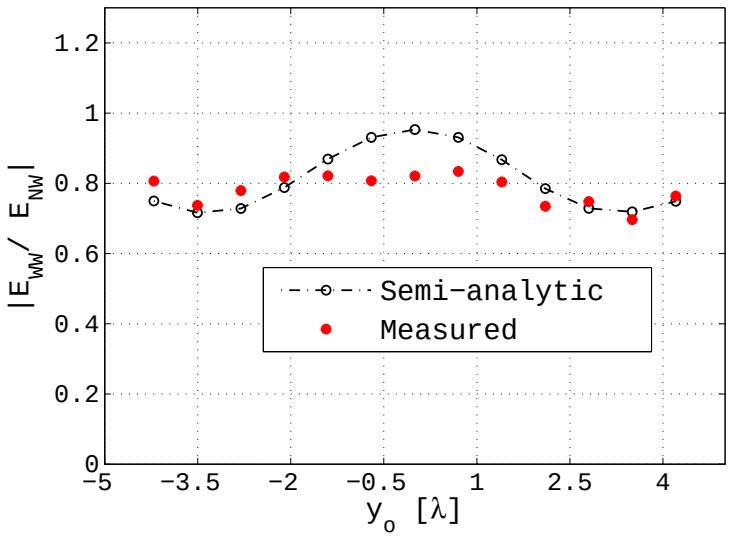

Figure 2.15: Field magnitude comparison between the the proposed semi-analytic method and measured values when Tx is moved along path A ($zs = 0.87m$, $xs = 0.91m$ and $zo = 0.79m$) as shown in Fig. 2.10

dielectric constants used in the simulation for the ground and the wall are only approximate values, 2) both the ground and the concrete wall have inhomogeneities and hence the effective dielectric properties already include errors, and 3) errors in the actual vs measured positions of the Tx and Rx antennas all contribute to the overall discrepancies.

CHAPTER III

Sub-wavelength Source Tracking in GPS-challenged Environments

3.1 Introduction

In this chapter a source tracking approach in the HF range that combines interferometry based direction finding and triangulation based on measurements from at least two points is proposed. The advantage of choosing the operating frequency in the HF range is two-fold. First, scattering from walls ceiling and furniture will be small compared to the direct path making direction finding with good resolution possible. Said another way, the multipath level becomes very small compared to higher frequencies. The second advantage of using HF is that wave propagation for near-ground antennas ($h < \lambda$) is supported by Norton surface waves which are confined on or near the ground and hence illuminate only the lower part of scatterers such as walls, furniture and ceiling. This in turn makes the scattered components from these indoor scatterers smaller compared to the case where the antennas are well removed from the ground ($h > \lambda$). It should be noted that the significance of the surface waves increases as the distance between Tx and Rx antennas increases. Numerical models are used to investigate wave propagation and scattering in complex indoor scenarios at these frequencies. Of course, there is a tradeoff between the

size of the antenna and the level of multipath. As the frequency is lowered the size of the antenna becomes prohibitively large for many applications (as an example, the length of a half-wave dipole in the HF range is several meters). So, one challenge is to design a compact antenna to be used both for the Tx and Rx antennas. For our system prototype, we designed a miniaturized antenna having vertical polarization and an omnidirectional radiation pattern. In the presence of the ground only, the received signal is maximized when both the Tx and Rx antennas have vertical polarization. Another challenge that is addressed in this chapter has to do with the small antenna spacing of the receive array. At low frequencies such as the HF range, the phase difference between the received signals, which is an important quantity of interest, becomes too small to be measured. To tackle this issue, a phase difference amplification scheme that mimics the hearing mechanism of a fly (Ormia Ochracea) is designed and fabricated. The system validation and resolution analysis based on numerical and measurement results is discussed.

In the rest of the chapter, we first describe the proposed source tracking technique. Then wave propagation models for realistic indoor scenarios are utilized to investigate the proposed technique. The system prototype along with the design and test results of various components including the phase difference amplification circuit are also discussed. Also in this section, a description of a low profile highly miniaturized antenna used in the system prototype is included. The approach utilized to achieve high radiation efficiency and omnidirectional radiation pattern is described. We conclude this chapter with discussion of the source tracking system test results for various multipath environments.

3.2 Proposed Source Tracking Approach

The technique we are proposing for direction finding utilizes the received signals on an array of antennas closely positioned ($\lambda/15$ spacing) on a rotating platform. A schematic showing the proposed technique is given in Fig. 3.1. The magnitude and phase differences between the received fields on the elements of the array provide information about the direction of the source. The direction of arrival (DOA) is determined using the phase and magnitude of the received signals based on

$$DOA = \underset{\theta_i}{\text{Min}} \left[\, |\Phi(E_1^r(\theta_i)) - \Phi(E_2^r(\theta_i))| \, \right], \tag{3.1}$$

$$DOA = \underset{\theta_i}{\text{Min}} \left[\, \frac{|E_1^r(\theta_i) - E_2^r(\theta_i)|}{|E_1^r(\theta_i) + E_2^r(\theta_i)|} \, \right], \tag{3.2}$$

where $E_1^r(\theta_i)$ and $E_2^r(\theta_i)$ are the complex received fields at each element of the receive array as a function of the incidence angle θ_i (the angle between the bisect of the Rx array and the incident wave) and Φ which is the phase of the received field. The DOA of a given source needs to be correctly retrieved from at least two locations separated by a known baseline outside the building. By using the coordinates of the receiver arrays and the retrieved angles (β_1 and β_2), the location of the source is calculated by triangulation. The vector baseline $\vec{B}$ can be characterized very accurately, for example, using a differential GPS unit mounted on the two platforms. As it was alluded to in the previous Section, to minimize the effect of multipath as much as possible, the use of the lower band of the electromagnetic spectrum (HF-band) is proposed. When the level of multipath increases (i.e. when the frequency of

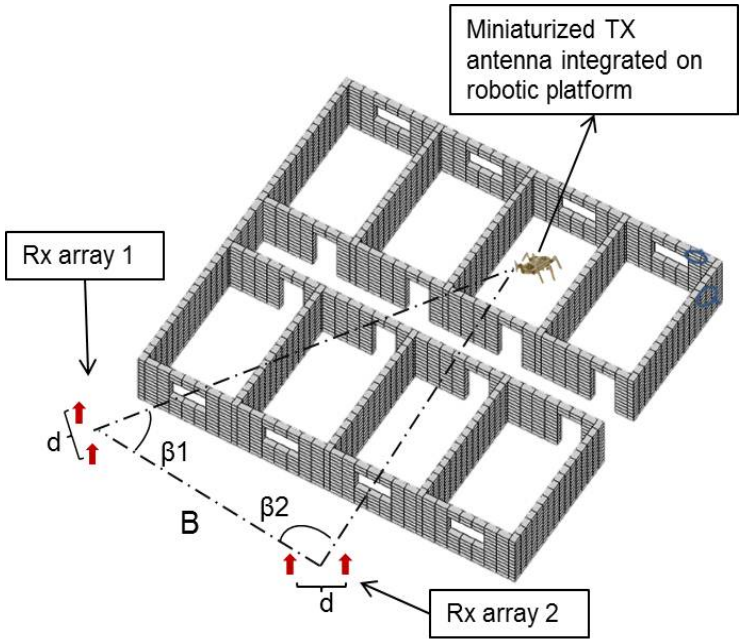

Figure 3.1: A schematic illustrating the proposed approach. It consists of a complex building scenario, receiver arrays and the Tx antenna (building picture is borrowed from [23]).

operation for a given geometry of propagation scenario is increased), the resolution of the retrieved DOA will degrade. It is shown that based on full-wave simulations in the presence of mostly dielectric scatterers, the direction finder works with good resolution in the HF range. Another advantage of using HF has to do with near-ground propagation effects which is unique to antennas that are very close to the ground in terms of wavelength. The Tx and Rx antenna heights for many of the applications of interest is only a small fraction of the wavelength. For example, at 20MHz, 1m antenna height is only $\lambda/15$. Wave propagation at such low antenna heights is dominated by Norton surface waves [83],[90]. For near-ground antennas, unlike in the case of antennas that are well removed from the ground (having heights greater than a wavelength), the received electric field which is dominated by Norton surface waves decay as $\frac{1}{R^2}$ [83]. For this reason, in the presence additional scatterers, multipath effects also decay fast for near-ground antennas.

In order to achieve a high resolution source tracking system, there are three things that need to be considered. First, the Signal-to-noise ratio (SNR) should be maximized because it is the main limiting factor determining the smallest phase difference that can be accurately measured which in turn determines the maximum tracking resolution. Secondly, the orientations for each antenna should be selected so that the received signal is maximized while the multipath effects are further minimized. In the proposed system vertically polarized transmit and receive antenna arrays are chosen to maximize the received signal. The third important variable is the spacing between the antenna elements in two Rx antenna array sets as it has to be large enough so that the phase difference due to path length differences is not too small.

3.3 Propagation Modeling and Analysis

For Tx and Rx antennas located in a complex propagation environment, the received signal includes the direct, reflected, diffracted and multiply scattered components from the scatterers in the environment. The major scatterers in indoor environments are walls, big furniture, ceilings and the ground. In order to quantify the effect of multipath on the DOA retrieval technique, an accurate and efficient propagation model that takes into account scattering from the major indoor scatterers is required. Once we have a propagation model, we can then quantify the effects of indoor scatterers as a function of frequency, geometry of the problem, and electromagnetic properties of the various scatterers. As a first order analysis to investigate the effects of walls and similar scatterers, we will first calculate the reflection coefficient from a single dielectric wall for different values of wall thicknesses, incidence angles and frequencies. Here, the wall is essentially modeled as a dielectric

slab having an effective complex dielectric constant. The real (ϵ_r') and imaginary part (ϵ_r'') of the dielectric constant of the wall used for this calculation are 4 and 0.9 at 20MHz, respectively. At 100MHz, ϵ_r' is 4 and ϵ_r'' is 0.2. The use of a constant effective dielectric constant for the walls is a good approximation for realistic walls made out of bricks or cinderblocks at the frequency of interest (HF band).

Table 3.1: Wall Reflectivity (Tw is thickness of the wall,$\epsilon_r' = 4$ and $\epsilon_r'' = 3.6$ @ 5MHz), ϕ_i is the incident angle measured from the normal to the interface.

f [MHz]	Tw [cm]	$\lvert\Gamma_{TE}\rvert$ $\phi_i = 30°$	$\lvert\Gamma_{TM}\rvert$ $\phi_i = 30°$	$\lvert\Gamma_{TE}\rvert$ $\phi_i = 60°$	$\lvert\Gamma_{TM}\rvert$ $\phi_i = 60°$
5	15	0.04	0.03	0.07	0.01
20	15	0.11	0.08	0.18	0.02
5	25	0.07	0.05	0.11	0.02
20	25	0.18	0.12	0.29	0.03
100	25	0.59	0.45	0.78	0.08

Table 3.1 shows the wall reflectivity values, Γ_{TE} and Γ_{TM}, for transverse electric and transverse magnetic components of the incident wave. These results show that only a small fraction of the signal is reflected by the wall (especially in the HF band). For example, about 80% of the incident field is transmitted through the wall at 20MHz independent of incidence angle for concrete walls as thick as 25cm. It can be seen that reflection coefficient significantly increases with frequency. The main point of this analysis is to show that the HF band is desired for source tracking in indoor settings, since at this frequency the multipath becomes much less significant than at higher frequencies. In the rest of this section, we present full-wave simulation results of a typical complex indoor propagation scenario to quantitatively investigate and justify the choice of HF band for source tracking in cluttered environments.

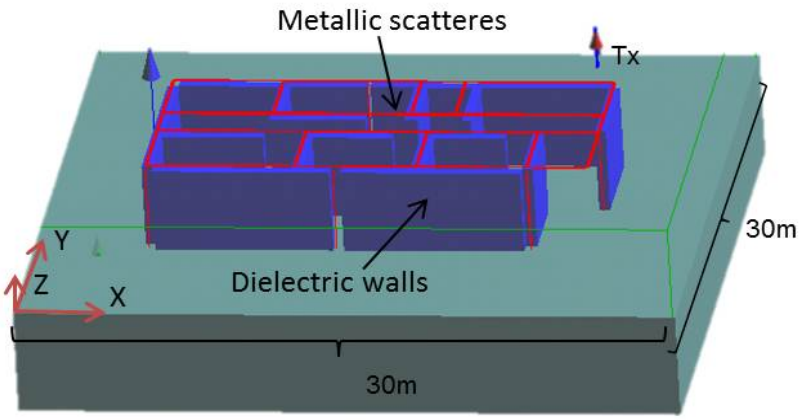

Figure 3.2: Full-wave simulation setup to investigate field coverage as a function of frequency is shown. Several steel cylinders are included as support for the dielectric walls and the ceiling (similar to realistic buildings). The dielectric ceiling is not shown in this picture. A short dipole located outside is utilized as a Tx antenna and field coverage inside and outside the building is analyzed.

3.3.1 Full-wave simulation in the presence of dielectric and metallic scatterers

In order to study the effect of multipath using a more realistic model, we used a second model based on a Finite-difference time-domain (FDTD) full-wave solver. The full-wave simulation is important because it takes into account near-ground wave propagation and antenna coupling effects that ray tracing does not consider. We will consider the setup given in Fig. 3.2 which will be used to investigate the level of multipath as a function of frequency using field coverage comparison. The performance of the proposed tracking technique will also be analyzed. The geometry used for this simulation is a complex building setting consisting of several walls and the ground. The walls and the ceiling are modeled as dielectric slabs. The dielectric properties of the walls are chosen to be that of cinder block ($\epsilon_r = 4 + 0.9j$). The ground is modeled as a concrete half-space medium. The dielectric constant of concrete in the HF range is assumed to be $\epsilon_r = 4.5 + 0.9j$. To make the environment more realistic, a metallic frame is considered as support for the dielectric walls and

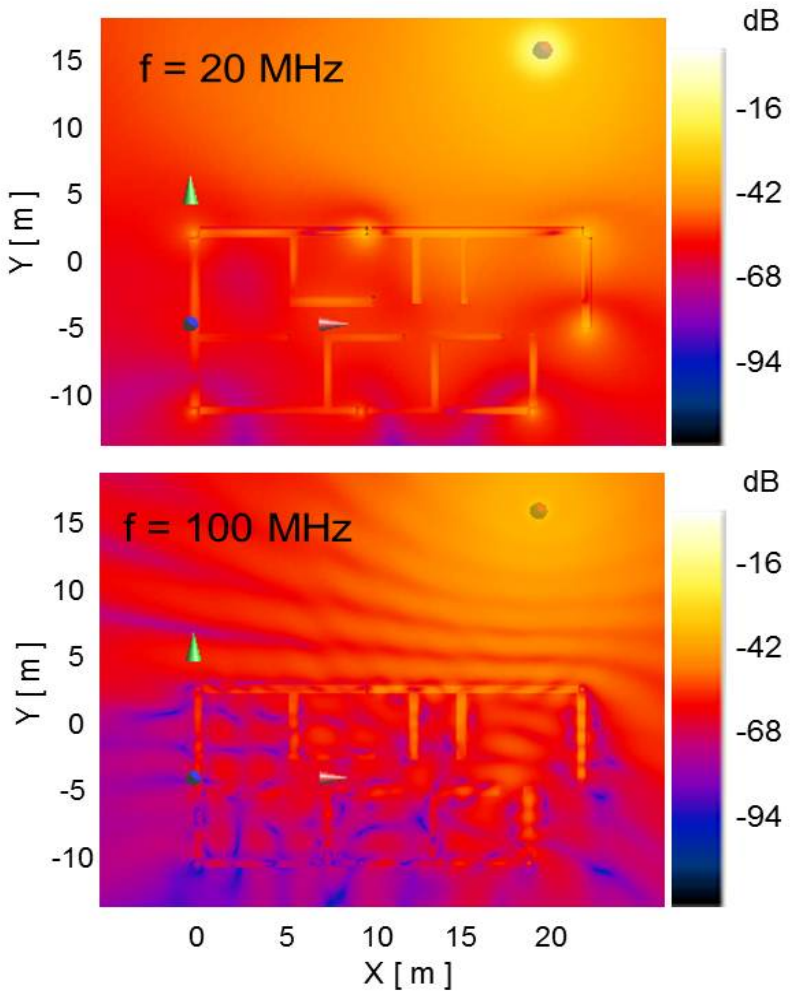

Figure 3.3: Comparison of magnitude of the vertical component of the electric field coverage as a function of frequency on a plane parallel to the ground (at a height of $z_o = 1.5m$) for the setup given in Fig. 3.2.

ceiling (Fig. 3.2, dielectric part of the ceiling is not shown). A z-directed short dipole located outside the building is utilized as a Tx antenna and the electric field coverage is computed as a function of frequency. It should be noted that absorbing boundary conditions have to be correctly placed to avoid diffracted components from the edges of the ground. For this reason perfectly matched layer (PML) boundary conditions without any air padding are utilized to simulate infinite ground.

The vertical component of the electric field on a plane parallel to the ground at

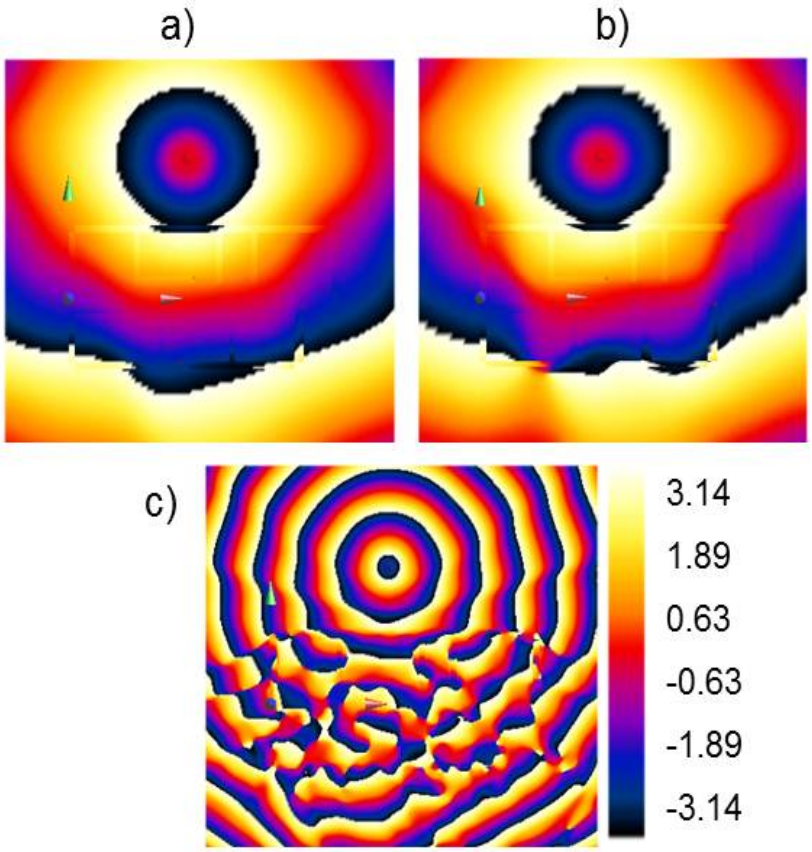

Figure 3.4: Phase map of the geometry given in Fig. 3.2 where the Tx antenna is positioned at (9,10,1.5). The phase map is given in a) with ground and dielectric walls and ceiling at 20MHz, b) with metallic scatterers in addition to dielectric scatterers at 20MHz, and c) with metallic scatterers in addition to dielectric scatterers at 100MHz.

a height $z_o = 1.5m$ is plotted for two different frequencies (20MHz and 100MHz) as shown in Fig. 3.3. As expected when a vertical dipole is used as Tx, the effect of the vertical metallic scatterers (used for reinforcing walls in realistic buildings) can be seen in the field coverage at both frequencies. But, the horizontal metallic scatterers are not significant since the radiated field is vertically polarized. By comparing the field coverage plots in Fig. 3.3, we note that at 100MHz the signal components scattered by the building walls, ground and ceiling become comparable to the direct field component causing significant fading and uneven field distribution. Of course, if the frequency is increased further (e.g. L or X band), the multipath level becomes

even more significant [46]-[47]. In addition, attenuation through the walls and ceilings becomes much larger making the possibility of source tracking using these frequencies challenging. We can see that the effect of the scatterers is much less prevalent at 20MHz. The fact that the multipath level is very small and that the direct path is the dominant component of the total received field is the main reason the HF band is considered. In Fig. 3.4, the phase map for the geometry given in Fig. 3.2 are given. As can be seen, at 20MHz (Fig. 3.4*a* and Fig. 3.4*b*), even in the presence of dielectric and metallic scatterers, the phase fronts inside the building are only slightly disturbed. When the frequency is increased to 100MHz (Fig. 3.4*c*), the effect of the multipath becomes more significant. At a given frequency, the error introduced on the tracking resolution due to the small multipath is first calculated by performing simulations with and without the building walls. Then, the highest frequency at which the error is within the intended resolution of the system is selected. After the frequency of operation is chosen, the performance of the proposed tracking approach is investigated. Here, we discuss the results of three sets of simulations based on a FDTD full-wave solver. The building geometry considered is the same as that of Fig. 3.2. A detailed simulation setup and parameters are given in Fig. 3.5.

In the first simulation, only the dielectric scatterers were considered. This is important because many residential houses do not include metals and instead use bricks or wood. The goal here is to study the effect of having mostly dielectric scatterers on the proposed source tracking technique. For this simulation, the receive array is kept stationary and the Tx antenna is moved along a straight line inside the building. For each Tx position, the received field at the receive antennas is recorded. It's obvious that when the Tx antenna is at the boresight of the Rx arrays

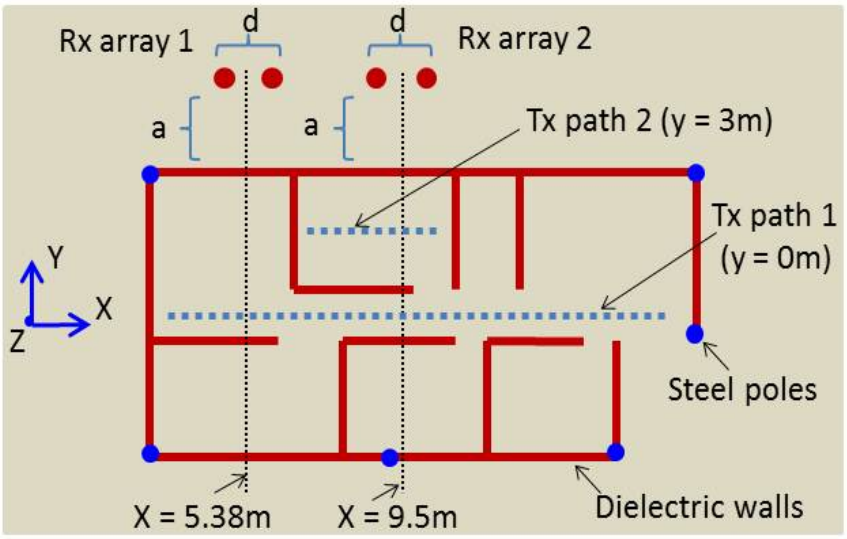

Figure 3.5: Top view of the full-wave simulation setup. The geometry of the problem is the same as the one shown in Fig. 3.2. For this case, the Tx antenna is moved inside the building while the Rx array is positioned outside. The simulations in this section use z-directed short dipoles Tx and Rx antennas.

($x = 5.38m$ and $x = 9.5m$ for Rx array 1 and Rx array 2, respectively), the phase difference between the received signals is zero. In this case the Tx antenna is moved (along Tx path 1 in Fig. 3.5) to vary the phase differences between the received signals. The same analysis could have been done by fixing the position of the Tx antenna and rotating the Rx array to create the phase differences. The DOAs for a given position of the Tx antenna are calculated from the center of both receive arrays. These DOA values are then used to compute the location of the Tx antenna based on the technique describe in Section 3.2. The plots given in Fig. 3.6 show the DOA calculated based on the phase and magnitude of the signals received by the two Rx antennas of array 1. For comparison, the same setup (without the walls) is simulated based an asymptotic Dyadic Green's function for a half-space medium which takes into account the near-ground propagation effects [83]. As described in the original work, by utilizing asymptotic Dyadic Green's function, the Norton surface waves that become prevalent in near-ground scenarios can be fully taken into

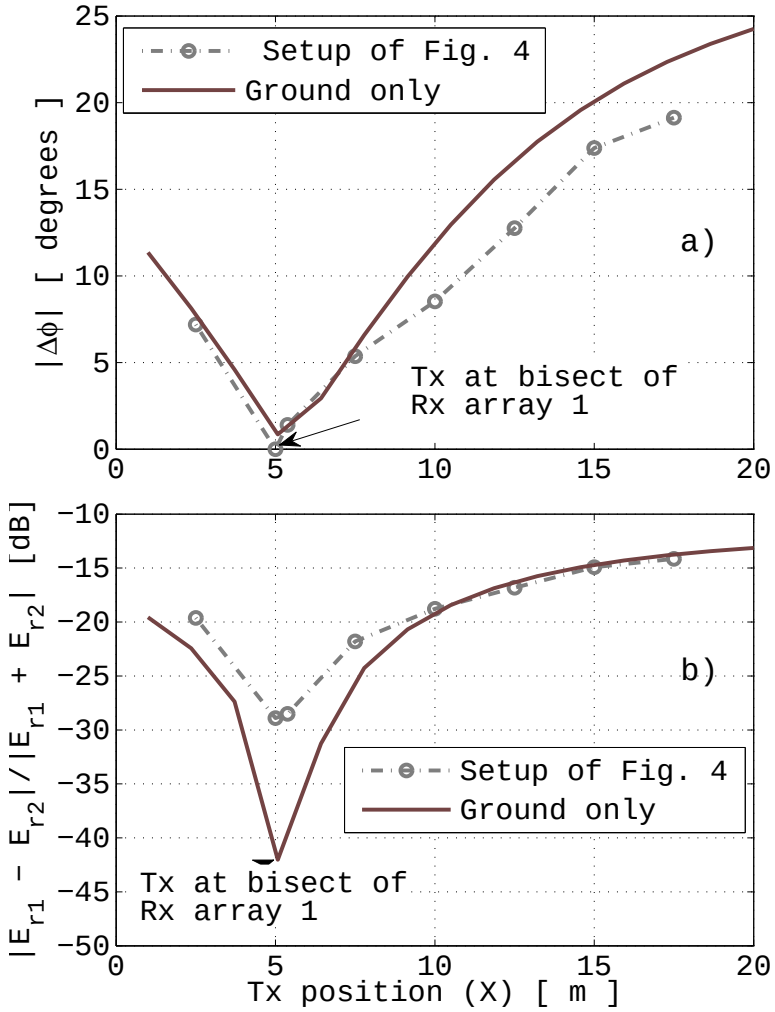

Figure 3.6: The geometry of the simulation is given in Fig. 3.4 ($d = 1.25m, a = 1m$). The source is moved along Tx path 1 and phase difference variation of the received signals at Rx array 1 is plotted in (a) and 3.3 is used to calculate DOA based on magnitude of the received signals.

account. The results confirm that even in the presence of scatterers such as walls and ground, the DOA of the signal can be successfully retrieved because the direct signal is dominant compared to the level of multipath in the HF band. It should be noted that the errors in the estimated DOA are caused by small level of multipath that still exists (it is much smaller than the direct path) and antenna coupling in the Rx array especially for larger DOA values which is described in Section 3.3.2. It should be noted that the proposed system needs to measure only small DOAs because the Rx arrays which are positioned on a rotating platform can rotate to keep the Tx antenna along the bisect of the Rx array. Essentially, as the Tx antenna moves, the Rx array rotates in such a way that the phase difference between the received signals at the Rx elements is at a global minima. The advantage of this approach is that the system does not have to measure large DOA values and hence can avoid DOA errors that can be significant (See Fig. 3.6*a*).

A second set of simulations for a more complex scenario is also performed. Since some buildings are built out of both metallic and dielectric materials, the performance of the proposed direction finding technique must be analyzed in the presence of both types of scatterers. For this simulation, thick cylindrical posts are placed at the various corners and junctions of the building (Fig. 3.2). A pair of short dipoles are used as a receive array (the bisect of the array is along $x = 9.5$). The received fields at each antenna is recorded by running the FDTD solver for various positions of the Tx antenna (Tx path 1 and Tx path 2 shown in Fig. 3.5). As can be seen in Fig. 3.7*a*, when the Tx antenna is moved along Tx path 2, the phase difference plot results in a null at the bisect of Rx array 2. Tx path 1 is also considered to investigate the performance of the proposed technique for various locations inside

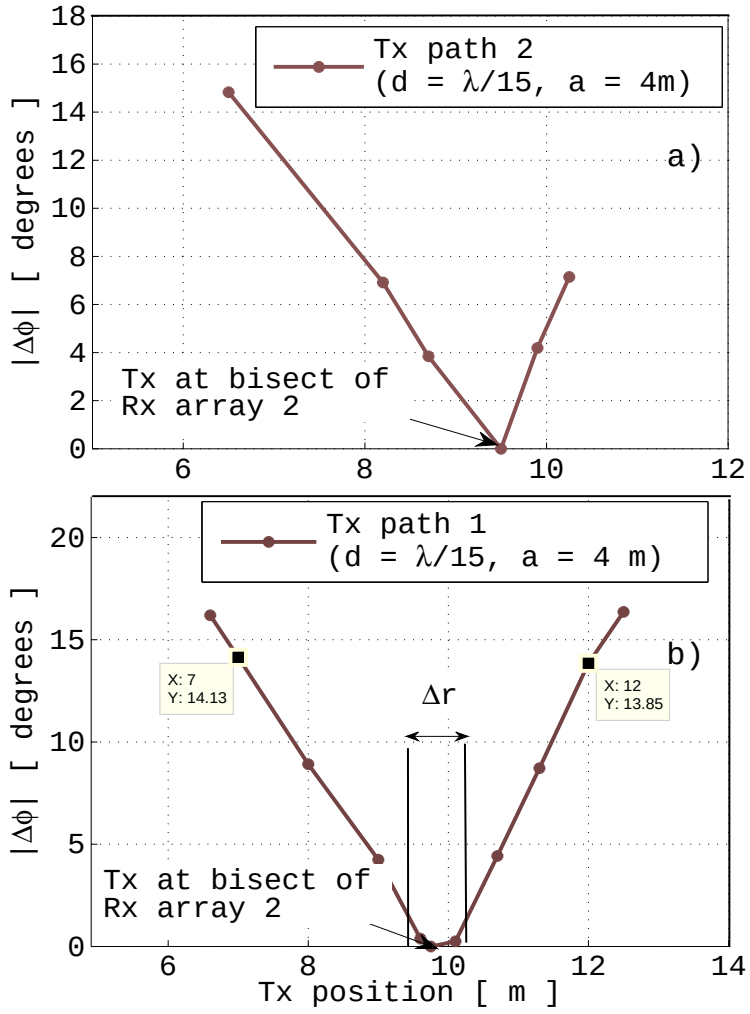

Figure 3.7: The geometry of the simulation is given in Fig. 3.5($d = 1m, a = 5m$). Phase difference variation of the received signals at Rx array 2 when the source moves along Tx path 1 (b) and Tx path 2 (a) are shown. Dielectric walls and metallic scatterers for the walls and ceiling are included in this simulation (Fig. 3.2).

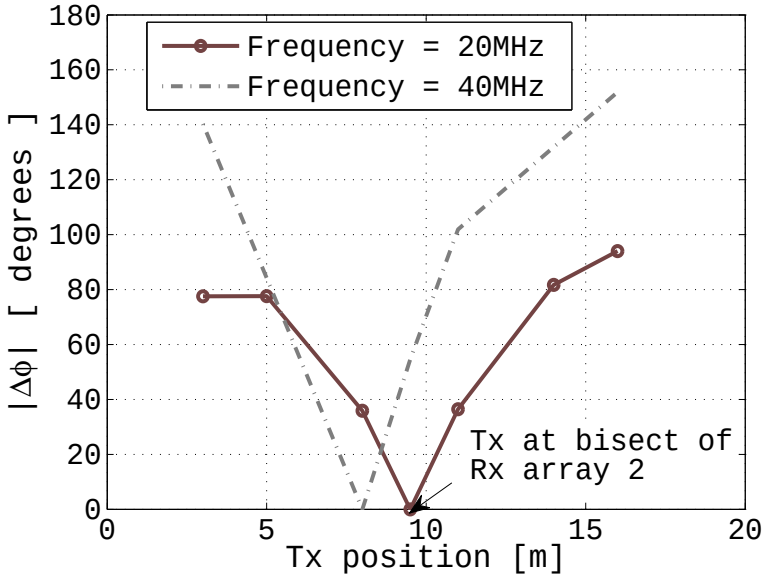

Figure 3.8: The geometry of the simulation is given in Fig. 3.5 ($d = 1.25m, a = 1m$). Phase difference variation of the received signals at Rx array 2 is plotted at 20MHz and 40MHz (for Tx path 1). Dielectric walls and metallic scatterers are included.

the building. Fig. 3.7*b*, the result for the case where the source moves along Tx path 1, shows a null at the correct location. Of course, there is a relatively small error in the estimated DOA values. For example, in Fig. 3.7*b*, we notice that when the Tx antenna is at x = 7 (2.5m to the left of the bisect of Rx array 2, see Fig. 4), the estimated phase difference is 14.13°. On the other hand, when the Tx antenna is at x = 12 (2.5m to the right of the bisect of Rx array 2), the estimated phase difference is 13.85°. The calculated phase difference based on the location of the Tx and Rx antennas is 14.03° for both cases. So, the errors in the retrieved phase differences are small (despite the presence of indoor scatterers). For this simulation d is $1m$ and a is $5m$.

In the third simulation, the effect of increased multipath level is investigated by comparing phase differences at 20MHz and 40MHz with the same geometry as the above two cases. The phase differences between the received signals at Rx array 2 are

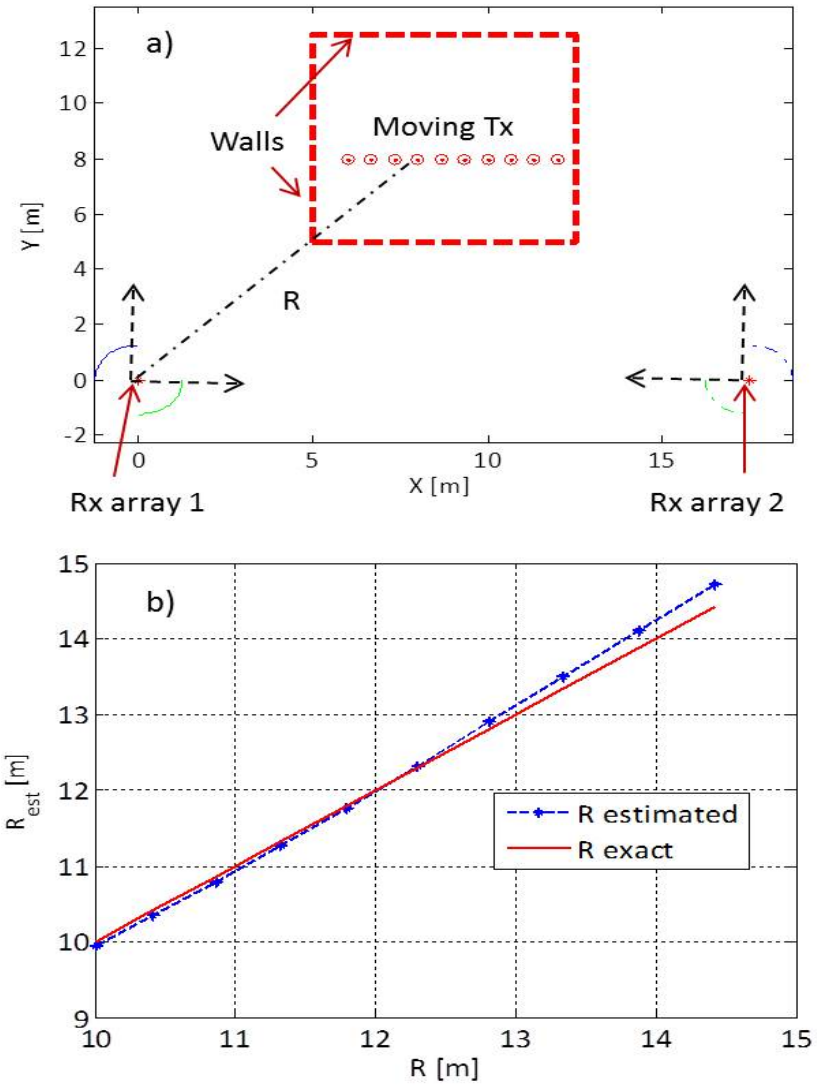

Figure 3.9: A comparison between actual and estimated distance between Rx array 1 and moving Tx inside a room (b). The geometry is shown in (a).

computed as the Tx antenna is moved along Tx path 1. The plots in Fig. 3.8 show that the error in estimated phase differences increase as the frequency is increased because the effect of the scatterers becomes more significant at 40MHz compared to 20MHz. To investigate the effect nearby scatterers, the receive array for this case was positioned very close to the wall unlike the previous case ($a = 1m$). The bisect of the receive array is correctly retrieved only at 20MHz. The slight asymmetry compared to the previous case (Fig. 3.7) in the result is caused by the close proximity of the antennas to the wall.

In addition to accurately retrieving the DOA from various TX and Rx locations, a simulation to compare the estimated distance between the Rx arrays and the moving Tx is also shown. It should noted that (as given in Fig. 3.14), if the DOA can be accurately measured from multiple points, the location of the Tx can easily be estimated. In Fig. 3.9, we show an example simulation comparing the actual distance between the Rx array and the Tx antenna to the estimated distance based on the proposed technique. It can be seen that even in NLoS scenarios, the error introduced is very small.

3.3.2 Antenna coupling analysis

Because of the close proximity of the antenna elements in the receive array ($\lambda/15$), the effect of the interelement coupling has to be investigated. One way to analyze the coupling as it relates to direction finding is by using the scattering matrix (S-matrix) of the antenna system. The three antenna system consisting of the Tx antenna and the two Rx antennas on the receive array can be modeled as a three port network which can be represented by a 3x3 S-matrix (Fig. 3.10). Because of

Lorentz reciprocity, the S-matrix is symmetric. For our application, S_{12} and S_{13} are the important elements since these elements are responsible for interelement coupling between the receive antennas. S_{12} can be calculated by first exciting the Tx antenna (port P_1) and measuring the voltage at port P_2 while P_3 is matched to 50 ohm. S_{12} is then computed by taking the ratio of V_1 to V_2. When the two Rx antennas are illuminated by the radiated field from the Tx antenna, the scattering from Rx_2 induces a voltage across the port of Rx_1 and vice versa. So, the received field at Rx_1 consists of the direct field from the Tx antenna and a small scattered component from Rx_2 determined by the radar cross-section of the short dipole and the scattering angle (θ_s). To quantify the the effect of antenna coupling on the retrieved DOA, a full-wave simulation consisting of three short dipoles is carried out with no other scatterers present (Fig. 3.10). The error in the retrieved DOA is then calculated by taking the difference between the retrieved DOA (from simulation) and exact DOA (based on geometry). It should be noted that when the Tx antenna is at the bisect of the two identical receive antennas, the error in phase difference due to antenna coupling is zero. If the Tx moves on the azimuth plane (the x-y plane in Fig. 3.10), a small error is introduced on the phase difference. The results of the full-wave simulation (errors due antenna coupling) are shown in Table 3.2. The results show, for small antennas whose bistatic scattering is almost invariant with the bistatic angle, the resulting errors are quite small. The coupling effect has been fully taken into account in the full-wave simulation analysis presented. Also, a scenario where the dipole lengths are slightly different was simulated. There was no significant change in the error compared to identical antennas.

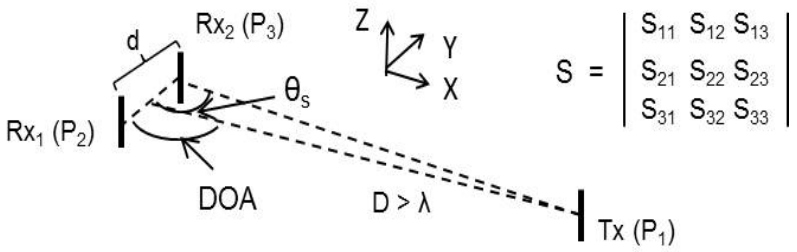

Figure 3.10: The three antenna system used for antenna coupling analysis

Table 3.2: Antenna coupling analysis using full-wave simulation (see Fig. 3.10)

d [λ]	DOA [°]	$\lvert DOA_{est} - DOA_{exact} \rvert$[°]
$\lambda/15$	53.1	1.5
$\lambda/15$	64.6	0.9
$\lambda/15$	80	0.3
$\lambda/15$	90	0
$\lambda/15$	100	0.3

3.4 Source Tracking System Prototype

Having performed numerical analysis of direction finding in multipath environments, the next step is to validate our proposed approach using measurement results. In order to realize the proposed system, various components need to be designed, fabricated and tested. Assuming a narrowband signal in the HF range is transmitted by the miniaturized antenna, the signals at the two receiving antennas are first filtered by narrowband, low-loss filters with high stop-band rejection. The filtering stage is important to reduce the out-of-band noise and maximize signal-to-noise ratio (SNR) as much as possible. Assuming a zero-mean gaussian noise, the standard deviation of phase in terms of SNR is given by $\sigma_\phi = 57.3°/\sqrt{SNR}$. The SNR is an important quantity because it is the main limiting factor determining the smallest phase difference that can be accurately measured which in turn affects the maximum tracking resolution. After the the filtering stage, the signals are amplified by low-noise, high gain amplifiers. Since the components used could introduce phase

differences between the two signal lines, an electronic phase shifter is connected in one of the lines for calibration. The next component which is the phase difference amplification (PDA) circuit is a four-port passive network inspired by the hearing mechanism of a fly that essentially amplifies the phase difference between the input signals into a much larger value that can then be measured accurately. The output signals of the Phase difference amplification (PDA) circuit are sampled by a highly sensitive two channel 16-bit A/D converter. In this section, we will first describe the design and fabrication of a miniaturized low-profile HF antenna. The principles of operation and design of the four-port PDA circuit is also described. We concluded the section with test results performed in various environments.

3.4.1 Highly miniaturized low-profile HF antenna

Conventional antennas in the HF range are prohibitively large especially for applications such as tracking of small robotic platforms where the antennas are to be integrated. For our prototype, a very low-profile miniaturized antenna with vertical polarization and omni-directional pattern, operating in the HF band is utilized. The length and width of the antenna are both $\lambda/100$ while the height is $\lambda/300$ at 20MHz. For such extremely low-profile condition, the radiation efficiency becomes very small. One way of improving the gain of low-profile vertically polarized antenna is to use multiple vertical elements that are in phase which is equivalent to having a vertical short dipole with higher height. This approach is used to design the Tx antenna in the proposed source tracking system. In order to minimize the size of the vertically polarized antenna with two in-phase vertical elements, a modified T-type 180° phase shifter utilizing a capacitive impedance inverter is used [91] -[92]. As can

be seen in Fig. 3.11*a*, the currents on the feed and shorting pins (I_1 and I_2) that would normally have 180° phase difference are forced to flow in the same direction by using a T-type 180° phase shifter. First, the capacitance value is determined by the limited area of the capacitive plate (150mm X 150mm). Next, in order to achieve 180° phase shift of the T-type phase shifter at the frequency of interest, the inductance value is calculated. The values used in our design are L = 10μH and C=10pF. It should be noted that these values are just for ideal circuit simulations. In the actual antenna geometry, the parasitic inductance of feeding and shorting pins and dielectric constant of thin substrates of top and bottom plates also affects the values. For this antenna, a lumped element capacitor can not be used as that would cause an out-of-phase conduction current to the ground which would result in radiation cancelation. For this reason, the required capacitor is realized by using an open stub. Finally, for a given lateral dimension and height, the miniaturized antenna structure is designed by optimizing the geometry of the open stub to get omnidirectional radiation pattern. The proposed antenna was successfully fabricated and integrated with voltage controlled oscillator (VCO) operating at HF-band and a battery, as shown in Fig. 3.11. The VCO is used to tune the frequency of operation. Having the battery integrated with the antenna is important because if a cable is used to feed the antenna, the cable itself will become part of the antenna (λ at 23MHz is $\sim$13m), leading to a shift in the resonant frequency, poor impedance matching and radiation pattern. The measured antenna gain is -29.2dBi, which is similar to the simulated gain of -28.1dBi. In comparison, the gain of the spiral-shaped inverted-F antenna (IFA) is -34.4dBi which is 5.2dB lower than that of the proposed antenna. The radiation pattern of the proposed antenna is given in Fig. 3.12.

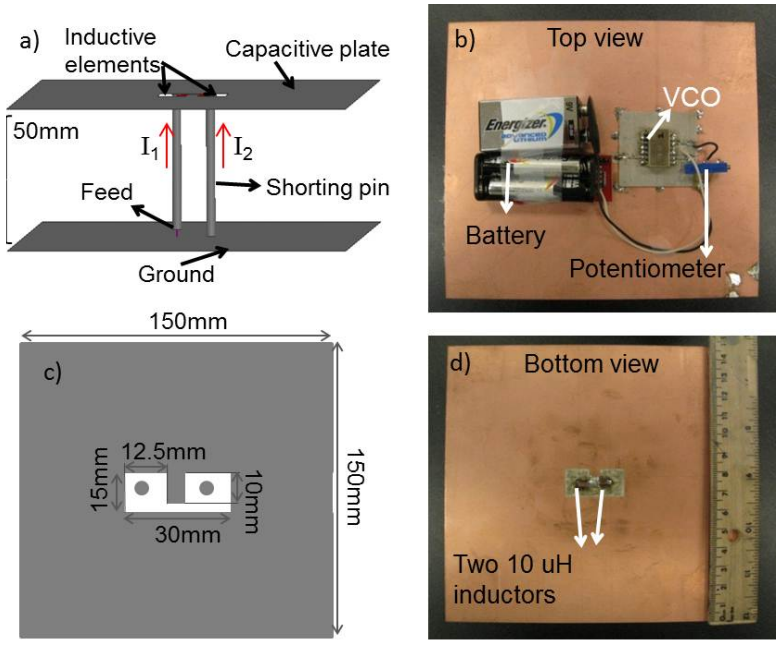

Figure 3.11: The low profile miniaturized antenna designed to operate at 22.8MHz and the optimized dimensions are shown(a,c). The top and bottom view of the fabricated antenna are shown in b and d, respectively. The inductive and capacitive elements form a realization of a 180° T-type phase shifter. This forces I_1 and I_2 to be in phase(a).

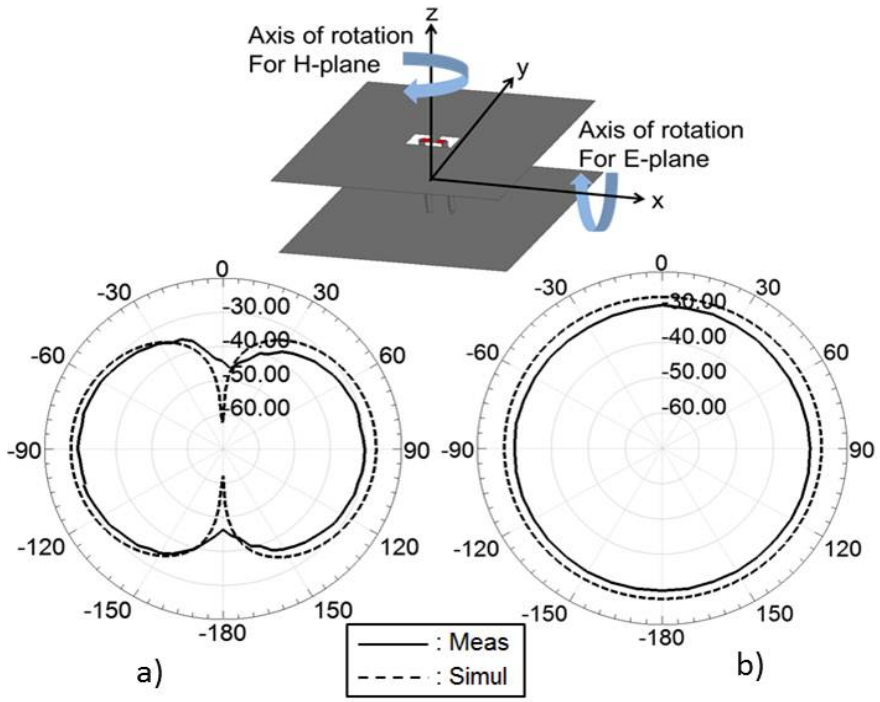

Figure 3.12: Measured and simulated radiation patterns of the proposed antenna in (a) E (=yz) plane and (b) H (=xy) plane.

3.4.2 Phase difference amplification (PDA) circuit inspired by Ormia's hearing mechanism

The receive end in our system prototype consists of two antennas operating in the HF range that are very close to each other in terms of wavelength ($\lambda/15$ at 20MHz). One of the challenges that arise at such low frequencies is that the phase difference between the two received signals becomes too small to be accurately measured. Also, the resolution of tracking is limited by the smallest phase difference that can be measured. The smallest measurable phase difference is in turn determined by the SNR. Given a receive array and a Tx antenna as depicted in Fig. 3.13, the phase difference between the signals at the Rx antennas changes slightly as the Tx antenna moves a distance Δr. If the system can accurately measure the phase difference introduced because of the motion of the Tx antenna, then that means the system can achieve a spatial resolution of Δr. A plot that relates the spatial resolution to Tx-Rx separation and the minimum phase difference that can be measured is presented in Fig. 3.14. For example, if the system can accurately measure a phase difference of 1° and the Rx antennas on the array is separated by $1m$, then the best possible spatial tracking resolution is about $35cm$ for a Tx-Rx separation of $10m$. Since the measurement of small phase differences is challenging, we need a way to enhance the accuracy in phase difference measurement without increasing the baseline distance.

To tackle the challenge associated with measuring very small phases, we utilize a phase difference amplification technique inspired by the hearing mechanism of a fly called Ormia Ochracea. Ormia is a small fly which is known for its accurate directional hearing. This ability helps Ormia loacalize the mating call of the male cricket. Ormia's ears are separated by a mere 1.2mm ($\lambda/60$ at 4.5KHz). This close

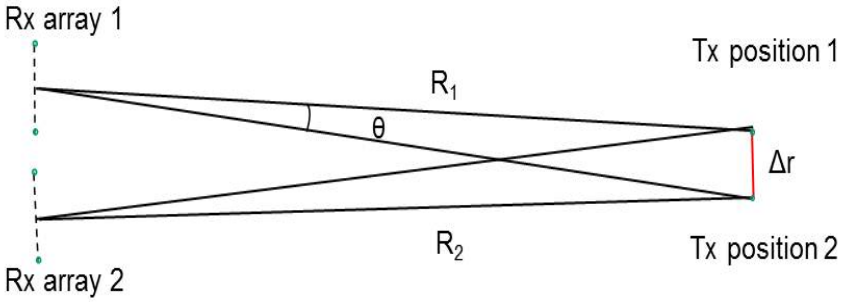

Figure 3.13: Geometry used to analyze the minimum phase requirement for a given tracking resolution.R_1 and R_2 are the distances between the center of the Rx arrays to the first and second positions of the source.

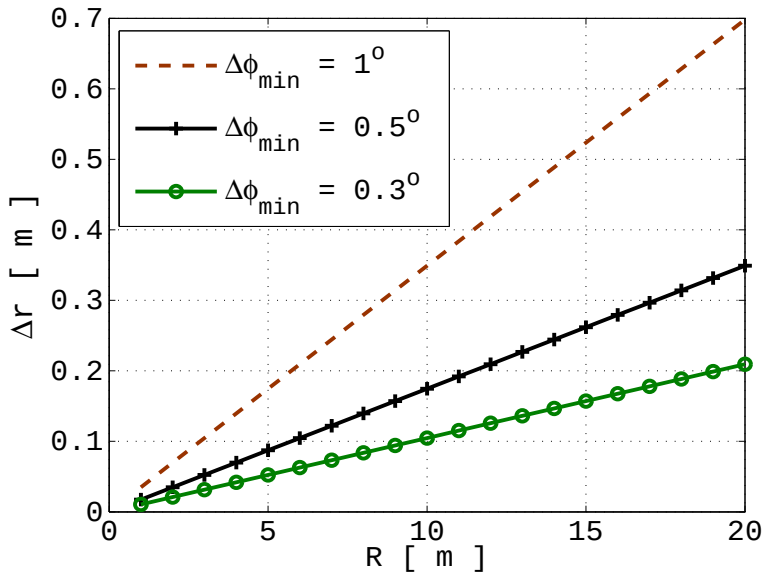

Figure 3.14: The azimuth resolution plotted against Tx-Rx separation. The three curves show the resolution for various values of minimum phase difference between received signals that can accurately be measured ($\Delta\phi_{min}$).

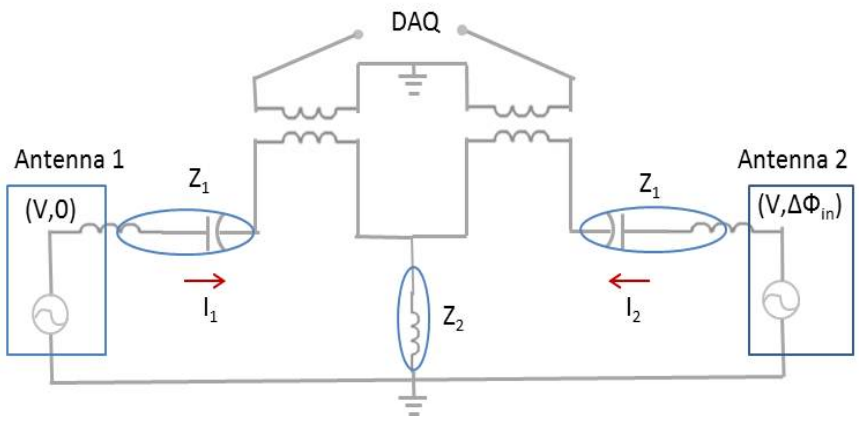

Figure 3.15: Phase difference amplification circuit designed to amplify small phase differences.

proximity causes the arrival times of the sound pressures at the two ears to be less than 1 to 2 microseconds [93]-[94]. So, how is that Ormia can sense the direction of sound with resolution as small as 1°? Ormia uses a sophisticated structure that mechanically couples its two ears, the effect of which is the amplification of the phase difference to values that are amenable to neural processing. The electrical analogous of Ormia's phase difference amplification mechanism is first investigated in [95]. The schematic in Fig. 3.15 shows a realization of this approach. The coupling circuit consists of various lumped elements and two transformers used to measure currents I_1 and I_2. So, by optimizing the values of the lumped elements, the phase difference between I_1 and I_2 dramatically increases compared to the phase differences between the input signals. Assuming the amplitudes of the input signals are almost the same, the output phase difference ($\Delta\phi_{out} = |\phi(I_2) - \phi(I_1)|$) can be approximated in terms of the input phase difference (phase difference between the received fields at the two Rx antennas) as

$$\Delta\phi_{out} = \angle\left(\frac{e^{j\Delta\phi_{in}} - K}{1 - e^{j\Delta\phi_{in}}}\right), \; K = \frac{Z_2}{Z_2 + Z_1} \tag{3.3}$$

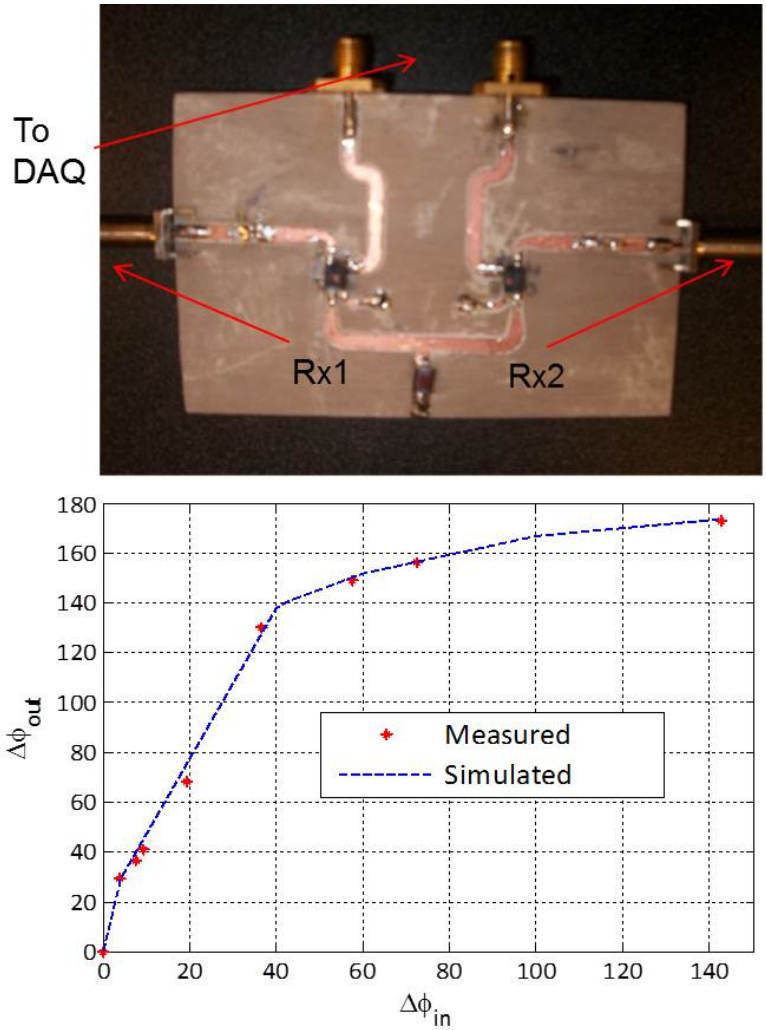

Figure 3.16: A picture of the fabricated PDA circuit where Rx1 and Rx2 are the ports that connect to the two receive antennas is shown. The simulation and measurement results of the phase difference amplification are given in the plot.

where, $\Delta\phi_{out}$ the output phase difference. Z_1 and Z_2 are the series and shunt impedances,respectively (as given in Fig. 3.15). To get an insight into how the circuit works, let's look at two extreme cases which are when the impedance of Z_2 is zero and infinity. When $Z_2 = 0$ ($K = 0$), the output phase difference will be same as the input phase difference. On the other hand, if Z_2 is very large ($K \sim 1$), the phase difference becomes $\sim 180°$. When Z_2 is finite and larger than Z_1, the phase difference between the two currents will be an amplified version of the original phase difference. The way this circuit is optimized is based on the following two conditions: 1) Achieving the desired phase amplification which is determined by the phase amplification factor (K), and 2) Maximizing the power at the output channels of the PDA circuit (by achieving impedance matching at each stage of the receive circuit). The values chosen in the final design are $K = 0.84$ and $Z_1 = j120\Omega$. The circuit was fabricated and tested using a signal generator, an electronic phase shifter and an A/D converter. As can be seen in Fig. 3.16, there is a very good agreement between measured and simulated results. It should be noted that this circuit is only necessary when the input phase differences are relatively small ($\leq 10°$). Larger input phase differences can be directly measured without amplification.

3.4.3 System Integration and Test

The receiver module as can be seen in Fig. 3.17 consists of two signal lines each having a narrowband, low-loss filter connected to the two miniaturized dipole antennas ($\sim \lambda/15$). A high-gain low-noise amplifier is then used to amplify each signal by about 40dB. However, the noise that passes through the filters with the signal of interest will also be amplified. It's vital to minimize this noise to achieve

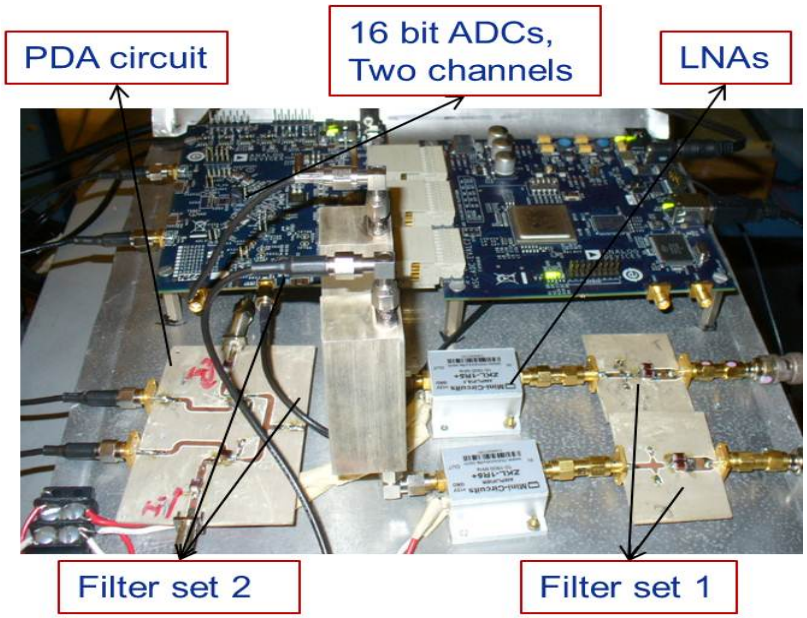

Figure 3.17: Receiver module including a sensitive pair 16 bit ADCs, phase amplification circuit, various filters, amplifiers.

the maximum possible SNR. For this reason, a second set of band-pass filters with high stop-band rejection are used. The various parameters of the system are listed in Table 3.3. The second column in the table lists the calculated or simulated values for the Tx antenna gain (G_t), Rx antenna gain (G_r), the output power of the VCO used to feed the Tx antenna (P_{Source}), the received power (P_r) and the distance between the Tx and Rx antennas (R). The third column of the table lists measured values for the same parameters. The antenna gains were measured outside where the multipath effects were minimized by positioning one antenna at higher elevation relative to the other antenna [91].

Table 3.3: A comparison of calculated and measured received system parameters

	Calculated/Simulated	Measured
Gt [dB]	-26	-28
Gr [dB]	-12	-13
Freq. [MHz]	22.8	22.8
$\lambda[m]$	13.27	13.27
$P_{Source}[dBm]$	8	8
$P_r[dBm]$	-55.54	-53
$R[m]$	20	20

With the current setup, at the maximum Tx-Rx separation considered (20m), an SNR well over 20dB was achieved. It should be noted that this noise is not thermal noise, but is caused by signal interference and thus the error generated by it in both channels are coherent. This makes it possible to improve the DOA measurement by subtracting the coherent components and hence thermal noise uncertainty is not the main factor. Also, one way to improve the current system is by designing extremely narrowband filters with high stop-band rejection which will further improve the Signal-to-interference ratio (SIR). The downside to using filters in the HF band based on lumped element components is that such filters suffer from low Q and/or high insertion loss. Other types of filters such as dielectric resonator filters and coaxial resonator filters which usually have high Q maybe used for better accuracy.

The Tx and Rx antennas are also tuned to maximize transmit and receive power, respectively. Without any amplifiers and filters, the received power is -53dBm at 20m Tx-Rx separation. As can be seen in Table 3.3, the received power is similar to the expected value. This measurement was done both indoor and outside using a spectrum analyzer to estimate the SIR. The fact that we get similar received power results for both the indoor and outdoor cases further confirms the minimal effect of multipath at this frequency. For a Tx-Rx separation of varying from 5m to 20m, the source tracking system was tested in various environments. We first tested the system for cases where there was a line of sight between the Tx and Rx antennas. The measured results were also compared with simulated results based on the half-space dyadic Green's function to capture the effect of the ground accurately. In all the measurements presented, the signals at the Rx antenna elements are recorded by keeping the Tx antenna stationary and rotating the Rx array in the azimuth

Table 3.4: Source tracking system test scenarios

Case	Tx/Rxs location	Line of sight?	Main Scatterers
1	Outdoor/Outdoor	Yes	Ground
2	Indoor/Indoor	Yes	Ground & Walls
3	Indoor/Indoor	No	Ground & Walls

plane about the center of the Rx array (One case is shown in Fig. 3.18). In the results that follow, we choose 0° rotation as the case when the Tx antenna is at the bisect of the Rx array. In Fig. 3.19*a*, the phase difference comparison between measured and simulated results for Case 1 (see Table 3.4) show very good agreement. The mean error for this case is 0.78°. For each Tx position, the phase difference is measured a minimum of five times. Errors are then calculated based on measurement and simulated results. More importantly, the two channel 80MSPS A/D converter acquires about 16000 samples. The FFT process essentially averages over the samples in 0.2ms (averages over 4000 cycles of the signal). By referring to Fig. 3.14, we see that this error in the retrieved DOA results in a spatial tracking resolution of less than a meter. The slight asymmetry in the measured result and the overall error is caused by measurement errors and the effect of antenna coupling between the Rx antennas as discussed in Section 3.3.2. Measurement errors come from inaccuracy in determining the location of the antennas especially for NLoS scenarios and differences in the performance of Rx antenna elements. The small multipath effect also contributes to the error. The result in Fig. 3.19*b* (Case 3, Table 3.4) shows that the proposed system works in NLOS case as well. The setup for this case is given in Fig. 3.18.

Table 3.5: Comparison of the proposed system with existing techniques [96]-[97]

System	DOA accuracy [°]	Meas. scenario
TCI7235 (Wattson-Watt)	10	Free space
DDF255 (Rohde & Schwarz)	2	Free space
TCI 802C (Wattson-Watt)	2	Free space
Proposed system	≤ 1	Indoor,outdoor

It is worth comparing the proposed system to the state of the art commercial

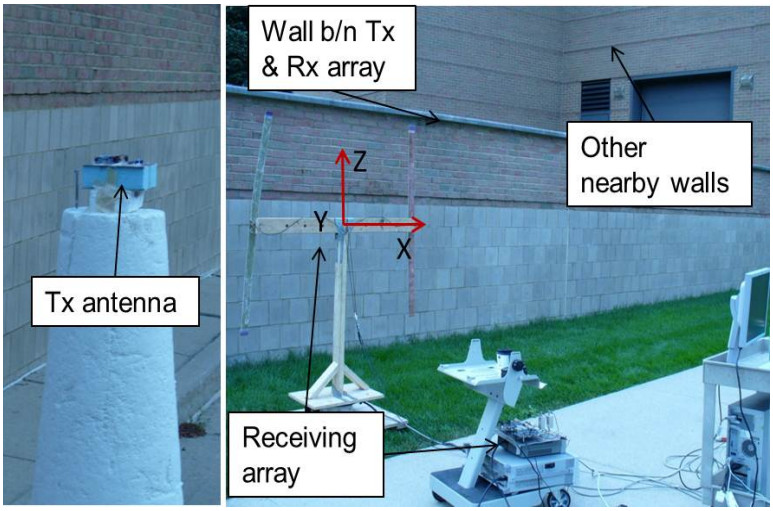

Figure 3.18: Measurement setup of Case 3 in Table 3.3 (NLOS case), Tx was positioned at the boresite of the receiving array on the X-Y plane. The Rx array and is then rotated about the Z-axis to investigate the phase difference variation.

DF systems. In the literature there are not many HF DOA retrieval techniques and measurement results for NLoS environments that we could make direct comparison with. Table 3.5 lists a few commercial systems and their accuracy compared to the proposed system.

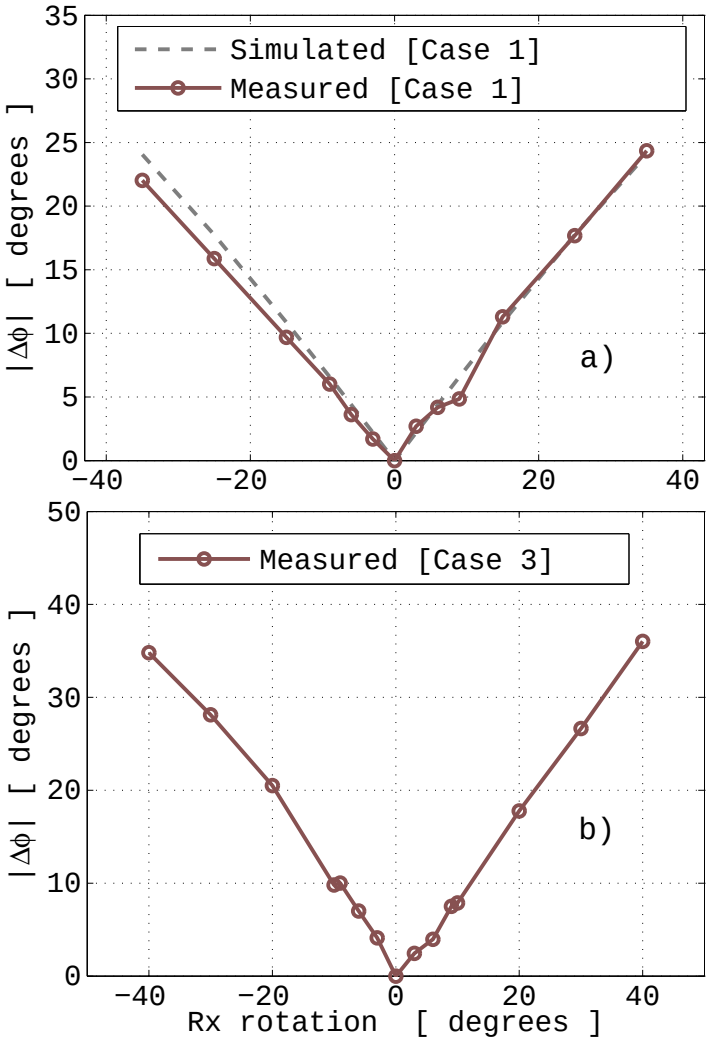

Figure 3.19: Measurement results and comparison with simulation for the Cases listed in Table 3.4.

CHAPTER IV

Subsurface Imaging based on Distributed Near-ground Sensors

4.1 Introduction

In this chapter, we propose a 3D high-resolution subsurface imaging approach based on non-uniformly distributed near-ground sensors operating in the VHF range. The imaging approach uses ultra-wideband near-field focusing. The system is envisioned to utilize transceivers mounted on robotic rovers or flyers (Fig. 4.1). With operation at the VHF band, better ground signal penetration and long range coverage can be achieved. Furthermore, by utilizing large bandwidth, the depth resolution can be improved. The advantage of a rover based distributed near-ground sensor network is that it can provide high transverse and depth resolution, possible autonomous data collection capabilities, and is well suited for the detection of deep targets (a few meters) as well as efficient imaging of large areas such as mine fields to help in demining and UXO clearance effort. Also, by positioning the Tx and Rx antennas close to the ground (less than λ), the direct and geometrical optics reflected signal from the ground almost cancel out and Norton surface waves are the dominant component of the direct field [83]. This unique property of near-ground sensors is exploited in the proposed approach as the direct signal in the case of near-ground an-

Figure 4.1: Transceivers and geolocation systems are mounted on robotic rovers or flyers that move in specified routes and acquire data about the subsurface environment (Image background borrowed from [6]).

tennas is less than the case of antennas that are well removed from the ground. One of the main challenges is overcoming issues related to the design of a compact and low-profile antenna in the proposed frequency range with good bandwidth. For this reason the idea of using multiple narrowband antennas is investigated. Essentially, the fundamental frequencies and the higher order harmonics of a few narrowband antennas (operating at the lower VHF band) are combined to achieve a larger combined bandwidth. Since the electromagnetic properties of the subsurface medium needs to be modeled based on the various variables including soil textural compositions, soil moisture, frequency, and dielectric profile of the subsurface medium, an appropriate soil dielectric model in the frequency of interest is required. The soil dielectric model is to be used to develop the forward scattering model as well as to improve the computational efficiency of the inversion algorithm.

The chapter is organized as follows. In Section 4.2, an accurate forward model for realistic subsurface environments based on a vertically stratified medium is presented. A soil dielectric model originally developed for the UHF band based on [98] is modified and validated at the VHF range with measured results available in the literature. The sensitivity analysis in the frequency of interest (Lower UHF and VHF) is performed to assess the signal penetration depth for realistic soil textural

compositions and soil moisture. In Section 4.3, the proposed imaging algorithm along with validation of the approach based on numerical results is discussed. Frequency analysis of the inversion algorithm relating both the bandwidth and number of frequency points to the depth resolution along with a scheme to reduce the number of frequency points is proposed. Furthermore, sensitivity analysis of the accuracy of the background dielectric profile as it relates to the imaging resolution is discussed. A scale model measurement to validate the proposed approach is performed in the laboratory and the results are presented in Section 4.4.

4.2 Subsurface scattering model and analysis

A realistic forward model that accurately captures the change in phase and magnitude of the electric field radiated by the transmitting antenna and received by each sensor is an essential element which is required both for signal penetration depth (SPD) analysis as well as to create synthetic data for validation of the subsurface imaging algorithm. In this section, an accurate forward model along with a VHF soil dielectric model and analysis of SPD in realistic subsurface environments are described.

4.2.1 Forward scattering model

Given a dielectric or metallic target, such as UXO, buried under an inhomogeneous soil medium along with transmitting and receiving antennas located close to the top surface, the goal here is to accurately calculate the received field. It's often the case that the dielectric variation of realistic subsurface medium is mainly along the vertical dimension (varies with depth). Here, we model the ground as a

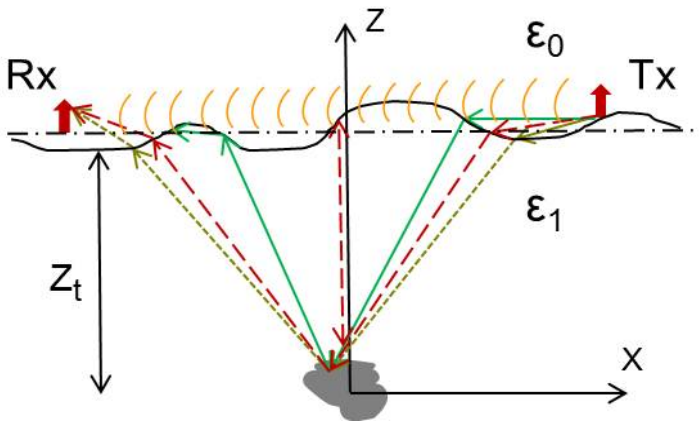

Figure 4.2: Near-ground Tx/Rx pair above a half-space medium and a buried target where the various scattering mechanisms are shown.

stratified dielectric medium composed of several thin layers where each layer has a constant electromagnetic properties resulting in a staircase approximation of the complex dielectric profile of the soil medium. The region under investigation is first illuminated with the electric field from the Tx antenna; the scattered field is used to image any possible inhomogeneity, aside from the stratified medium representing the background.

The required quantities for the forward model are the dielectric profile of the layered medium, the location of targets, and thicknesses of each layer. The electric field at the location of the receive antennas need to be accurately predicted. Assuming the target is not close to the surface, and noting that the interface between layers are diffuse, a first order approximation for calculating scattered field from the target to each sensor can be based on Geometrical optics by making use of the Fresnel transmission coefficients, phase delays and losses for each layer. This is especially valid for targets that are deeply-submerged for which the surface waves and other higher order effects can be ignored. As can be seen in Fig. 4.2, for a near-ground Tx/Rx pair, the received total field consists of several components including higher

order terms that Geometrical optics does not take into account. It turns out that the higher order terms are important only for shallow targets. However, the reflection from the ground and the direct coupling among the Tx and Rx antennas have to be correctly captured including Norton surface waves. The forward model for approach utilizes a vertically stratified medium to approximate the background dielectric profile as shown in Fig. 4.3. It should be noted that by varying the number of layers and the thicknesses of each layer, the background dielectric profile approximation can be improved. Antennas with wide beamwidth, which will be necessary to illuminate as much of the subsurface environment as possible, are more susceptible to stronger coupling compared to antennas with narrower beamwidth. It should be noted that unlike applications in communication areas, the goal is to have most of the energy propagate into the subsurface illuminating the region of interest while minimizing the direct coupling. In this regard, an interesting advantage of near-ground antennas that is exploited in our approach is that depending on the polarization choice the direct coupling can be made much smaller compared to systems that operate far from the ground. To investigate the coupling as a function of relative antenna orientation and separation, we used an accurate asymptotic approximation of the half-space dyadic Green's function [83]. In addition to the above techniques, full-wave simulation based on FDTD is utilized to analyze the proposed imaging approach.

4.2.2 A Semi-empirical VHF soil dielectric model

For a given soil mixture that has different soil textural class and moisture, the dielectric constant of the mixture is related to the properties of the individual components of the mixture including the dielectric constant, volume fractions and spatial

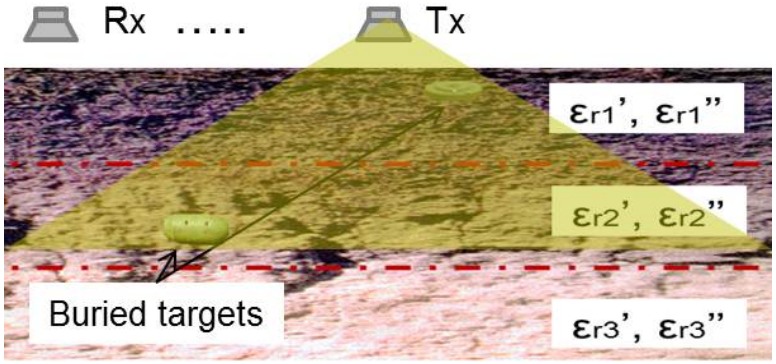

Figure 4.3: Vertically stratified medium used as a subsurface model. Each layer can be made arbitrarily thin resulting in a stair case approximation for the subsurface dielectric profile.

distributions among other things. Depending on size, the soil particles are divided into three types namely sand, silt and clay. By varying the relative percentages of the three soil particle sizes, the soil mixture's textural class can be determined. In the absence of water, the real part of the relative dielectric constant of soil varies between 2 and 4. A wet soil which is a mixture of soil particles, air pockets and water has dielectric constant that is significantly different from dry soil. In the literature, there are various empirical, semi-empirical and analytical models for the dielectric constant of soil especially at microwave frequencies [99]-[102]. However, for frequencies in the HF and VHF range, there is not a robust model that can be used to accurately predict the complex dielectric constant of various types of soils.

A semi-empirical soil dielectric model originally developed for microwave frequencies later extended to the UHF frequencies was proposed by Peplinski et al. [98]. For our purposes, the frequency range of this semi-empirical model was further extended down to VHF frequencies, assuming the empirical formulas do not change by much as the frequency is lowered. We then compared the real and imaginary parts of the dielectric constant predicted by this model to measured results available in

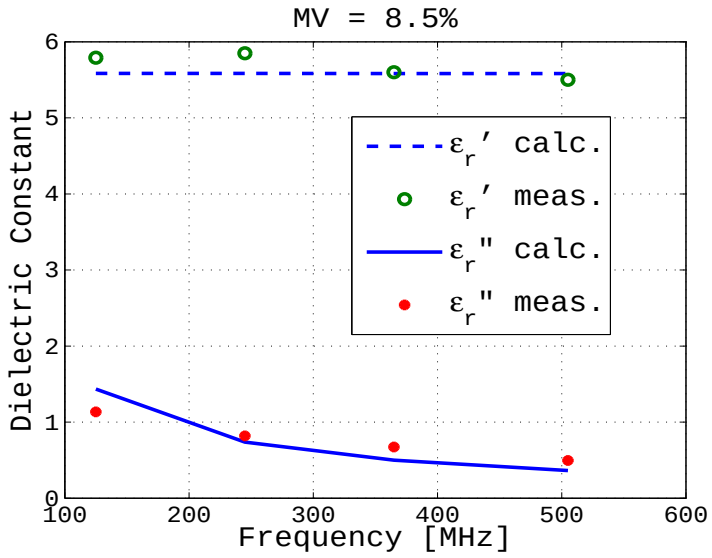

Figure 4.4: Comparison of the real and imaginary parts of the dielectric constants plotted against frequency for Sandy loam. Measured results are from [104]

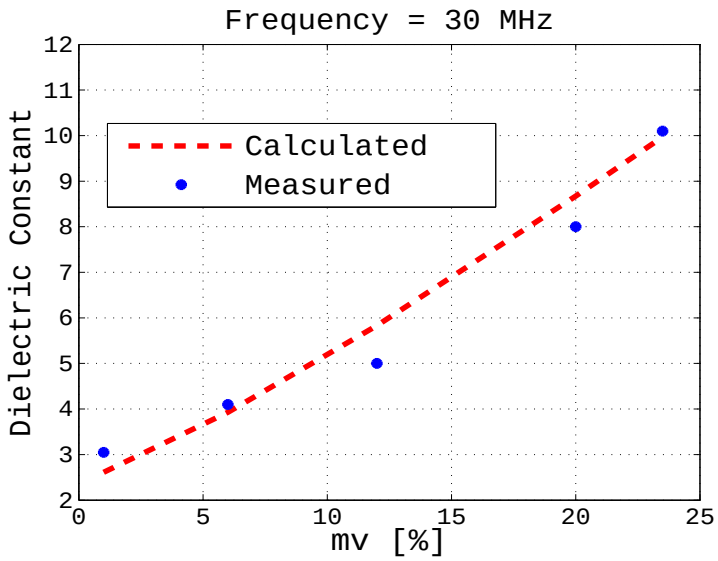

Figure 4.5: Dielectric constant comparison between calculated and measured results for clay loam, measured results are from [105]

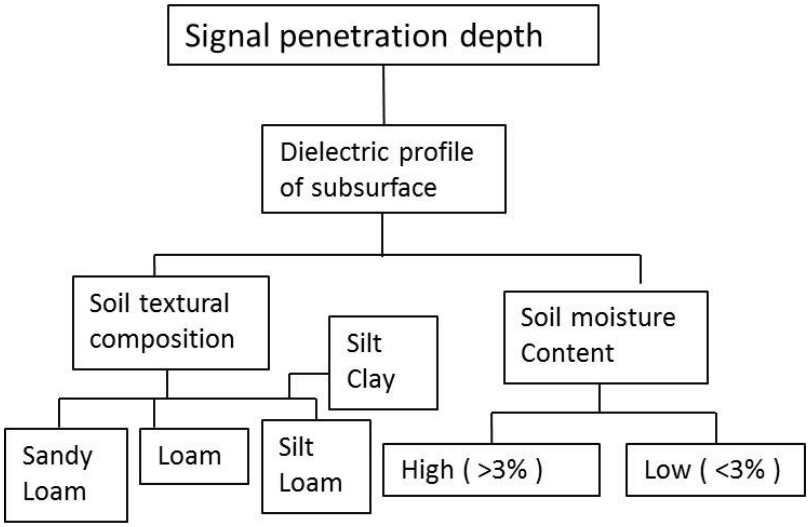

Figure 4.6: Signal penetration dependence chart

the literature [103]-[105]. The model for the frequencies of interest is then improved by introducing correction factors of $|mv - 1.3|/1.32$ and $|mv - 1.3|/3.3$ which are applied to the calculated real and imaginary parts of the dielectric constant, respectively. These values are chosen to adjust Peplinski's model (developed for frequencies above 300 MHz) to fit measured data for VHF frequencies. The equations needed to calculate the complex dielectric constant of a given soil mixture are included in Appendix B. The comparison results between measured and calculated dielectric constant of soil at lower UHF and VHF range are given in Fig. 4.4 and 4.5 showing very good agreement between the predicted and measured values.

4.2.3 Signal penetration depth analysis

Investigating the signal penetration depth for realistic subsurface environments by calculating the field at the location of the receivers as a function of frequency will be useful in determining the depth of the targets that can be imaged. This analysis will also be useful in selecting the best frequency range to be used in the inversion

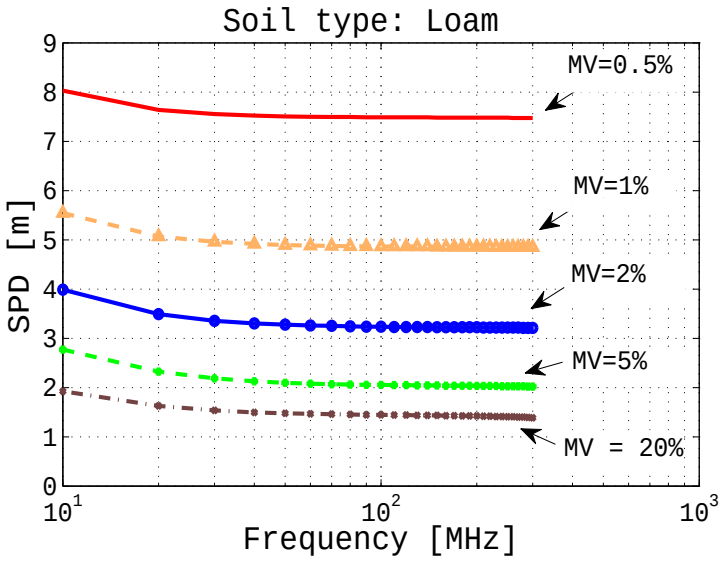

Figure 4.7: Signal penetration depth for varying moisture content plotted as a function of frequency, the soil type used here is loam.

depending on the depth of interest. Realistic subsurface regions of interest can be divided into two categories: 1) regions where the soil type is mostly the same and the soil dielectric varies mainly due to variation in soil moisture and, 2) those where the soil is highly inhomogeneous consisting of varying soil moisture and/or multiple soil textural compositions. The depth where the signal illuminating the air-ground interface decays by 10dB (chosen cutoff point) is calculated for the frequency of interest. We performed two sets of simulations to analyze these cases. In the first set, the subsurface region is modeled as a homogeneous half space. The soil textural composition (% of clay, silt and sand) was kept constant and soil moisture content is varied. In the second case, a multilayered medium is created by varying the moisture content of the different layers. As can be seen in Fig. 4.7 and Fig. 4.8, the cutoff point varies significantly based on soil textural compositions as well as soil moisture. But, the SPD is at least 1.5m in the upper VHF range even for higher moisture content.

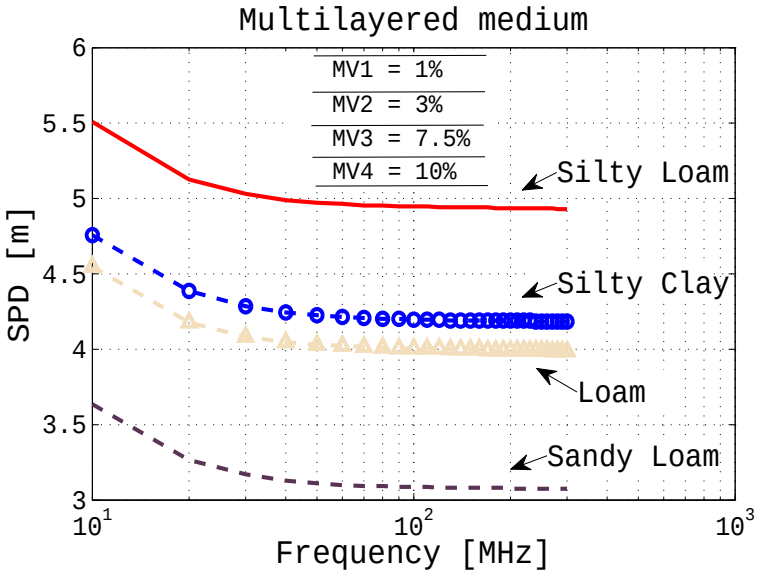

Figure 4.8: Signal penetration depth (-10 dB) is plotted as a function of frequency. A subsurface medium with four layers with equal thicknesses and different moisture (1,3,7.5,10 %, i.e. layers 1 to 4) are used for this simulation.

It can be seen that soil moisture is the more important factor in determining the signal penetration depth. For lower soil moisture contents (less than 3%), the signal penetration depth is much higher compared to higher moisture cases. It's important to note that in relatively drier areas, the SPD would be much higher. The cutoff point is chosen to be -10dB because the round trip attenuation of -20dB beyond the propagation path loss in relatively short distances is tolerable by sensitive receivers. If the sensitivity of the receivers can be increased, it will be possible to image targets that are located deeper than what is shown in the analysis above. We can see from the above analysis that by using VHF frequencies, it's possible to localize targets buried several meters below the surface depending on the soil texture and soil moisture.

4.3 Proposed imaging approach and analysis

A high resolution subsurface imaging technique based on distributed near-ground sensor networks is proposed. The antennas are to be mounted on autonomous rovers or flyers as depicted in Fig. 4.1. The proposed subsurface imaging algorithm uses an ultra-wideband signal and a large aperture with near-field focusing. As compared to existing technologies such as GPR, the advantage of rover based near-ground sensor networks is that it can provide high lateral and depth resolution, possible autonomous data collection capabilities, and is suited for efficient detection of distributed targets covering large areas(e.g. mine fields and UXO contaminated areas). Traditional GPR systems essentially acquire data in a uniform grid of receiving points, but not all of these receiving points provide independent information about the subsurface environment. Also, in traditional GPR approach the data points are not processed coherently together. In this work, we investigate possible ways of reducing the total number of receiving points required to achieve a certain resolution. Simulation and scale model measurement results will be utilized to assess various sensor distributions both in terms of spatial distribution and polarization keeping in mind the possible routes that the rovers could follow.

4.3.1 Inversion algorithm

Given a set of electric field measurements and the transceiver spatial distribution, the goal of the inversion algorithm is to localize targets submerged below the surface with the best possible resolution. This requires an estimation of the soil dielectric profile. An iterative approach is used to achieve this. First, a best guess for the soil

moisture profile using a stair-case approximation (assuming constant soil moisture content for each layer) is made. The starting value for the moisture profile could be from past history of the region of interest or simply a constant value if the history is not known. The semi-analytic soil dielectric model discussed in Section 4.2 is then used to estimate the complex dielectric constant profile based on the guessed moisture profile. Using this dielectric profile, Geometric Optics in conjunction with the back-projection algorithm is used to create an approximate 3D image of the subsurface domain. The algorithm used in this work is the frequency domain equivalent of the back projection algorithm. Essentially, the correct signal path between the Tx/Rx antennas and each test cell is calculated which in the inversion will be used to undo the time delay in each layer as given in equation (1). The inner sum over the various receiving points improves the lateral resolution by increasing the aperture while the outer sum which is over frequency increases the depth resolution. To actually improve upon the first-order 3D image, an optimization must be carried out to better estimate the soil moisture profile and the resolution of the image. The objective function for this optimization is defined as:

$$O(p_i) = \sum_{f_l}^{f_u} \sum_{r_n} S_{21}^{Cal}(f, r_n) \prod_{l_1}^{l_m} e^{jk_l(f, mv_l)[r_l^t(p_i) + r_l^r(p_i)]}, \tag{4.1}$$

where, p_i and S_{21}^{Cal} are the coordinates of the current test point and the calibrated received field (as a function of frequency and current receiver position), respectively. mv_l is the volumetric moisture value for layer l. Also, r_l^t and r_l^r are the distance traveled by the signal from the Tx antenna to the current test point and from the test point to the current receiving point, respectively. If there are buried targets,

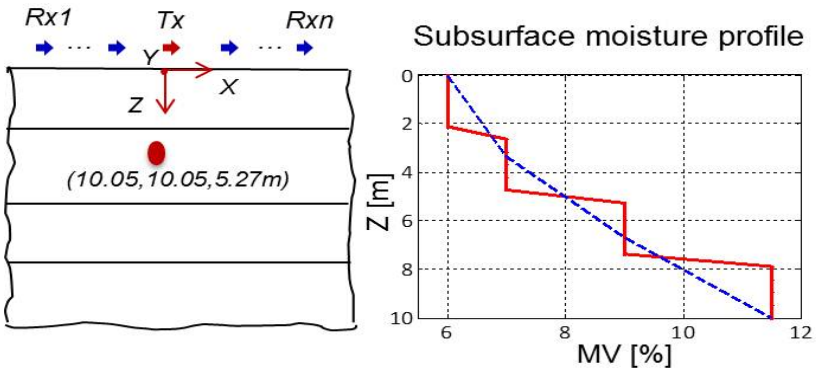

Figure 4.9: Simulation setup for analysis of lateral resolution, the lateral dimensions of the region of interest was 20m by 20m while the depth was 10m. The subsurface medium is composed of sandy loam with the moisture profile given above.

these targets are imaged with poor resolution initially. The image is sharpened by searching for the correct soil dielectric profile. This is done in two ways: 1) by maximizing the power from a pixel within a target region, and 2) by minimizing the difference between the sum of the values of a set of resolution boxes around the maximum of the point spread function (PSF) and that of the ideal PSF.

The lateral resolution is obtained by forming a synthetic aperture using coherent measurements acquired by multiple rovers moving in specified routes. As it was alluded to earlier, achieving very high resolution and being able to detect or image targets that are deeply-submerged are one of the main goals. With operation at the VHF range, better ground signal penetration and long range coverage can be achieved as described in the previous section. Higher bandwidth results in better depth resolution. Therefore, the antennas, with center frequency in the VHF range, should be able to operate over a wide frequency band. Issues related to the design of a compact and low-profile antenna in the proposed frequency range with good bandwidth is recognized as one of the main challenges of the implementation of a prototype of the proposed imaging system and will be addressed in section 4.3.3.

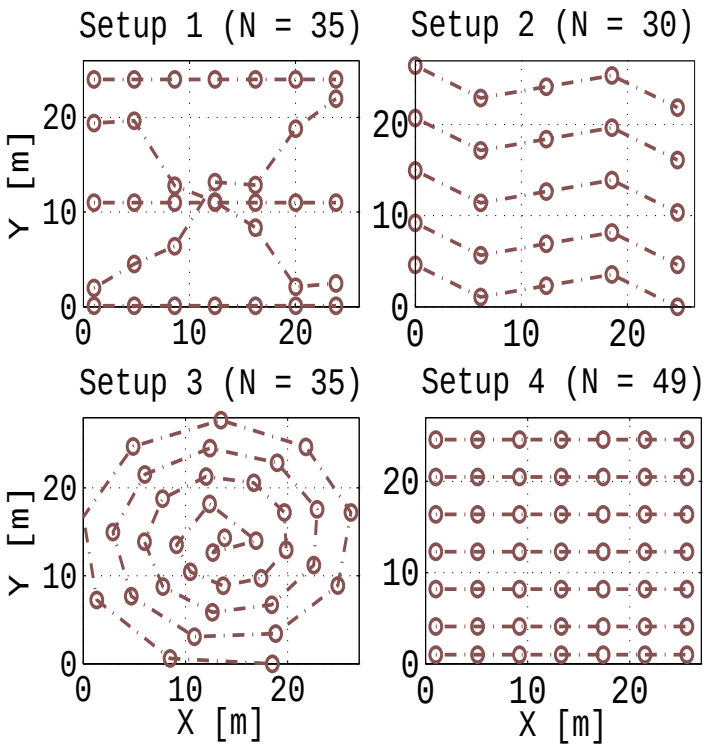

Figure 4.10: Several uniform and non-uniform sensor configurations are shown. The corresponding lateral resolutions are also compared.

4.3.2 Numerical validation and analysis

The proposed imaging approach was implemented and tested using data generated based on the forward model presented in Section 4.2. The raw data was created based on a four layer medium with a dielectric profile as given in Fig. 4.9. In this set of simulations, Geometrical optics was used to calculate the received fields. The lateral dimensions of the simulation domain was 8λ by 8λ and the depth was 4λ at 120 MHz. The Tx antenna is positioned in the middle of the setup just above the top surface. As can be seen in Fig. 4.10, various configurations of receiving points are tested. The setups are chosen to cover large area while creating the necessary synthetic aperture to improve the lateral resolution. Also, the number of measurement points should be minimized for efficient data collection and inversion. The lateral resolution is shown

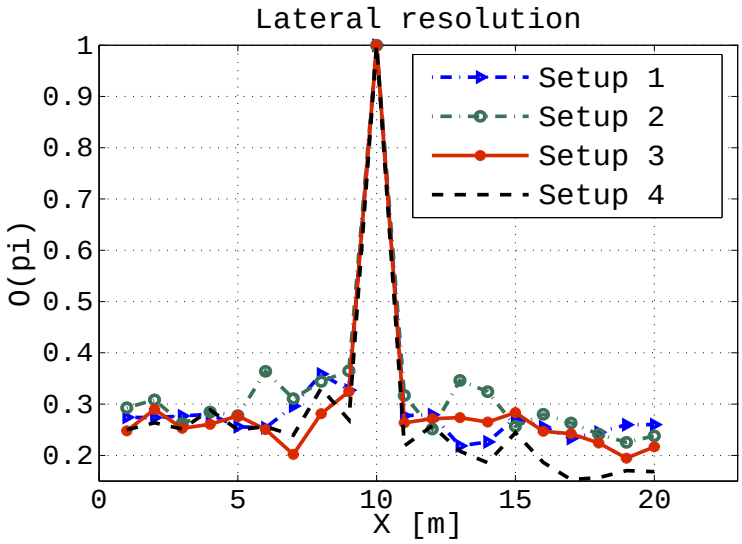

Figure 4.11: The Lateral resolution plotted for the simulation setup shown in Fig. 4.9. The various sensor setups used for this simulation is shown in Fig. 4.10. The frequency range for this simulation is from 30MHz to 270MHz with 5MHz steps.

in Fig. 4.11. The non-uniform setup (Setup 1) results in the same resolution with slightly higher side lobes as the uniform rectangular grid which has more number of receiving points. It should be noted that in a realistic subsurface environment receiving points that are further away from the Tx antenna do not improve the resolution because the received signals become very small due to subsurface loss (especially at higher frequencies). In the proposed approach, however, the signals travel longer range since we are using frequencies in the VHF band. This makes it possible to have larger synthetic aperture.

Another set of simulations were performed to assess the performance of the imaging algorithm based on raw data created using a full-wave solver. The simulation setup for this case includes a half-space dielectric medium and a small metallic sphere buried at a depth of 7m below the surface. Perfectly matched layer (PML) boundary conditions are utilized to simulate the infinite half-space. The full-wave simulation is important because it takes into account field components that are ignored by

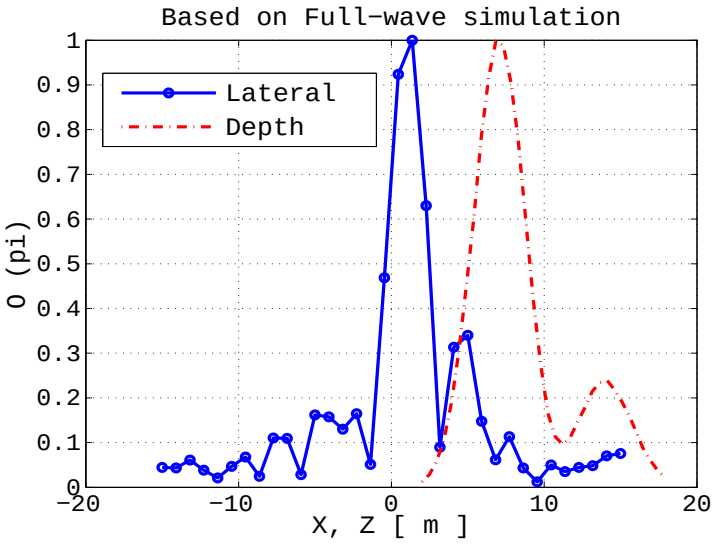

Figure 4.12: The Lateral and depth resolution retrieved based on raw data created using a Full-wave solver.

Geometrical Optics. These include near-ground wave propagation effects (Norton surface waves) and other higher order components. A horizontally polarized short dipole located just above the ground is used as a source and the received electric fields are recorded at several points around the Tx antenna as shown in Fig. 4.10. The frequency range used for this simulation is from 30MHz to 70MHz. For this simulation, the signal component that is scattered by the target is isolated by following the calibration approach discussed in Section . As can be seen in Fig. 4.12, the location of the target is correctly retrieved with good resolution. The depth resolution can be further improved if a larger bandwidth is used by including the higher VHF range which is not utilized for this particular simulation. Also, a larger aperture can improve the lateral resolution.

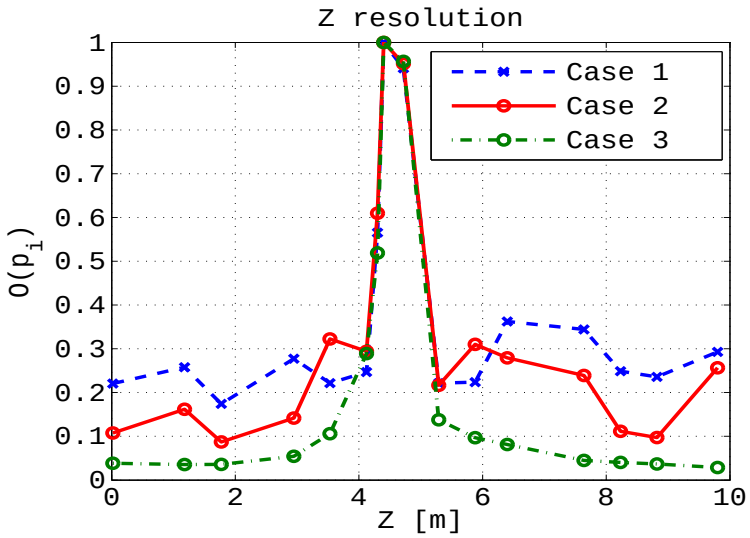

Figure 4.13: Comparison of depth resolution for the frequency selections listed in Table 4.1.

4.3.3 Frequency requirement analysis

The bandwidth of the system is the main variable that determines the depth resolution, however in order to realize the proposed imaging system, a compact low-profile ultra-wideband antenna in the VHF range is required. Designing such an antenna proves to be challenging due to various constraints. One way to mitigate this issue is to use an array of a few antennas operating at their first few harmonics which is equivalent to non-uniform sampling in the frequency domain. This will ease the design requirements of bandwidth of low-frequency (VHF) antennas. However, factors such as the number of frequency points and range as they relate to the depth resolution need to be investigated.

Simulations were performed to compare various sets of frequency points for a given bandwidth. The frequency range of interest is from 25 to 180MHz. Three different cases are investigated. In the first case, 15 frequency points were selected in such a way that they match three antennas with center frequencies at 25MHz,

30MHz and 35MHz. The first few harmonics along with the fundamental frequencies of each antenna are utilized. The second case is similar to the first case but with an additional antenna which has its fundamental frequency at 40MHz. The final case includes the whole 30-180 MHz range densely sampled in steps of 3MHz resulting in a total of 52 frequency points. It should also be noted that using a gaussian window whose fourier transform is also gaussian to the frequency domain data helps reduce side lobes in the resulting image (See Section 4.4). The various frequency choices are summarized in Table 4.1. Fig. 4.13 shows the depth resolution for the three different frequency sampling cases for a target located at 4.45m depth. The plots show that it is indeed possible to use fewer frequency points (Case 1 and 2) and still achieve almost the same resolution as in the densely sampled case (Case 3). Although, higher frequencies do not have high penetration depth, including higher frequencies (above 180MHz), could improve the depth resolution because some energy may still propagate (even for deeper targets) at those frequencies. This is especially true when the subsurface environment is not too moist. Also to compensate for the higher attenuation at higher frequencies, the waveform can be designed to transmit more power at higher frequencies.

Table 4.1: Various frequency selections

	Freq. [MHz]	No. of freq. pts.
Case 1	25,30,35,50,60,70,75,90,100,105,120, 125,140,150,175	15
Case 2	25,30,35,40,50,60,70,75,80,90,100,105, 120,125,140,150,175,180	18
Case 3	$25 - 180$	52

4.3.4 Sensitivity analysis

In this section, we investigate how the accuracy of the estimated dielectric profile of the background medium affects the accurate retrieval of the locations of the targets.

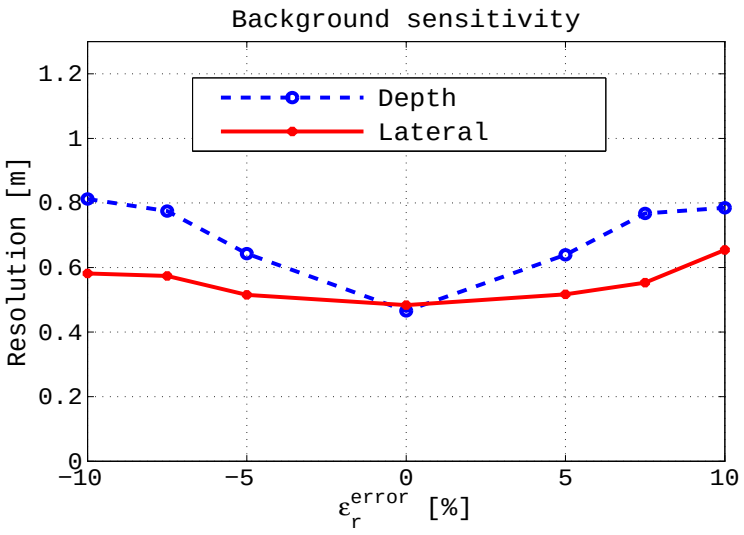

Figure 4.14: The lateral and depth resolution is plotted as a function of percent error in the estimated dielectric profile of the background medium.

This sensitivity analysis is important because it can be used to optimize the inversion. If, for example, 10% error in the background dielectric profile causes negligible change in resolution, then attempting to improve the accuracy of the profile is not necessary. It should be noted that in applications such as soil moisture retrieval, the accuracy of the dielectric profile is important. Here, we discuss the sensitivity analysis based on simulation results of a five layer setup (as in Fig. 4.9). We tested a case where there was only small losses in the subsurface medium and another more lossy scenario. The goal is to investigate how the background retrieval errors affect the resolution in different types of subsurface medium. The number of receiving points here is 144 and the frequency range from 30MHz to 270MHz is utilized. The lateral and depth resolution were calculated by introducing errors in the estimated dielectric profile compared to the profile used to create the raw data. As can be seen in Fig. 4.14 both the lateral and depth resolution change only by a small amount even when there is an error of up to 10% in the background dielectric profile.

Table 4.2: Proposed vs. Scale model parameters (The brick layer is used to create the profile)

	Proposed model	Scale model
Center freq.	100 MHz	10 GHz
Bandwidth	60 MHz	4 GHz
ϵ_r of Sand	2.8 + 0.018i	2.7 + 0.015i
ϵ_r of Brick	5.9 + 0.7i	5.9 + 0.7i

4.4 Laboratory scaled model measurement results

The proposed imaging approach was investigated by utilizing raw data created using MATLAB and a full-wave solver as discussed in the previous section. However it's important to validate the technique experimentally in the presence of practical limitations. Implementing the system at the frequency range of interest (VHF) is not pursued in this work because of limited space and resources. Instead we decided to perform a scaled model measurement with a scaling factor of 100. The main advantage of scale model measurements in the laboratory is that they are in controlled environment where all the parameters can be measured directly. Table 4.2 summarizes the various parameters used in the proposed and scale model. Since the Tx and Rx antennas are in close proximity to the ground, the relative orientation of the antennas have to be wisely chosen. For applications in communications, vertical polarization is preferred for near-ground scenarios [90],[106]. However, when the goal is to minimize the direct signal and direct most of the radiated field to the subsurface region, horizontally polarized Tx and Rx antennas are preferred. Various receiver configurations are tested by comparing the corresponding depth and lateral resolution.

In this experiment, a network analyzer based radar operating in the X-band is used. The geometry of the setup is given in Fig. 4.15. The measurement setup

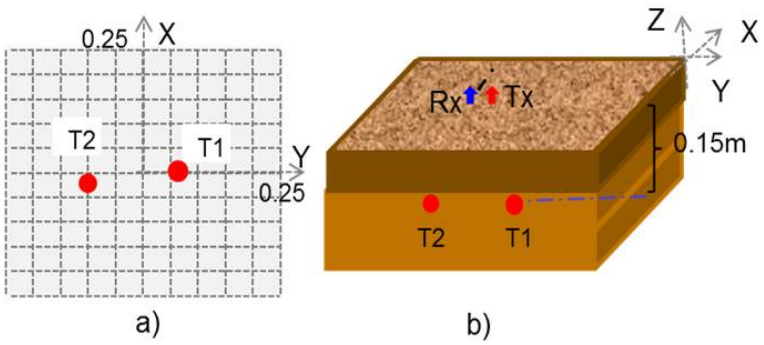

Figure 4.15: Measurement dimensions and target locations for the scale model experiment. The units of the given dimensions are in meters.

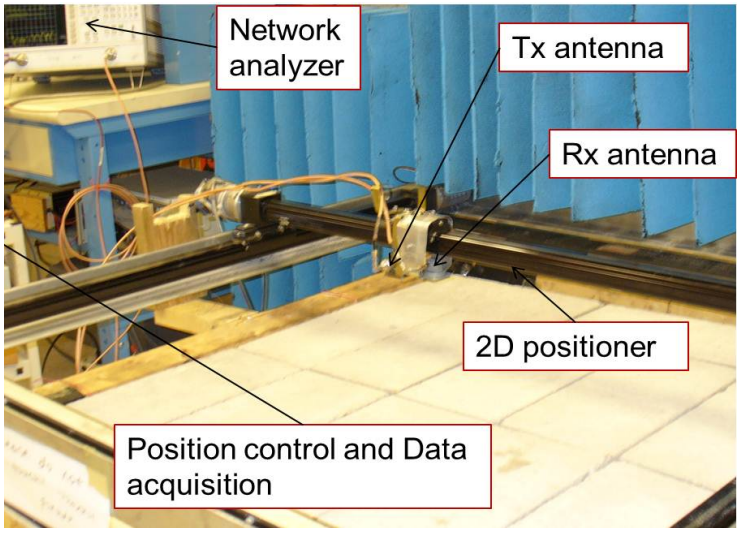

Figure 4.16: A picture of the laboratory scale model setup.

which is shown in Fig. 4.16 consists of a sandbox, a Tx and Rx antenna, 2D antenna positioner, metallic targets buried in the sand, a network analyzer and a PC. The size of the box is made large in terms of wavelength (40λ by 40λ by 20λ) at the center frequency of 10GHz. The large dimensions of the measurement setup will help minimize the effects of unwanted scatterers in the laboratory. It should be noted that two sets of antennas are tested in this experiment namely dual-polarized quadruple-ridged horn antennas and open ended waveguides. Open ended waveguides have advantage because they can illuminate larger region while the horns have a more directive pattern. It was found that the open ended waveguides are preferred for our purpose because with their wider beamwidth, a larger synthetic aperture could be formed.

One of the main goals of this experiment is to investigate the performance of the proposed technique for imaging targets that are deeply submerged in realistic subsurface environments. Two different cases of the subsurface environment are tested. In the first case, dry homogeneous sand is used as the background medium. Two small spheres are buried 15cm below the surface of the sand (See Fig. 4.15). In the second case, a layer of bricks is used as the top layer in addition to the sand layer. The brick layer is used to simulate a layer with higher dielectric constant. In reality, this happens because of the presence of soil type with higher dielectric or increased moisture. The scan area is 20λ by 20λ and a rectangular grid of data points with steps of $\lambda/2$ in each dimension is measured. At each data point, S_{21} is recorded by sweeping frequencies from 8GHz to 12 GHz with 401 frequency points. In order to minimize noise, averaging and narrow IF bandwidth is used in the Network analyzer settings. It should be noted that not all the data points can provide entirely

independent information. In fact one of the goals here is to use fewer points and still achieve almost the same lateral resolution.

The measured S21 data consists of the direct signal and the scattered field from the background and targets. Before applying the imaging algorithm, the component scattered by the targets will have to be isolated from other components. In addition, since both the Tx and Rx antennas are connected to the network analyzer via long cables, the delay caused by these cables needs to be removed. A calibration procedure, outlined below, is performed to isolate the field component scattered by the targets and to compensate for cable delays. Three sets of measurements are acquired. S_{21}^{Unal} is the measurement taken in the presence of the background medium and targets while S_{21}^{Bg} is measured in the presence of the background (but without the targets). In both cases the data is acquired at each receiving point by moving the antennas using the 2D positioner as can be seen in Fig. 4.16. Also, S_{21}^{C} is measured as a function of frequency by connecting the Tx and Rx cables directly. The frequency domain data consists of 401 points at each receiving point which is equivalent to applying a rectangular window to the frequency domain data. This has the same effect as multiplying the time domain data by a Sinc function resulting in higher side lobe levels. Using a gaussian window whose fourier transform is also gaussian results in better images because of reduced side lobe levels. The calibrated data (S_{21}^{Cal}) as a function of frequency for each receiving point is calculated by:

$$S_{21}^{Cal}(f, r_n) = W(f) * \frac{S_{21}^{Uncal}(f, r_n) - S_{21}^{Bg}(f, r_n)}{S_{21}^{C}(f, r_n)}, \tag{4.2}$$

where, W(f) is a windowing function which could be either a gaussian, hamming

or other windowing functions. In (4.2), subtracting the background measurement removes the direct and other scattered components while dividing by S_{21}^{C} compensates for the delay caused by the cables. Of course, in actual applications background data will not be available and another way of calibration has to be devised. One viable approach is to design antennas with minimal direct near-ground coupling. For near-ground antennas, the interactions between the Tx and Rx antennas occur at near-grazing incidence angles for which the Geometrical Optics components are not dominant. If the antennas are designed in such a way that the direct coupling is very small in the presence of the ground, there need not be a calibration step to remove the direct signal. In [106], various near-ground antenna pairs have been analyzed based on numerical techniques and the possibility of maximizing or minimizing (depending on the specific application) the received signal has been suggested. Another realistic alternative to remove the direct signal from the raw data is to use time-domain gating. This can be done because the direct signal always has the shortest path and hence can be removed in time-domain. After calibration, the data is processed by the inversion algorithm. As can be seen in Fig. 4.17, the image created based on measured data clearly shows the targets at the correct locations.

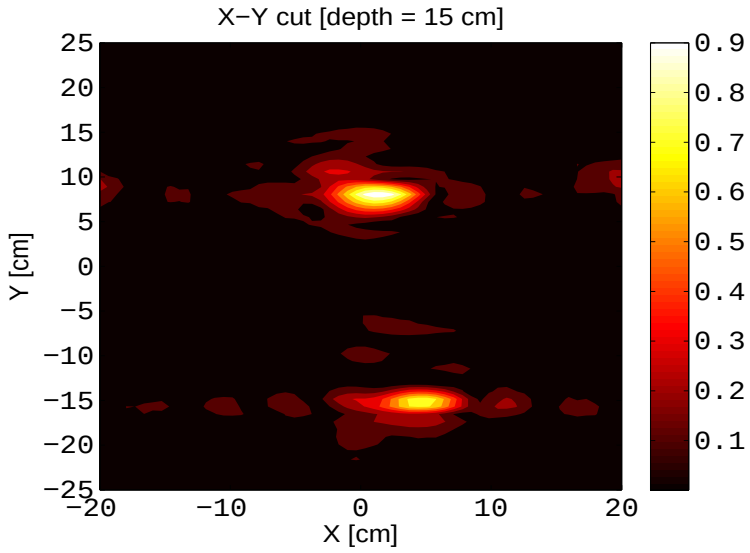

Figure 4.17: The X-Y cut of the reconstructed image of two small spheres located at a depth of 15cm.

CHAPTER V

Measurements and Physics-based Analysis of Co-located Antenna Pattern Diversity System

5.1 Introduction

A thorough and accurate analysis of a diversity system needs three main components: the Tx and Rx antenna radiation patterns (phase and amplitude), the multipath coherent propagation model and the calculation of a figure of merit for the performance of the diversity system such as complex and envelop correlation coefficients and/or diversity gain. Existing simulation based diversity analysis techniques essentially model the indoor or other multipath channel using a stochastic model such as Rayleigh and Rician distributions. While these probabilistic models provide generalized approximations to the indoor channel, such models do not accurately capture all the propagation mechanisms such as angle of arrival and polarization, and hence diversity analysis techniques based on such models inherently lack the information needed to assess the true performance of a given diversity system. For example, for near-ground antennas, propagation supported by Norton surface waves have to be captured for accurate field calculations. Specifically, for Tx and Rx antennas located less than a wavelength (λ) above ground, wave propagation is dominated by Norton surface waves. The other aspect of diversity system is the design of a common

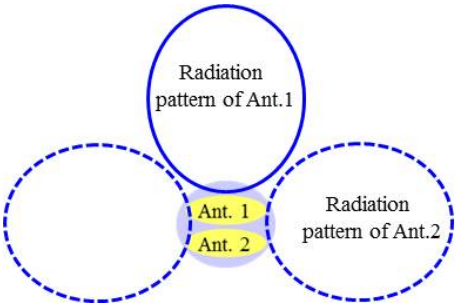

Figure 5.1: A schematic of a Radiation pattern diversities using two antennas.

aperture radiation pattern diversity antenna. Recently, different types of antenna topologies with radiation pattern diversity have been reported [107]-[108]. In such literature, one antenna has omnidirectional radiation pattern, and the other antenna has broadside radiation pattern, as depicted in Fig. 5.1. While the antenna geometries in the literature provide the desirable isolation between two antennas, they are based on multi-layer structures, that cannot be easily fabricated and are not easily amenable to miniaturization. This paper introduces a new approach to design an antenna with a small form factor and co-polarized radiation pattern diversity.

In this chapter, we discuss a new diversity system analysis approach that takes into account the complex radiation pattern of the Tx and Rx diversity antennas and make use of an accurate deterministic, coherent, and polarization preserving propagation model for a complex indoor scenario. One advantage of this approach is that for a diversity system deployed in complex scenarios the performance can be quantified accurately since all the propagation mechanisms are accounted for. In section 5.2, the new physics-based pattern diversity analysis approach will be introduced. The propagation modeling with specific focus on near-ground antennas will also be discussed. An accurate near-ground indoor propagation model that can accurately capture scattered field components from indoor obstacles while fully

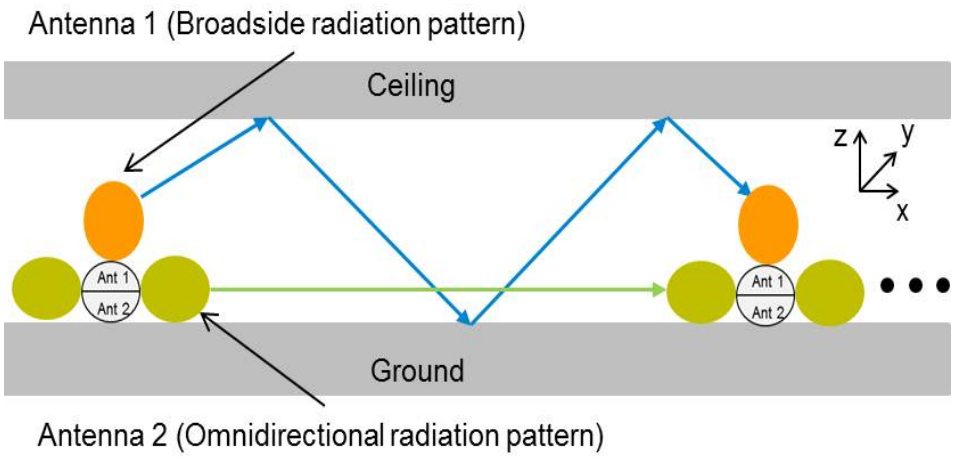

Figure 5.2: A schematic of a Radiation pattern diversity system in a hallway (top view) environment.

taking into account the Norton surface waves will be discussed as well. An example analysis of a near-ground diversity system based on this model will also be presented. In section 5.3, the design of a co-located radiation pattern diversity antenna will be described which is used in a pattern diversity measurement system. Finally, in section 5.4, the diversity measurement system to measure the amplitude and phase of the received field needed for computing the complex correlation coefficients will be presented.

5.2 Physics-based simulation and Analysis of Pattern Diversity Systems

As it was alluded to in the previous section, the objective of this section is to discuss a new approach to analyze the performance of a diversity system. This technique will be utilized to investigate the performance of the pattern diversity system based on a common aperture pattern diversity antenna described in section 5.3. Of the various diversity techniques mentioned in the previous section, for small platforms, spatial diversity is not possible. However, it is possible to use a small antenna with

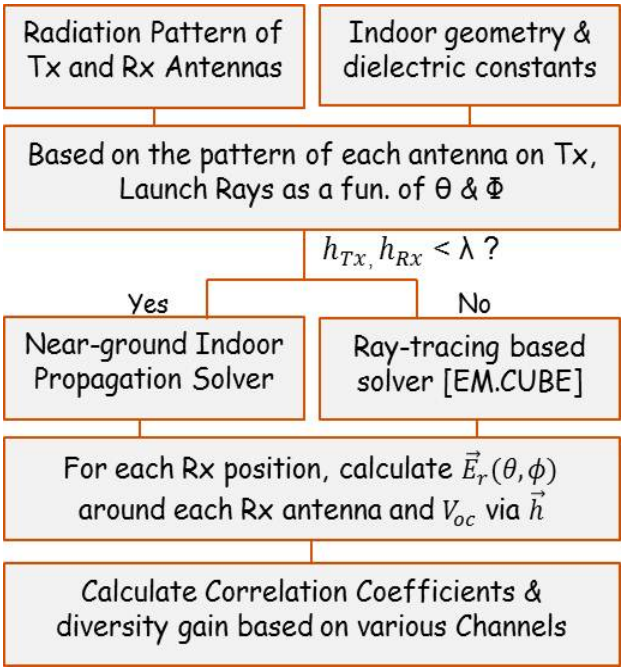

Figure 5.3: A diagram of the proposed physics-based diversity system analysis approach, $E_r(\theta,\phi)$,V_{oc} and $\vec{h}$ are received field, open circuit at the Rx channel and antenna effective height, respectively. h_{Tx} and h_{Rx} are the heights of the Tx and Rx antennas.

two or more feeds to generate different radiation patterns. The main idea of pattern diversity approach is to utilize antenna systems with different ports that radiate electromagnetic fields in mutually exclusive (almost) directions and when positioned in multipath environments can receive the fields in mutually exclusive directions. This results in simultaneous field measurements that are statistically uncorrelated and thus can be utilized to improve the wireless connectivity.

The block diagram in Fig. 5.3 shows the proposed diversity analysis technique. In this section, the steps for calculating the open circuit voltage (V_{oc}) at the Rx ports and the complex correlation coefficients between the various channels is described. We will then discuss two sets of results: 1) a near-ground scenario where the antennas are within a wavelength above ground, and 2) a case where the antenna heights are greater than a wavelength. At the frequency of operation used for this analysis

(400MHz), if the antenna heights are above λ (75cm), the ray-tracing approach is a good approximation. For the near-ground case, we will utilize an efficient propagation model that we developed for this application.

5.2.1 Calculation of Rx Open circuit voltage and Complex correlation coefficients

Here, we will discuss the steps required to calculate the complex correlation coefficients between the different channels (e.g. the horizontal and vertical pattern channels as illustrated in Fig. 5.2). First, the complex radiation pattern of the Tx antenna system for all directions, i.e. the complex normalized electric field values (in the far-field) sampled in small steps as a function of θ and ϕ, are imported. For each value of θ and ϕ, rays are launched by taking into account the complex pattern data in that direction. All the rays are then used as sources to illuminate the multipath propagation environment in which the antennas are operating. For each Tx-Rx arrangement, an accurate deterministic propagation model is used to calculate the electric field incident on each Rx antenna element as a function of θ and ϕ. The real and imaginary parts of the incident electric field in conjunction with the effective Rx antenna height is used to calculate the open circuit voltage at each Rx antenna port. The open circuit voltage(V_{oc}) is defined as

$$V_{oc} = \vec{h}(\theta, \phi) \; . \; \vec{E^i}(\theta, \phi), \tag{5.1}$$

where,$\vec{h}$ and $\vec{E^i}$ are the complex effective height of the antenna and the complex received electric field at the receive antenna element location in the absence of the antenna. The effective height h can be expressed in terms of a matched load Z_L, the

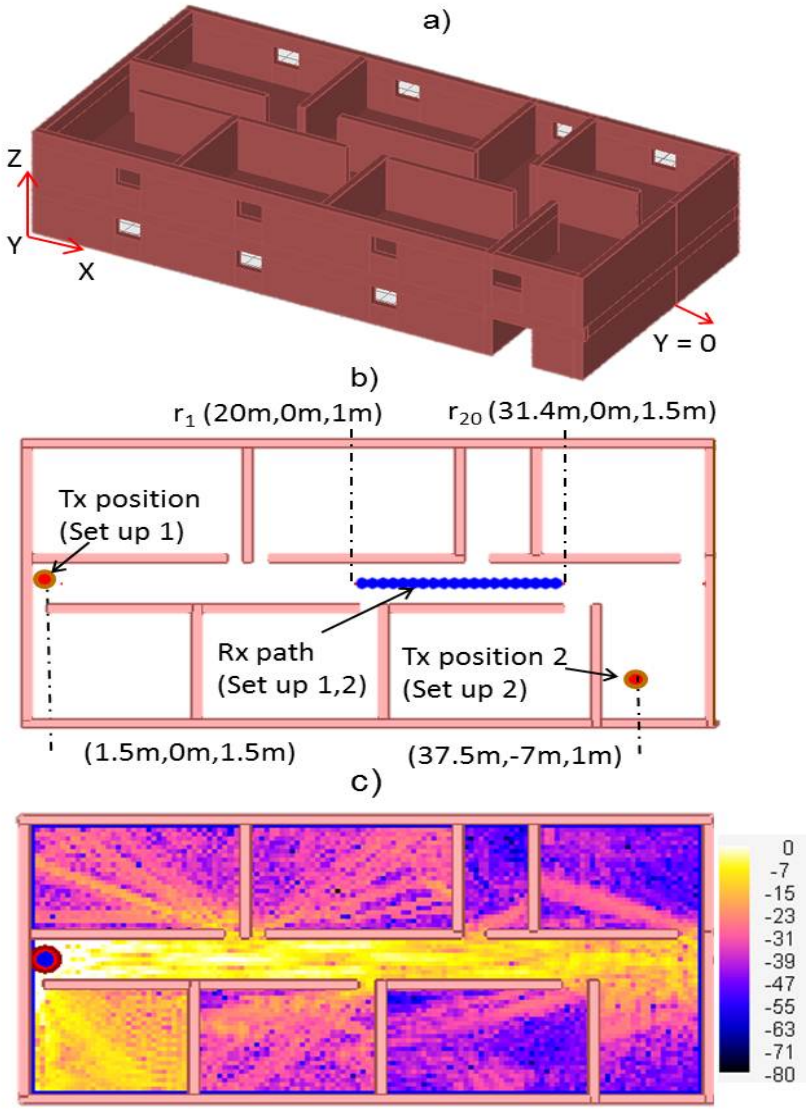

Figure 5.4: a) Simulation geometry (ceiling and ground not shown but are included in the simulation), b) the top view and the Tx-Rx configurations for diversity system simulation analysis, and c)signal coverage when Tx is at Position 1 on a plane parallel to the ground at 1m height.

complex pattern of the Rx antenna ($G(\theta, \phi)$), the complex polarization vector of the Rx antenna ($\vec{p}$), free space impedance (Z_o), and the wavelength (λ) as

$$\vec{h}(\theta, \phi) = \sqrt{\frac{Z_L \lambda^2 G(\theta, \phi)\Gamma}{Z_o \pi}} \vec{p^r} \ , \tag{5.2}$$

The polarization matching factor (Γ) and the intermediate variables (a,b,β and α) are given by

$$\frac{p^i_\theta}{p^i_\phi} = a \ e^{j\alpha} \ \ \& \ \ \frac{p^r_\theta}{p^r_\phi} = b \ e^{j\beta} \ , \tag{5.3}$$

$$\Gamma = \frac{1 + 2ab \ cos(\alpha + \beta) + a^2 b^2}{(1 + a^2)(1 + b^2)} \ , \tag{5.4}$$

where $p^i_{\theta,\phi}$ and $p^r_{\theta,\phi}$ are the components of the polarization vectors of the incident field and the receive antenna, respectively. We can then calculate V_{oc} by including the polarization mismatch factor as

$$V_{oc} = |E^i| \sqrt{\frac{Z_L \lambda^2 G(\theta, \phi)\Gamma}{Z_o \pi}} \ . \tag{5.5}$$

Finally, if v_1 and v_2 are the open circuit voltages at the two ports of the receive antennas, the complex correlation coefficient between the two channels can be computed using

$$r_c = \frac{< v_1 v_2^* > - < v_1 >< v_2^* >}{\sqrt{(< |v_1|^2 > - |< v_1 >|^2)(< |v_2|^2 > - |< v_2 >|^2)}}, \tag{5.6}$$

where, $< . >$ represents the expected value operator calculated using the spatial samples of v_1 and v_2.

Another parameter commonly used to quantify the effectiveness of a given diversity system is Diversity Gain which is essentially the increase of the combined signal compared to a single channel [109]. In this paper, the diversity gain is calculated by using a selection combining criteria with maximum apparent diversity gain of 10 and an outage rate of 1% [110]-[111]. Using the antenna radiation efficiency (e_r) and based on the above assumptions, the effective diversity gain (EDG) can be calculated by

$$EDG = e_r.10\sqrt{1 - |r_c|^2}. \tag{5.7}$$

5.2.2 Simulation result of the pattern diversity antenna in a complex indoor scenario

In this section the performance characteristics of the proposed co-located pattern diversity antenna system is studied through simulation of wave propagation in a complex multipath indoor environment. A two story office building shown in Fig. 5.4 is used for analyzing the performance of the proposed system. Two different propagation solvers are utilized. The first set of results presented in this section is based on a commercial ray-tracing based propagation solver called EM.CUBE [112].

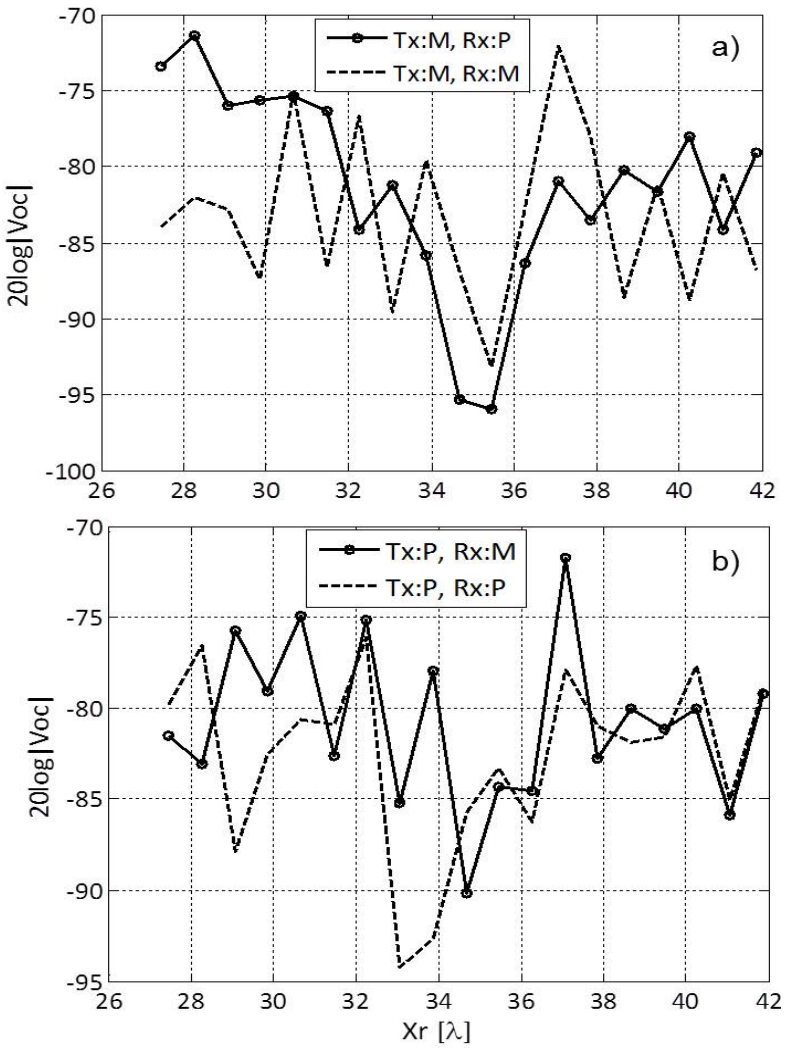

Figure 5.5: The computed open circuit voltage values at the outputs of a radiation diversity antenna composed of co-located patch and monopole antenna, a) when monopole antenna is transmitting, and b) when the patch antenna is transmitting.

In the next section a propagation model that we developed to analyze near-ground diversity systems is utilized. The building structure consists of several rooms where the walls are modeled as lossy dielectric slabs having a thickness of 50cm. The dielectric properties of the walls is assumed to be that of a brick wall ($\epsilon_r = 4.4$ and σ=0.004). The Tx and Rx pattern diversity antennas used for this simulation are co-located monopole and compact bowtie patch antennas. A detailed description is included in the next section. The complex building structure shown in Fig. 5.4*a* is modeled using EM.CUBE and for each radiating elements of the Tx pattern diversity antenna data are imported. For each new Rx position, the electric field corresponding to rays that are incident on the Rx antenna are calculated as a function of θ and ϕ. The incident electric field is exported and is used to compute the effective antenna heights of the Rx antenna elements for all angles of arrival.

Table 5.1: Correlation coefficients calculated for various channels based on simulation results for Set up 1 as shown in Fig. 5.4 (M and P stand for Monopole and Patch antennas, respectively)

Ch1 (Tx,Rx)	Ch2 (Tx,Rx)	r_c	$\lvert r_c \rvert$ [dB]
M,P	M,M	0.0434 + 0.0159i	-26.7
P,M	P,P	-0.1939 + 0.1399i	-12.43
M,M	P,P	-0.1857 - 0.1860i	-11.6

In the first case of the simulation of the diversity system, the Tx and Rx antennas are deployed along the corridor on the first floor of the building where the location of the Rx antenna is changed along Rx path as shown in Fig. 5.4*b*, and the transmitter is located at Tx position 1. This case is chosen to analyze the performance of the diversity system when there is a line of sight (LoS) between the Tx and Rx antennas. By following the procedure described above, the open circuit voltages at the Rx antenna elements are computed. As can be seen in Fig. 5.5, the V_{oc} curves show the uncorrelated variation of the various channels. In Fig. 5.5*a*, the monopole is used as the Tx antenna and the two curves show the channels created when the monopole

and patch antennas are used as a Rx antennas. For this scenario (LoS case), the vertical channel is mainly supported by the rays that bounce back and forth between the ground and the ceiling. The horizontal channel is mostly from multiple reflections from the side walls. A case where there is no line of sight between the Tx and Rx antennas as shown in Fig. 5.4*b* is also simulated (Tx position 2 and Rx path). In this case the received fields are mainly supported by the walls, ground and ceiling of the center hallway similar to the LoS case, but instead of the direct path, edge diffraction and penetration through walls also contribute to the NLoS case.

5.2.3 Near-ground propagation modeling and analysis

For near-ground transceivers deployed in multipath environments, electromagnetic wave propagation is dominated by Norton surface waves. In order to accurately calculate electric field coverage in complex propagation scenarios such as indoor environments, these higher order waves and their interactions with building walls and other indoor obstacles have to be captured. Full-wave solutions are computationally inefficient for indoor propagation simulations. The most commonly used field prediction techniques are based on ray tracing routines which are based on Geometrical Optics (GO). Ray tracing approaches are inadequate for evaluating signal coverage of transceiver nodes very close to the ground (less than a wavelength above ground) since such routines neglect higher order surface waves. For this reason we need to devise a technique that can efficiently capture the higher order surface waves and their interactions with the obstacles. Our approach for calculation of near-ground wave propagation and scattering is based on a physical optics solution where an asymptotic approximation of the Dyadic Green's function for a half-space dielectric

medium is utilized. In chapter 2, we presented a near-ground indoor propagation approach that fully takes into account the higher order Norton surface waves [90]. The field components scattered from indoor obstacles such as walls are computed using a physical optics approximation in conjunction with an efficient solution of the half-space Dyadic Green's function.

In this work, we extended this model to make it more efficient by taking into account the dominant scattering mechanisms when calculating scattering from indoor obstacles. The modified approach is implemented for hallway geometry similar to Fig. 5.2. Essentially, the geometry consists of the ground, ceiling and two side walls as shown in Fig. 5.2. When a radiation pattern diversity antenna (will be described in the next section) having two radiating elements as depicted in Fig. 5.1 is positioned in one end of this hallway very close to the ground , there will be a vertical and horizontal channel that are supported. The proposed propagation technique calculates the direct path between Tx and Rx, by radiating the current distribution on the Tx antenna using the Dyadic Green's function for a half-space medium discussed above. The first order reflections and multiple scattering from side walls are calculated based on the image method. In all the calculations, the surface waves are included. The open circuit voltage for each channel (when Rx antenna is Monopole or Patch) are calculated following the procedure described in the previous section. The resulting correlation coefficient is 0.0519.

5.3 Radiation Pattern Diversity Antenna Design

This section shows the design of a common aperture antenna in a small space having radiation patterns that are significantly different and almost orthogonal. This

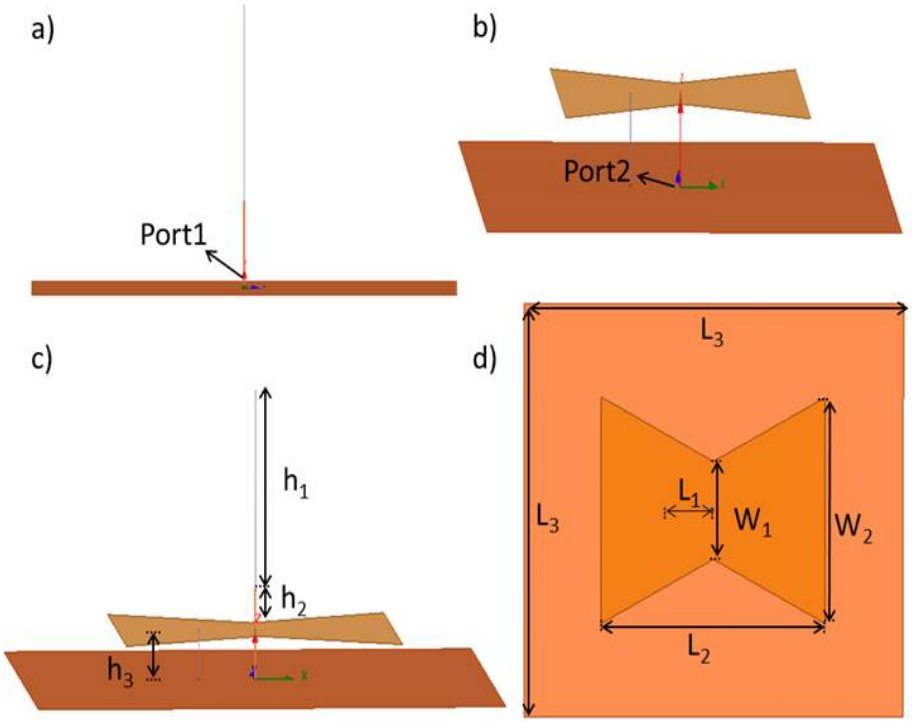

Figure 5.6: Geometry and design parameters of the proposed radiation pattern diversity antenna, (a) Monopole antenna, (b) bow-tie patch antenna,(c) proposed radiation pattern diversity antenna, and d) top-view of the proposed antenna.

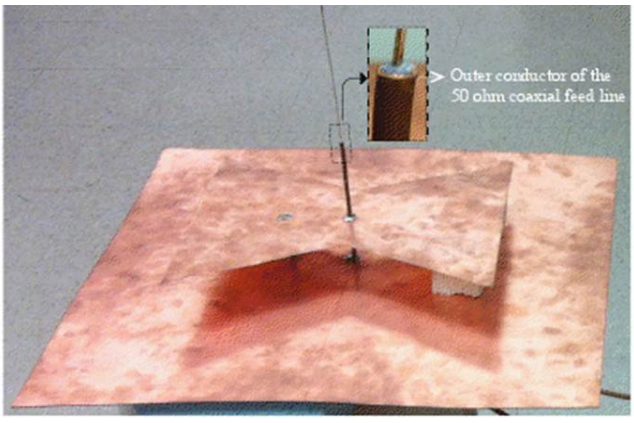

Figure 5.7: The proposed pattern diversity antenna designed and fabricated for the 400MHz diversity system.

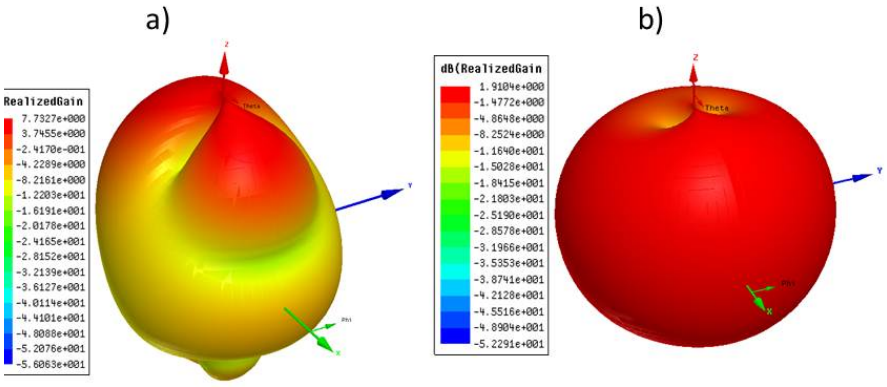

Figure 5.8: 3D radiation patterns (E_θ) of the proposed radiation pattern diversity antenna: (a) when the bowtie patch antenna is transmitting and the $\lambda/4$ monopole antenna is matched with 50Ω (broadside radiation pattern), and (b) when the bowtie patch antenna is matched with 50Ω and the $\lambda/4$ monopole antenna is transmitting (omnidirectional radiation pattern)

difference is measured by the envelop cross-correlation between the radiation patterns in the far-field. This can be done numerically if the theoretical radiation patterns ($\vec{F}(\theta,\phi)$) of both antennas are known in all directions based on:

$$\rho_e = \frac{|\iint [\vec{F_1}(\theta,\phi) \bullet \vec{F_2}(\theta,\phi)] d\Omega|^2}{\iint [\vec{F_1}(\theta,\phi)]^2 d\Omega \iint [\vec{F_2}(\theta,\phi)]^2 d\Omega}. \tag{5.8}$$

where $\bullet$ represents the Hermitian product.

Also, $\vec{F_1}(\theta,\phi)$ and $\vec{F_2}(\theta,\phi)$ radiation patterns antenna 1 and 2. In practice, it is difficult to know the radiation patterns for arbitrary antennas. To calculate the envelop correlation in this case, a relation between radiation patterns and scattering matrix (S-matrix) has been established [113] and is given by

$$\rho_e = \frac{|S_{11}^* S_{12} + S_{21}^* S_{22}|^2}{((1-(|S_{11}|^2+|S_{21}|^2))(1-(|S_{22}|^2+|S_{12}|^2))}, \tag{5.9}$$

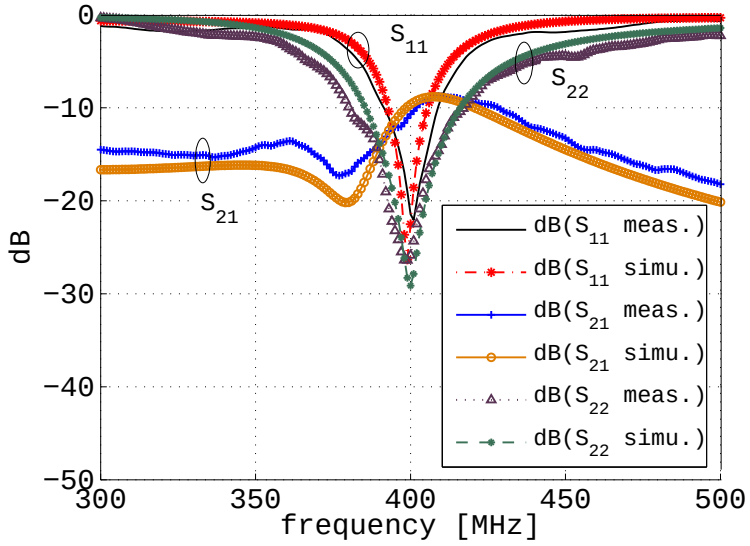

Figure 5.9: Measured and Simulated S-parameters of the proposed pattern diversity antenna

The proposed antenna system consists of two radiating elements: one with omnidirectional radiation pattern in horizontal plane and the other one with a radiation pattern mainly in the broadside direction as depicted in Fig. 5.1. Fig. 5.2 shows a simple geometry where the proposed antenna could be used to produce two channels with relatively small correlation. To realize the omnidirectional radiation pattern, a $\lambda/4$ monopole antenna is chosen. The second antenna, which needs to have a broadside radiation pattern, was chosen to be a bow-tie patch. In order to make the two antennas co-located in a small space, the monopole antenna is placed in the middle of the bow-tie patch antenna fed by a co-axial line with the outer connector of the co-axial line connected to the bow-tie patch. This enables high isolation between the two antenna feeds since electric potentials are zero in the middle of the bow-tie patch antenna and at the bottom of the monopole antenna.

The resulting envelope correlation between the two different radiation patterns from the proposed antenna system is quite small. In addition, considering the dif-

ficulty of impedance matching of the monopole antenna with stacked ground plane (bow-tie patch and its ground plane), the concept of the sleeve, which is a well-known technique for improving bandwidth and obtaining impedance matching, is applied [114]. In this geometry, a short section (h_2 in Fig. 5.6) of the coaxial cable protruding over the bow-tie patch antenna acts as an impedance transformer. Also, the bow-tie patch antenna is designed on the air substrate to obtain low dielectric loss. Since the geometry of the bow-tie patch antenna is symmetric in terms of XZ and YZ planes, omnidirectional radiation pattern of the $\lambda/4$ monopole antenna is preserved. Through a parametric study using a full-wave simulator, Ansoft HFSS 13.0, the two operating frequencies of the two antennas are designed to be same.

Design parameters are shown in Fig. 5.6. The values are given by L1 = 55 mm, L2 = 270 mm, L3 = 457 mm, W1= 108 mm, W2 = 250 mm, h1 = 159.5 mm, h2 = 31.5 mm, and h3 =40 mm. In order to consider ohmic loss, conductivity of copper is used in all metallic traces in the full-wave analysis. Fig. 5.8 shows the 3D radiation patterns of the proposed antenna at 400MHz. The radiation patterns are calculated by exciting one antenna while the other antenna is terminated with 50Ω and vice versa. Based on the simulated design parameters, the pattern diversity antenna is fabricated and measured, as shown in Fig. 5.7. As can be seen in Fig. 5.9, the measured S-parameters show good agreement with the simulated S-parameters. Phase and amplitude information of the S-parameters are used to calculate the envelop correlation (ρ_e) between the two different radiation patterns. The value of the calculated envelope correlation based on simulated results is shown to be as low as 0.00016 or -37.94 dB at 400MHz. Based on the the measured data, the value of the envelope correlation is found to be as low as 0.0013 or -28.97 dB at 400MHz. The

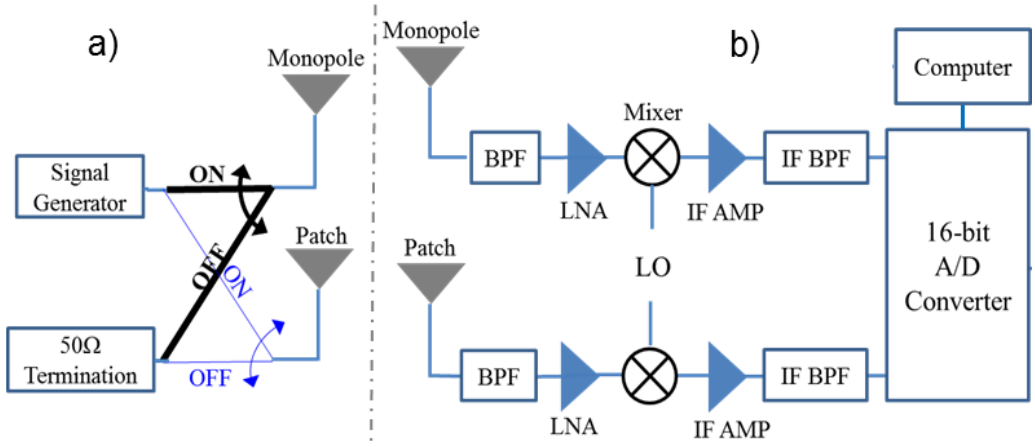

Figure 5.10: Schematics of (a) the transmitter and (b) receiver utilizing the proposed diversity antennas.

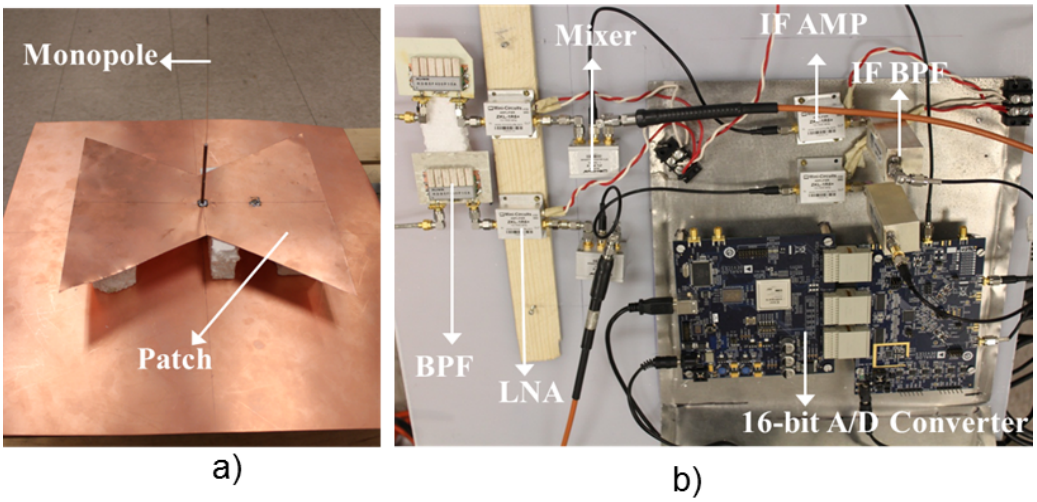

Figure 5.11: Pictures of (a) fabricated diversity antenna and (b) receiving module.

difference between simulated and measured envelope correlation values is due to the cable effects which can affect the radiation performances of the antennas, leading to the slight increase in the interaction between two feeds.

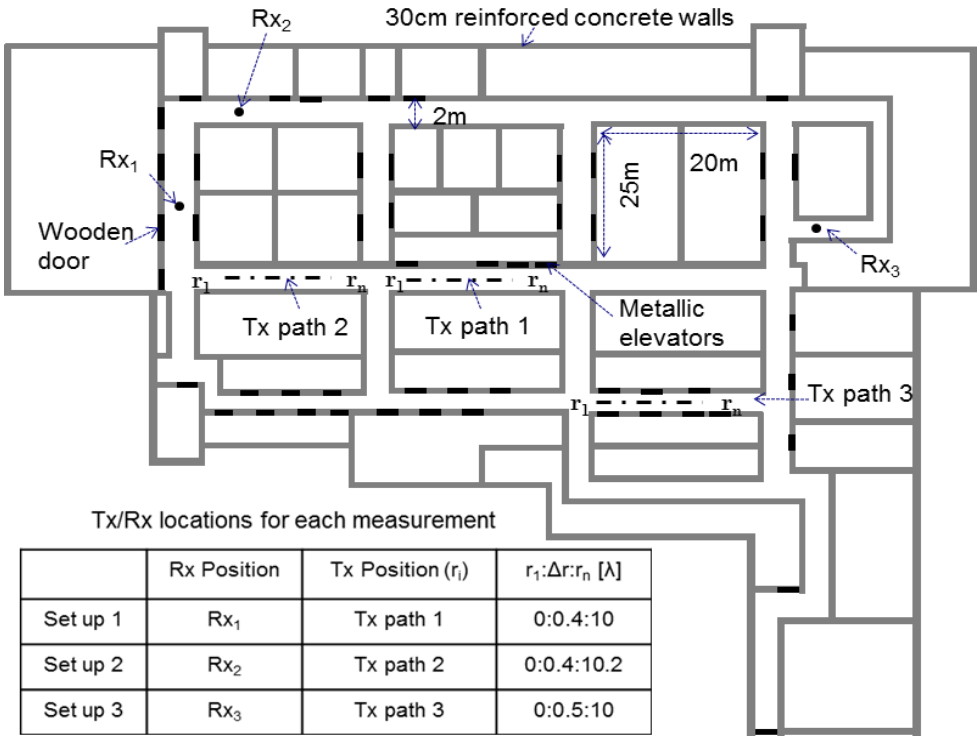

Tx/Rx locations for each measurement

	Rx Position	Tx Position (r_i)	r_1:Δr:r_n [λ]
Set up 1	Rx_1	Tx path 1	0:0.4:10
Set up 2	Rx_2	Tx path 2	0:0.4:10.2
Set up 3	Rx_3	Tx path 3	0:0.5:10

Figure 5.12: The floor plan of the Electrical Engineering building at the University of Michigan where the measurement was carried out. A table listing the Tx and Rx positions for each measurement is also included(r_1, r_n are the starting and ending points of each Tx path and Δr is the difference between consecutive Tx positions).

5.4 Radiation Pattern Diversity Measurement System and Results

5.4.1 System Configuration

In order to investigate indoor wave propagation of radiated fields from the proposed diversity antennas, a measurement system was designed and fabricated to operate at 400MHz. The operating frequency of 400MHz is chosen considering the allowable size of the antenna and characteristics of indoor wave propagation as a function of the operating frequency. Fig. 5.10 shows schematics of a transmitter and a receiver utilizing the proposed diversity antenna. When one Tx antenna is connected to a signal generator (ON), the other is terminated to 50Ω(OFF). Received signals at both receiving antennas are recorded. In other words, while only

one transmitting channel is 'ON', signals at both intended and unintended receiving channels are recorded. By calculating the correlation between the two signals received from two different antennas, the ability of the proposed diversity system to increase channel capacity is evaluated. In the receiver, the received 400MHz signals are down converted to 20MHz and the signals are sampled by a highly sensitive 16-bit A/D converter whose maximum available sampling rate is 80Mbps. With this receiver set up, the received data can be easily compared to each other and processed to calculate the correlation. Bandpass filters (BPF) are used to get rid of outer noise signals. Also low noise amplifiers (LNA) and IF amplifiers are used to satisfy the detectable sensitivity of the A/D Converters. Fig. 5.11 shows the photographs of the fabricated antennas and receiving module. In order to realize a channel established by near-ground wave propagation, the diversity antennas are positioned near the ground, about 10cm (0.13λ at 400MHz) above the ground.

5.4.2 Measurement in complex Indoor Scenarios

Using the measurement system discussed in the previous section, the propagation measurements are performed in a complex multipath-rich indoor environment. Fig. 5.12 shows the floor plan of the 3rd floor in Electrical Engineering building at the University of Michigan where the measurement was carried out. The measurement environment consists of several concrete walls and wooden/metallic objects including doors and ceilings. Three different sets of measurements were performed by varying Tx and Rx arrangements. These scenarios were selected in order to assess the performance of the diversity system for different levels of multipath. The positions of the Tx and Rx antennas are given in Fig. 5.12. In each case the position of the receiver

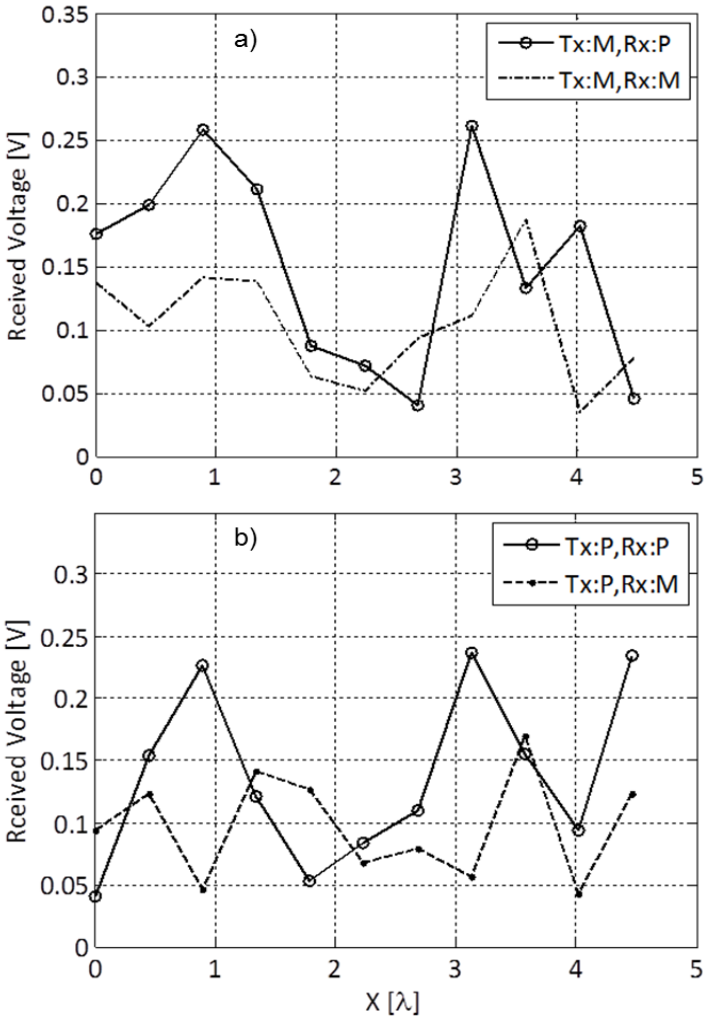

Figure 5.13: Measured signals for set up 1 (Fig. 5.10), a) when monopole antenna is transmitting while the Patch component of the Tx antenna is terminated with 50Ω and b) when the patch antenna is transmitting while the Monopole component of the Tx antenna is terminated with 50Ω.

system is fixed and the Tx antenna is moved along the path shown. The magnitude and the phase of the received signal corresponding to each channel is then recorded as a function of the position of the Tx antenna. For each measurement scenario, the received signals which can be considered as complex random variables in terms of the position of the transmitter. For example, v_{MP} is the signal measured when the Tx antenna is the monopole antenna while the Rx is the patch antenna. Finally, the complex correlation coefficient is calculated using (5.6) similar to the simulation results presented in the previous section.

The magnitudes of the signals for the first measurement scenario are given in Fig. 5.13. The output signals from the two Rx antennas (monopole and patch) when the Monopole antenna is transmitting while the Patch antenna is matched to a 50Ω termination are shown in Fig. 5.13*a* (Case 1). The signals from the other two channels (where Tx is Patch, Case 2) are shown in Fig. 5.13*b*. It is observed that in Case 1 where near-ground wave propagation is excited by the monopole antenna with omnidirectional radiation pattern, the fields radiated by the monopole antenna are well received at both receiving antennas. This is because the use of a finite ground plane makes the radiation pattern of the patch antenna broader, eliminating a desired radiation null at $\theta = 90°$. On the other hand, in Case 2 (where the Tx antenna is the patch) where propagation is mainly supported by rays bouncing between top ceiling and ground are dominantly excited by the patch antenna. The monopole antenna with a null radiation in the broadside direction has a relatively poor signal reception compared to the patch antenna. This is why the correlation coefficient in Case 2 is much lower than the correlation coefficient in Case 1. The envelop correlation coefficients between the channels for both cases were 0.3985 and 0.0953 for Case 1

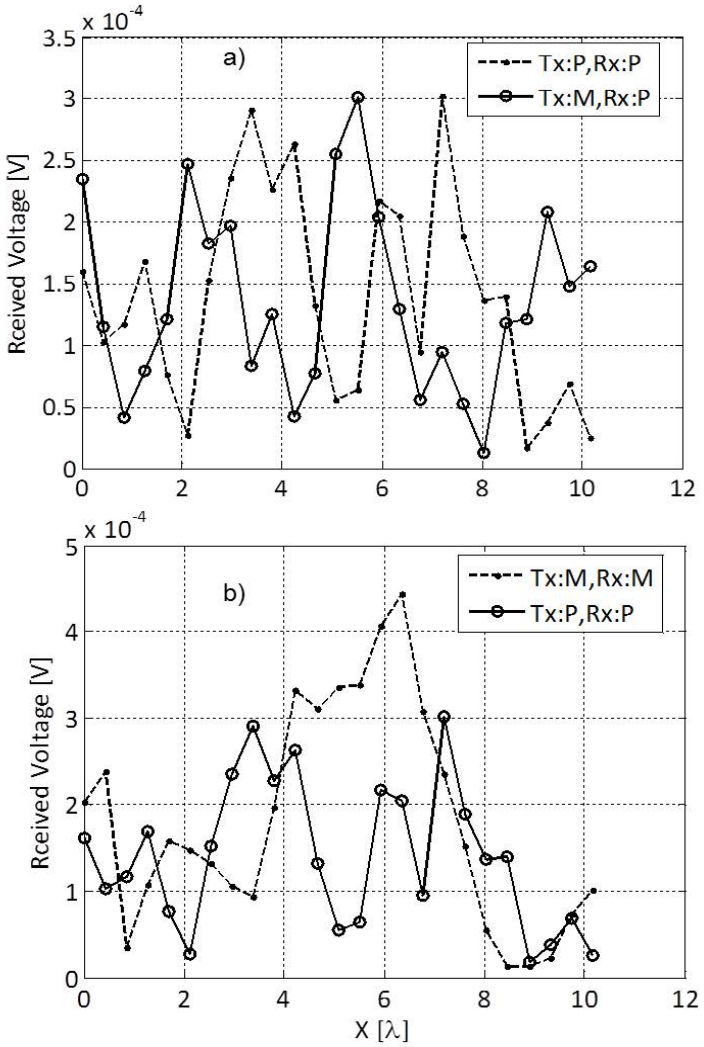

Figure 5.14: Measured signals for set up 2 (Fig. 5.10), a) received signals from the Patch antenna while the patch is transmitting (while the monopole is terminated with 50Ω) and when the monopole is transmitting (while the patch is terminated with 50Ω), b) received signal from the Monopole when the Monopole is transmitting and received signal from Patch when the patch is transmitting.

and Case 2, respectively. In both cases, the correlation values are less than 0.5, which meets the required industry standards. This measurement results, in addition to the simulation analysis presented, further validate the feasibility of using the proposed radiation pattern diversity system in multipath-rich indoor environments.

Table 5.2: Correlation coefficients calculated for various channels based on measured results (Fig. 5.9)

	Ch1 (Tx,Rx)	Ch2 (Tx,Rx)	Set up 1	Set up 2	Set up 3
Case 1	P,M	P,P	0.0953	0.3571	0.1656
Case 2	M,M	P,P	0.2757	0.0500	0.1857
Case 3	M,M	P,M	0.3985	0.0185	0.2553

The results of the second and third set of measurements, which correspond to set up 2 and 3 (Fig. 5.12) are given in Fig. 5.14 and 5.15. In all cases, the signals plotted as a function of position demonstrate independently varying magnitudes. These results show the advantage of utilizing the proposed radiation diversity system to create multiple channels with minimal correlation that could be combined to improve channel reliability in multipath environments. The correlation values computed for the various pairs of channels in all three scenarios are summarized in Table 5.2. Based on the three set of measurements, the two channels with lowest correlation are: 1)when both Tx and Rx are monopole (M,M), and 2)when both Tx and Rx are patch (P,P). This is because the first channel is mostly supported by near-ground propagation and multiple scattering between sidewalls, while the second channel is mostly supported by rays that bounce between the ground and ceiling. It should be noted that the correlation between other pairs of channels is also low (the maximum correlation value based on these measurements is 0.3985 and is as low as 0.05 for some cases). The effective diversity gain was also calculated based the measured results using a selection combining criteria for a 1% outage rate as described in section 5.2. The effective diversity gain for these measurements range from 7.75dB to 9.75dB for

the cases listed in Table 5.2.

Another way that is often used to demonstrate the performance of diversity systems is based on cumulative distribution functions which are used to describe the output SNR for a given outage rate. In order to analyze the improvement in signal-to-noise ratio as a function outage rate, a selection combining technique is utilized as described in [111]. Based on selection combining, the probability that the instantaneous combiner output SNR γ is below some value x can be calculated (by considering the correlation coefficient between the two channels) as

(5.10)

$$Prob(\gamma < x) = 1 - 2e^{\frac{-x}{\Gamma}} Q\left(\sqrt{\frac{2x}{\Gamma(1-|\rho_c|^2)}}, |\rho_c|\sqrt{\frac{2x}{\Gamma(1-|\rho_c|^2)}}\right) + e^{\frac{-2x}{\Gamma(1-|\rho_c|^2)}} I_o\left[\frac{2|\rho_c|x}{\Gamma(1-|\rho_c|^2)}\right],$$

where Γ is the mean SNR (assuming it is the same for both diversity branches) and ρ_c is the correlation coefficient between the two channels. Also, the functions Q and I_o are given in [111]. Based on 5.10, the output SNR is plotted against the outage rate in Fig. 5.16. The single channel case and the ideal two element case (when the correlation is zero) are also plotted. It should be noted that the curves in Fig. 5.16 are plotted in such a way that the output SNR value corresponding to 50% outage rate for the single channel case is 0dB. The other two curves shown in Fig. 5.16 are based on measured results using the pattern diversity system described in this chapter. As can be seen, the proposed pattern diversity system results is a diversity gain of 8dB at 1% outage as alluded to earlier.

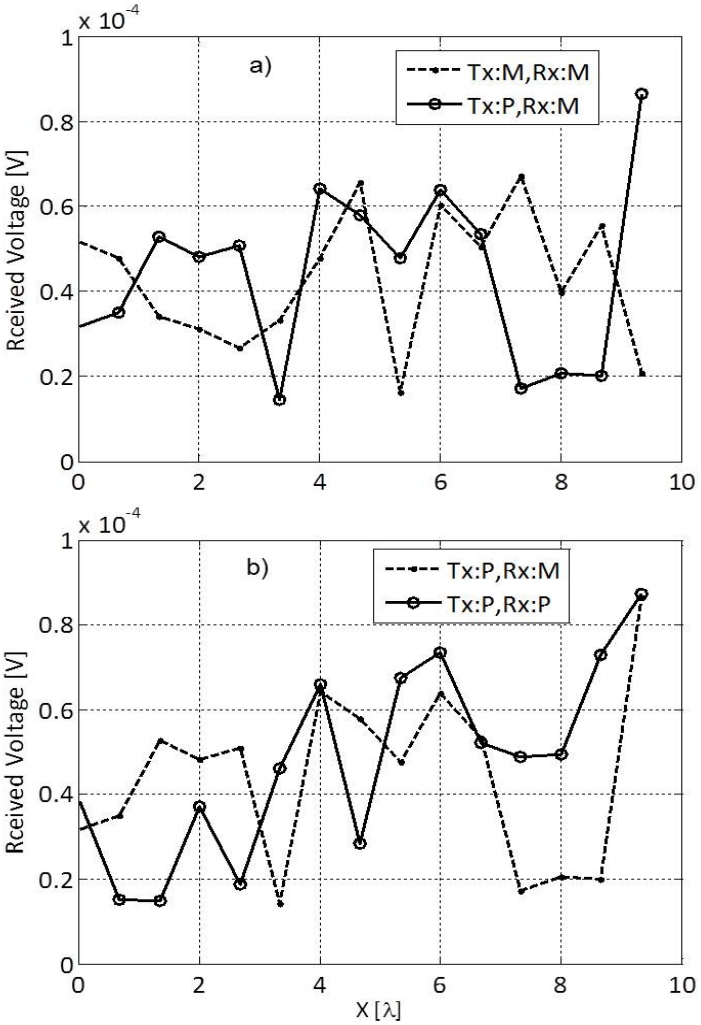

Figure 5.15: Measured signals for set up 3 (Fig. 5.10), a) received signals from the monopole antenna while the monopole is transmitting (the Tx patch is terminated with 50Ω) and when the patch is transmitting (the Tx monopole is terminated with 50Ω), b) when the patch antenna is transmitting while the monopole component of the Tx antenna is terminated with 50Ω and the Rx antenna is receiving in both channels

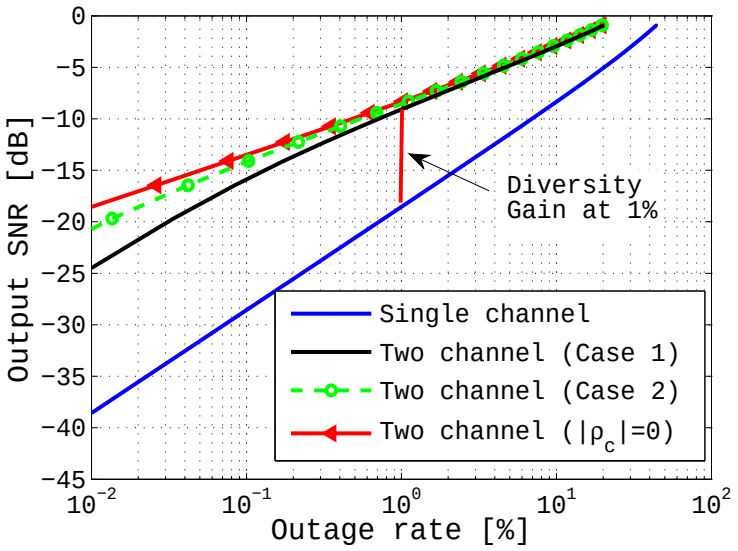

Figure 5.16: The output signal-to-noise ratio plotted as a function of the outage rate for a single channel and a two element diversity (i.e ideal case, the pattern diversity system discussed in this chapter. The two channels considered in Case 1 are (P,M) and (P,P). In Case 2, (M,M) and (P,P) are considered. In both cases, the channels are combined based on selection combining. Also, Case 1 and 2 shown above use the measurements results for setup 1 and setup 2, respectively (See Fig. 5.12).

CHAPTER VI

Conclusions and Future Work

Despite the significant progress and ongoing research, systems that utilize electromagnetic waves for detection and tracking as well as for communication in highly cluttered environments still have significant challenges. These challenges include developing accurate and efficient propagation and scattering models and designing compact sensor systems. In this thesis, new physics-based propagation and scattering models and existing numerical solvers are utilized to analyze the detection and tracking approaches proposed in Chapters II and III. A compact subwavelength source tracking and a subsurface imaging approach based on distributed sensor networks are described in chapter III and chapter IV, respectively. In chapter V, a new physics-based analysis technique for diversity systems is introduced and a co-located radiation pattern diversity antenna system prototype is realized and investigated via measurement and simulation. In the rest of this Section, a brief summary of the work described in this thesis and possible future research directions are discussed.

6.1 Summary

In this dissertation, RF based techniques for detection and tracking of obscured objects as well as for communication applications in multipath environments are proposed.

In Chapter II, an efficient semi-analytic model for near-ground wave propagation in indoor scenarios is presented. This is required because the applications of interest in Chapters II and III utilize sensors that are close to the ground in terms of wavelength by virtue of the fact that these systems utilize relatively low frequencies (HF and VHF band). Existing ray tracing routines which are commonly used for indoor field prediction, are inadequate for evaluating signal coverage of transceiver nodes very close to the ground (less than a wavelength above ground) since such routines neglect higher order surface waves. In addition, geometrical optics alone is inadequate to treat finite-size and possible irregular-shaped obstacles at low radio frequencies (VHF and lower UHF). Our approach for calculation of near-ground wave propagation and scattering is based on a hybrid physical optics and asymptotic expansion of dyadic Green's function for a half-space dielectric medium. Equivalence principle in conjunction with physical optics approximation is utilized to handle scattered field from building walls which are the dominant scatterers in indoor settings. Simulation results for various indoor propagation scenarios based on the new approach is validated by using both measurement results and full-wave numerical solvers.

In Chapter III, a Sub-wavelength source tracking system utilizing highly miniaturized antennas in the HF range for applications in GPS-denied environments including indoor and urban scenarios is proposed. A technique that combines a high resolu-

tion direction finding and radio triangulation utilizing a compact transmit (Tx) and receive (Rx) antenna system is pursued. Numerical models are used to investigate wave propagation and scattering in complex indoor scenarios as a function of frequency. We choose HF band to minimize attenuation through walls and multipath in indoor environments. In order to achieve a compact system, a low-profile and highly miniaturized antenna ($\lambda/300$ height and $\lambda/100$ lateral dimensions at 20MHz) having omnidirectional, vertically polarized field is designed. At such low frequencies, accurate measurement of the phase difference between the signals at the Rx antennas having very small baseline is challenging. To address this issue, a biomimetic circuit that mimics the hearing mechanism of a fly (Ormia Ochracea) is utilized. With this circuit, very small phase differences are amplified to measurable values. The numerical simulations are used to analyze direction of arrival retrieval and source localization in highly cluttered environments. A compact system prototype is also realized and source tracking in complex indoor scenarios is successfully demonstrated.

A high resolution subsurface imaging technique based on distributed near-ground sensor networks that utilizes ultra-wideband waveforms in the Very High Frequency (VHF) range is presented in Chapter IV. An accurate scattering model for a target buried in realistic subsurface environment, modeled as a vertically stratified medium, is presented first. Then an inversion technique that uses ultra-wideband near-field focusing is described. The signal penetration depth as a function of frequency and various subsurface parameters is calculated based on the developed forward model. The imaging resolution as it relates to the accuracy of background retrieval is also analyzed. A semi-empirical soil dielectric model that was originally developed for the Ultra High Frequency (UHF) band is modified and validated at the VHF range with

measured results available in the literature. For a given soil textural composition and frequency, the model predicts the real and imaginary parts of the dielectric constant as a function of soil moisture content (MV). This soil dielectric model is utilized to make the inversion more efficient. To address the challenge associated with the design of compact and ultra-wideband VHF antennas, a scheme utilizing multiple antennas and reduced number of frequency points is proposed. The sensor arrangement both in terms of spatial distribution and polarization of each antenna as it relates to the lateral resolution as well as minimizing the direct coupling between the Tx and Rx antennas is analyzed. The proposed subsurface imaging approach is validated based on numerical techniques and a laboratory scale model measurement results.

In Chapter V, an investigation of the advantages of radiation pattern diversity by using a new physics-based diversity analysis technique and measurement results is discussed. Unlike techniques that utilize polarization and/or spatial diversity, radiation pattern diversity offers a unique opportunity to achieve compact diversity antenna systems especially with the advent of enabling antenna miniaturization techniques. In this work, a novel co-located antenna radiation pattern diversity system is proposed and its performance is analyzed using an accurate physics-based diversity analysis technique. The proposed analysis technique utilizes an efficient deterministic propagation model along with the complex gain of the transmit(Tx) and receive(Rx) antenna systems. The proposed system is realized and tested in complex indoor scenarios based on which complex correlation coefficients between various channels is computed which are then utilized as a figure of merit for improved channel reliability.

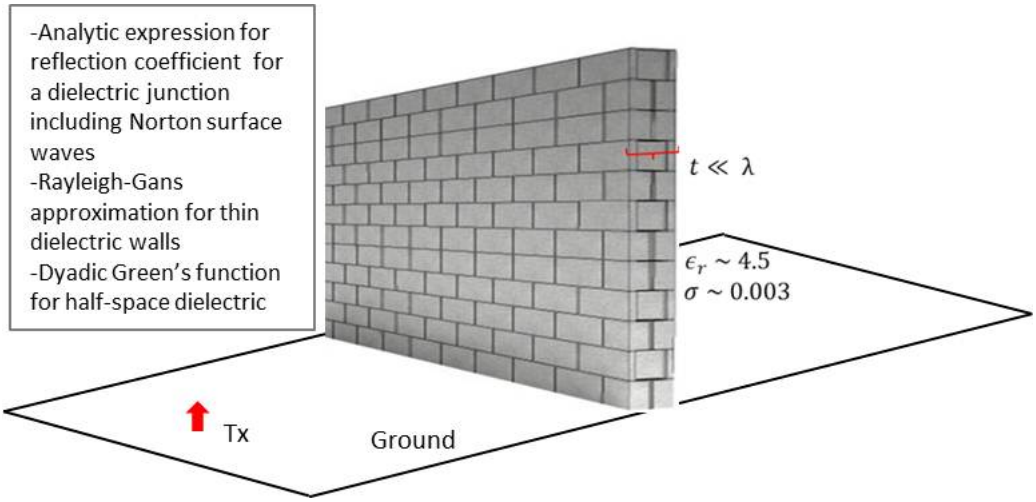

Figure 6.1: A concrete wall made of dielectric blocks. In many buildings metals are used for support. In the HF/VHF frequency range, the thickness of such walls is very small compared to a wavelength.

6.2 Recommendations for Future Studies

6.2.1 Near-ground wave propagation Modeling for Hybrid Outdoor-to-Indoor links

The near-ground propagation model for indoor scenarios presented in Chapter II addressed the challenge associated with near-ground propagation effects that commonly used techniques (i.e GO based approaches) do not account for. Although, the proposed approach proves to be significantly better than existing techniques such ray tracing, there are a few ways to further improve the model in terms of the complexity and size of the propagation scenario as well as computational efficiency. As an example, for a dielectric wall on top of a dielectric ground, instead of using the half-space Dyadic Green's function and resorting to a physical optics type approach, it would be more efficient if the effect of a dielectric wall can be captured using a modified reflection coefficient that takes into account the Norton surface waves.

Also, for low frequency applications, since indoor obstacles such as walls have

thicknesses that are only a small fraction of the wavelength, the calculation of scattered field from such scatterers can be made more efficient. Such a technique is specifically suited to accurately and efficiently analyze HF/VHF propagation in complex and electrically large indoor/urban scenarios. The asymptotic Dyadic Green's function for a half space dielectric medium can be used in conjunction with Rayleigh-Gans approximations to efficiently calculate scattered field from building walls while capturing the surface waves and their interaction with indoor obstacles. Another aspect of the work presented in Chapter II that needs further investigation is related to the fact that the ground in the current model is assumed to be flat. A more accurate and realistic model is to include surface roughness. In this regard, an efficient way to take into account roughness in addition to Norton surface waves for a flat ground is an area that needs to be explored.

6.2.2 Forward scattering model of Distributed Near-ground Sensors above a multilayered subsurface environment with rough interfaces

As discussed in Chapter IV, an accurate and efficient scattering model for a realistic subsurface environment is required in order to understand various scattering mechanisms, to perform sensitivity analysis and to assess the performance of an inversion algorithm. The Forward scattering model presented provides an efficient approach to calculate scattering point targets buried under a vertically stratified medium which can approximate a given dielectric profile. The proposed model provides a good solution especially for point targets that are far from air-ground interface. However, the proposed model should be improved in order to accurately handle metallic and dielectric targets buried under a multilayered subsurface scenario with rough interfaces. In order to accurately model extended targets the electric field

on the surface of the target can be calculated using the Dyadic Greens function for multilayered medium and either volume or surface equivalence principle can be used to calculate the currents and hence the scattered field from the buried target. The advantage of using the Dyadic Green's function is that it gives more accurate result compared to Geometrical Optics based approaches especially for targets close to the air-ground interface.

6.2.3 Optimally Distributed Near-ground Sensor Networks for Subsurface Sensing Applications

In the work presented in Chapter IV, the selection of spatial distribution of measurement points was investigate based on simulation and measurement results. The results presented showed that it is possible to achieve similar azimuth resolution with less number of measurement points compared to uniform grid of measurement points. Utilizing a more rigorous approach to determine an optimal distribution of measurement points using optimization techniques such as Genetic algorithm would be an ideal next step to the analysis presented. It should be noted that the solution will obviously depend on the specific subsurface environment (dielectric profile, number of layers, thicknesses of each layer and dielectric contrast between target and background medium. However, one can focus on arriving at specific solutions that are application dependent. In the same chapter, a frequency selection scheme that is meant to address the challenges associated with the design of compact wideband VHF antennas (and also improve the efficiency of the inversion approach) was described. Similar to optimizing the distribution of the measurement points, figuring out the optimal frequency selection is another interesting problem to explore.

6.3 Contributions

This dissertation has resulted in the following contributions:

Refereed Journal Articles

1) ***Fikadu T Dagefu*** and Kamal Sarabandi, "Analysis and Modeling of Near-Ground Wave Propagation in the Presence of Building Walls," *IEEE Trans. on Antennas and Propagation* Vol. 59, no. 6, June 2011

2) ***Fikadu T Dagefu***, Jungsuek Oh and Kamal Sarabandi, "A Sub-wavelength RF Source Tracking System for GPS-denied Environments," *IEEE Trans. on Antennas and Propagation* (Accepted)

3) ***Fikadu T Dagefu*** and Kamal Sarabandi, "High Resolution Subsurface Imaging of Deeply Submerged Targets Based on Distributed Near-Ground Sensors," *IEEE Trans. on Geoscience and Remote Sensing* (Under review)

4) Jungsuek Oh, Jihun Choi, ***Fikadu T Dagefu*** and Kamal Sarabandi, "Extremely Small Two-Element Monopole Antenna for HF Band Applications," *IEEE Trans. on Antennas and Propagation* (Under review)

5) ***Fikadu T Dagefu***, Jungsuek Oh, Jihun Choi and Kamal Sarabandi, "Measurements and Physics-based Simulations of Co-polarized Near-Ground Radiation Pattern Diversity System," *IEEE Trans. on Antennas and Propagation* (to be submitted)

Conference Papers/Presentations

6) ***Fikadu T Dagefu***, DaHan Liao, Kamal Sarabandi, "An Efficient model for near-ground wave propagation in the presence of building walls/indoor obstacles," *Proc. IEEE Int. Antennas and Prop. & URSI Symposium*, Charleston, SC, June, 2009

7) ***Fikadu T Dagefu***, Kamal Sarabandi, "High resolution subsurface imaging of deep targets based on distributed sensor networks," *Proc. IEEE Int. Geosc. and Remote Sensing Symp.*, Cape town, South Africa, July, 2009

   – Selected as a top 10 Finalist in the symposium student paper competition.

8) ***Fikadu T Dagefu***, Kamal Sarabandi, "Soil dielectric and Sensitivity Analysis for subsurface imaging applications based on distributed sensor networks," *Proc. IEEE Int. Geosc. and Remote Sensing Symp.*, Honolulu, Hawaii, July, 2010

   – Selected as a top 10 Finalist in the symposium student paper competition.

9) ***Fikadu T Dagefu***, Kamal Sarabandi,"Simulation and measurement of near-ground wave propagation for indoor Scenarios," *Proc. IEEE Int. Antennas and Propagation & URSI Symp.*, Toronto, Ontario, Canada, July, 2010

10) ***Fikadu T Dagefu***, Kamal Sarabandi, "A 3D Subsurface imaging technique based on distributed near-ground sensors: investigation using scale model measurements," *Proc. IEEE Int. Geosc. and Remote Sensing Symp.*, Vancouver, Canada, July, 2011

11) ***Fikadu T Dagefu***, Jungsuek Oh, Kamal Sarabandi,"Numerical and Experimental Investigation of Source Tracking in Multipath Environments," *Proc. IEEE Int. Antennas and Propagation & URSI Symp.*, Spokane, WA, July, 2011

12) ***Fikadu T Dagefu***, Kamal Sarabandi, "A Subsurface Imaging Approach Based On Near-Ground Sensor Networks Utilizing Ultra-Wideband Near-Field Focusing," *USNC-URSI National Radio Science Meeting*, Boulder, Colorado, January, 2011

13) ***Fikadu T Dagefu***, Kamal Sarabandi, "A Sub-wavelength RF Source Tracking Device for GPS-denied Environments," *USNC-URSI National Radio Science Meeting*, Boulder, Colorado, January, 2012

14) ***Fikadu T Dagefu***, Kamal Sarabandi, "An Efficient Indoor Wave Propagation Model for Analysis of near-Ground Radiation Diversity Antennas," *Proc. IEEE Int. Antennas and Propagation & URSI Symp.*, Chicago, IL, July, 2012

15) ***Fikadu T Dagefu***, Kamal Sarabandi, "Simulation and Scale model Measurements for the detection and localization of tunnels," *Proc. IEEE Int. Geosc. and Remote Sensing Symp.*, Munich, Germany, July, 2012

APPENDICES

APPENDIX A

Functions used for calculation of $\overline{\overline{G}}_{00}$ for a half-space and two-layer dielectric medium

In this section, the expressions for $f_{ij}(w)$ used to compute the various components of the scattered field from a half-space dielectric are given.

$$E_{ij}^{scat} \simeq \frac{-k_o^3 \eta_o I_o l_i}{8\pi} e^{ik_o\rho}[\frac{f_{ij}(w_s)}{ik_o\rho} + \frac{\frac{f_{ij}''(w_s)}{2} + \frac{f_{ij}(w_s)}{8}}{(ik_o\rho)^2}],$$

Where,

$$f_{xx}(w) = (\sin w)^{1/2} \cos w[R_-(w) - R_+(w)\cos(2\phi)],$$

$$f_{xy,yx}(w) = -(\sin w)^{1/2} \cos w R_+(w) \sin(2\phi),$$

$$f_{xz}(w) = \frac{2}{k_o}(\sin w)^{3/2} \cos w R_{TM}^{01}(w) \cos\phi,$$

$$f_{yy}(w) = (\sin w)^{1/2} \cos w[R_-(w) + R_+(w)\cos(2\phi)],$$

$$f_{yz}(w) = \frac{2}{k_o}(\sin w)^{3/2}\cos w R_{TM}^{01}(w)\sin\phi,$$

$$f_{zx}(w) = -\frac{2}{k_o}(\sin w)^{3/2}\cos w R_{TM}^{01}(w)\cos\phi,$$

$$f_{zy}(w) = -\frac{2}{k_o}(\sin w)^{3/2}\cos w R_{TM}^{01}(w)\sin\phi,$$

$$f_{zz}(w) = \frac{2}{k_o}(\sin w)^{5/2} R_{TM}^{01}(w).$$

The reflection coefficients $(R_{TE}, R_{TM}, R_{\pm})$ are given below:

$$R_{TE}^{mn}(w) = \frac{\sqrt{\epsilon_{rm} - \sin^2 w} - \sqrt{\epsilon_{rn} - \sin^2 w}}{\sqrt{\epsilon_{rm} - \sin^2 w} + \sqrt{\epsilon_{rn} - \sin^2 w}},$$

$$R_{TE}^{mn}(w) = \frac{\epsilon_{rn}\sqrt{\epsilon_{rm} - \sin^2 w} - \epsilon_{rm}\sqrt{\epsilon_{rn} - \sin^2 w}}{\epsilon_{rn}\sqrt{\epsilon_{rm} - \sin^2 w} + \epsilon_{rm}\sqrt{\epsilon_{rn} - \sin^2 w}},$$

$$R_{\pm}(w) = \frac{R_{TE}^{01}(w)}{k_o \cos w} \pm \frac{\cos w R_{TM}^{01}(w)}{k_o}.$$

APPENDIX B

Expressions for UHF soil-dielectric model

The expressions for the real ($\epsilon_r^{'}$) and imaginary ($\epsilon_r^{''}$) parts of the dielectric constants are given by

$$\epsilon_r^{'} = [1 + \frac{\rho_b}{\rho_s}(\epsilon_s^{\alpha} - 1) + mv^{\beta^{'}} \epsilon_{fw}^{'\ \alpha} - mv]^{\frac{1}{\alpha}},$$

$$\epsilon_r^{''} = [mv^{\beta^{''}} \epsilon_{fw}^{''\ \alpha}]^{\frac{1}{\alpha}},$$

where, ρ_s is the specific density of solid particles in $\frac{g}{cm^3}$ and ρ_b is bulk density also in $\frac{g}{cm^3}$. $\beta^{'}$, $\beta^{''}$ and α, are empirically determined based on data taken in the UHF range. $\beta^{'}$, $\beta^{''}$ and σ_{eff} (which is the effective conductivity of soil mixture) are related to fraction of sand (S) and fraction of sand (C) by

$$\beta^{'} = 127.48 - 0.519S - 0.152C,$$

$$\beta^{''} = 1.338 - 0.603S - 0.166C,$$

$$\sigma_{eff} = 0.0467 - 0.2204\rho_b - 0.4111S - 0.6614C,$$

where, τ_w is relaxation time for water and f is frequency. The real and imaginary parts of the dielectric constant of water ($\epsilon_{fw}^{'}$ and $\epsilon_{fw}^{''}$, respectively) are given as

$$\epsilon_{fw}^{'} = \epsilon_{w\infty} + \frac{\epsilon_{w0} - \epsilon_{w\infty}}{1 + (2\pi f\tau_w)^2},$$

$$\epsilon_{fw}^{''} = 2\pi f\tau_w \frac{\epsilon_{w0} - \epsilon_{w\infty}}{1 + (2\pi f\tau_w)^2} + \frac{\sigma_{eff}}{2\pi\epsilon_0\tau_w}\frac{\rho_s - \rho_s}{\rho_b},$$

where, ϵ_{w0} and $\epsilon_{w\infty}$ is the static dielectric constant of water and the high-frequency limit of the real part of the dielectric constant of water, respectively.

BIBLIOGRAPHY

BIBLIOGRAPHY

[1] Andria van der Merwe and Inder J. Gupta, "A Novel Signal Processing Technique for Clutter Reduction in GPR Measurements of Small, Shallow Land Mines," *IEEE Trans. on Geosc. and Remote Sens.*, Vol. 38, No. 6, Nov. 2000

[2] Hakan Brunzell, "Detection of Shallowly Burried Objects Using Impulse Radar," *IEEE Trans. on Geosc. and Remote Sens.*, vol. 37, No. 2, Mar. 1999

[3] Paul D. Gader,Miroslaw Mystkowski and Yunxin Zhao, "Landmine Detection with Ground Penetrating Radar Using Hidden Markov Models," *IEEE Trans. on Geosc. and Remote Sens.*, vol. 39, No. 6, June. 2001

[4] [Online]. Available: http://www.militarynewsnetwork.com/magazine/february2011.htm

[5] [Online]. Available: http://www.mast-cta.org/

[6] [Online].Available:http://land-affairs.typepad.com/tanzania/land-alienation/

[7] Mojtaba Dehmollaian and Kamal Sarabandi, "Refocusing Through Building Walls Using Synthetic Aperture Radar," *IEEE Trans. Geosci. Remote Sens.*, vol. 46, no. 6, June 2004

[8] Michael Thiel and Kamal Sarabandi, "Analysis of human backscattering in buildings for through-wall radar applications," *in Proc. IEEE Antennas and Propagation Society Int. Symp*, June 2009

[9] [Online]. Available: http://www.globalsecurity.org/military/systems/munitions/shm.htm

[10] [Online]. Available: http://www.darpa.mil/ipto/programs/nest/nest.asp

[11] W. M. Merrill, H. L. N. Liu, J. Leong, K. Sohrabi and G. J. Pottie, "Quantifying Short-Range Surface-to-Surface Communications Links," *IEEE Antennas and Propagation Magazine*, Vol. 46, NO. 3, June 2004

[12] J. W. McKown, R.Lee Hamilton, Jr., "Ray Tracing as a Design Tool for Radio Networks", *IEEE Network Megazine* , Vol. 5, Issue 6, Nov 1991

[13] R. A. Valenzuela, "A ray tracing approach to predicting indoor wireless transmission," *IEEE Trans. on vehicualr technology*, May 18-20, 1993

[14] F. Aryanfar and Kamal Sarabandi, "3-D Wave Propagation Simulation in Complex Indoor Structures," *in Proc. IEEE Antennas and Propagation Society Int. Symp*, June 2004

[15] M. Hassan-Ali and K. Pahlavan, "A new statistical model for site-specific indoor radio propagation prediction based on geometric optics and geometric probability," *IEEE Trans. Wireless Communications*, vol. 1, Jan. 2002

[16] F. A. Alves, M. R. M. L. Albuquerque, S. G. Silva, A. G. d'Assuno "Using efficient ray tracing techniques to predict propagation losses in indoor environments", *Microwave and Optical Technology Letters*, Vol. 49, No. 4, April 2007

[17] V. Erceg, S.J. Fortune, J. Ling, A.J. Rustako Jr., R.A. Valenzuela, "Comparisons of a Computer-Based Propagation Prediction Tool with Experimental Data Collected in Urban Microcellular Environments", *IEEE Journal on Selected Areas in Communications*, Vol. 15, No. 4, May 1997, pp.677-684.

[18] G.E. Athanasiadou, A.R. Nix, J.P. McGeehan, "A Microcellular Ray Tracing Propagation Model and Evaluation of its Narrow-Band and Wide-Band Predictions", *IEEE Journal on Selected Areas in Communications*, Vol. 18, No. 3, March 2000, pp. 322-335.

[19] S. Loredo, L. Valle, R.P. Torres. "Accuracy Analysis of GO/UTD Radio-Channel Modeling in Indoor Scenarios". *IEEE Antennas and Propagation Magazine*, Vol. 42, No.5, October 2001, pp. 37-51.

[20] Z. Zhang, Rory K. Sorensen, Zhengqing Yun, Magdy F. Iskander and J. F. Harvey, "A ray Tracing Approach for Indoor/Outdoor Propagation Through Window Structures". *IEEE Trans. Antennas Propag.*, Vol. 50, No.5, May 2002

[21] K. A. Remley, Harry R. Anderson, and Andreas Weisshar, "Improving the Accuracy of Ray Tracing Techniques for Indoor Propagation Modeling". *IEEE Trans. on vehicualr technology*, Vol. 49, No.6, November 2000

[22] F. Saez de Adana, Oscar Gutirrez Blanco, Ivn Gonzlez Diego, Jess Prez Arriaga, and Manuel F. Ctedra, "Propagation Model Based on Ray Tracing for the Design of Personal Communication Systems in Indoor Environments". *IEEE Trans. on vehicualr technology*, Vol. 49, No.6, May 2000

[23] M. Thiel and Kamal Sarabandi, "3D-Wave Propagation Analysis of Indoor Wireless Channels Utilizing Hybrid Methods", *IEEE Trans. Antennas Propag.*, vol. 57, no. 5, may 2009.

[24] R. Janaswamy, "Path Loss Predictions in the Presence of Buildings on Flat Terrain: A 3-D Vector Parabolic Equation Approach", *IEEE Trans. Antennas and Propag.*, vol. 51, no. 8, May 2003.

[25] S. Y. Tan and H. S. Tan, "UTD propagation model in an urban street scene for microcellular communications," *IEEE Trans. Electromag. Compat.*, vol. 35, Nov. 1993.

[26] R. J. Luebbers, "Finite conductivity uniform GTD versus knife edge diffraction in prediction of propagation path loss," *IEEE Trans. Antennas Propag.*, vol. AP-32, pp. 70-76, Jan. 1984.

[27] R. G. Kouyoumjian and P. H. Pathak, "A uniform geometric theory of diffraction for an edge on a perfectly conducting surface," *Proc. IEEE*, vol. 62, Nov. 1974.

[28] T. B. Gibson and David C. Jenn, "Prediction and Measurement of Wall Insertion Loss", *IEEE Trans. Antennas and Propag.*, Vol. 47, No. 1, January 1999

[29] F. Van Der Wijk, A. Kegel, and R. Prasad, "Assessment of a Pico-Cellular System Using Propagation Measurements at 1.9 GHz for Indoor Wireless Communications", *IEEE Trans. Veh. Technol.*, Vol. 44, Feb. 1995

[30] K.-W. Cheung, Jonathan H.-M. Sau, and R. D. Murch, "A New Empirical Model for Indoor Propagation Prediction," *IEEE Trans. on vehicualr technology*, vol. 47, no. 3, august 1998

[31] A. Hugine, H.I. Volos, J. Gaeddert, R.M. Buehrer, "Measurement and characterization of the near-ground indoor ultra wideband channel, " *Wireless communications and networking conference*, 2006

[32] M. Hata, Empirical Formula for Propagation Loss in Land Mobile Radio Service, *IEEE Transactions on Vehicular Technology*, VT-29,3, 1980, pp. 317-325.

[33] J. B. Andersen, Theodore 5. Rappaport, and Susumu Yoshida, "Propagation Measurements and Models for Wireless Communications Channels," *IEEE Communications Magazine*, January 1995

[34] Q. H. Spencer, Brian D. Jeffs, Michael A. Jensen, and A. Lee Swindlehurst, "Modeling the Statistical Time and Angle of Arrival Characteristics of an Indoor Multipath Channel" *IEEE Journal on Selected areas in communications*, vol. 18, no. 3, March 2000

[35] T. Li, A. Ekpenyong and Y.-F Huang, "Source Localization and Tracking Using Distributed Asynchronous Sensor," *IEEE Trans. on Signal processing, Vol. 54, no. 10, Oct. 2006.*

[36] [Online]. Available: http://www.crfs.com/technology/direction-finding/

[37] Z. Wang and S.A. Zekavat, "Manet Localization Via Multi-Node TOA-DOA Optimal Fusion," *IEEE Military Communications Conference*, 2006

[38] B. N. Hood and P. Barooah, "Estimating DoA From Radio-Frequency RSSI Measurements Using an Actuated Reflector," *IEEE Sensors Journal*, vol. 11, no. 2, 2011

[39] H. Liu, H. Darabi, P. Banerjee and J. Liu, "Survey of Wireless Indoor Positioning Techniques and Systems," *IEEE Trans. On Systems, Man, and Cybernetics-Part C: Applications and Reviews*, vol. 37, no. 6, Nov. 2007

[40] A. H. El Zooghby, C. G. Christodoulou and M. Georgiopoulos, "A Neural Network-Based Smart Antenna for Multiple Source Tracking," *IEEE Trans. Antennas Propag.*, vol. 48, no. 5, Nov. 2000

[41] Y. Wang and G. Leus and H. Delic, "TOA Estimation Using UWB with Low Sampling Rate and Clock Drift Calibration," *IEEE Inte. Conf. on Ultra-Wideband*, 2009.

[42] P.Z. Alba, V. Josep, and D.H. Brooks, "Closed-Form Solution for Positioning Based on Angle of Arrival Measurements," *Proc. 13th IEEE Intl Symp. Personal Indoor Mobile Radio Comm.* , vol. 4, 2002.

[43] Fabio Belloni, Ville Ranki, Antti Kainulainen and Andreas Richter, "Angle-based Indoor Positioning System for Open Indoor Environments," Proceedings of the 6th workshop on positioning,navigation and communication, 2009

[44] L. Cong and W.H. Zhuang, "Hybrid TDOA/AOA Mobile Users Location for Wideband CDMA Cellular Systems," *IEEE Trans. Wireless Comm.*, vol. 1, July 2002.

[45] C.-D Wann,Y.-J Yeh and C.-S Hsueh, "Hybrid TDOA/AOA Indoor Positioning and Tracking Using Extended Kalman Filters," *IEEE Conference On Vehicular Technology*, September 2006

[46] W.T. Barnett, "Multipath Propagation at 4,6, and 11GHz," *Bell System Technical Journal*, vol. 51, no. 2, February 1972

[47] C.L. Ruthroff, "Multiple-Path Fading on Line-of-Sight Microwave Radio Systems as a function of Path Length and Frequency," *Bell System Technical Journal*, vol. 50, no. 7, September 1971

[48] C. Morelli, M. Nicoli, V. Rampa and U. Spagnolini, "Hidden Markov Models for Radio Localization in Mixed LOS/NLOS Condition," *IEEE Trans on Signal Processing*, vol. 55, no. 4, April 2007

[49] C. K. Seow and S. Y. Tan, "Non-Line-of-Sight Localization in Multipath Environments," *IEEE Trans. On Mobile Computing*, vol. 7, no. 5, May 2008

[50] D.E. Gustafson, M.S. Bottkol, J.R. Parry, J.M. Elwell and T.Q Nguye, "Indoor Geolocation Using RF Multipath With Probabilistic Data Association," *IEEE Location and Navigation Symposium,* May 2008

[51] S. L. Cotton and W. G. Scanlon, Bhopinder K. Madahar, "Millimeter-Wave Soldier-to-Soldier Communications for Covert Battlefield Operation," *IEEE Communications Magazine*, vol.47, no. 10, 2009

[52] M. K. Kaise, N. R. Gans and W. E. Dixon, "Vision-Based Estimation for Guidance, Navigation, and Control of an Aerial Vehicle," *IEEE Transactions On Aerospace and Electronic Systems*, vol. 46, no. 3, July 2010

[53] W.-H Liau, C.-L Wu and L.-C Fu, "Inhabitants Tracking System in a Cluttered Home Environment Via Floor Load Sensor," *IEEE Trans. On Automation Science and Engineering*, vol. 5, no. 1, January 2008

[54] D. L. Moffat and R. J. Puskar, "A Subsurface Electromagnetic Pulse Radar," *Geophysics*, 41, June 1976, pp. 506-518.

[55] N. Osumi and K. Ueno, "Microwave Holographic Imaging of Underground Objects," *IEEE Trans. on Ant. and Prop.*, AP-33, Feb. 1985

[56] G. S. Smith and W. R. Scott, Jr., "A Scale Model for Studying Ground Penetrating Radars," *IEEE Transactions on Geosc. and Remote Sens.*, Vol 27, No. 4, July 1989

[57] C. Liu and C. Shen, "Numerical Simulation of Subsurface Radar for Detecting Buried Pipes," *IEEE Trans. on Geosc. and Remote Sens.*, Vol. 29, No. 5, Sept. 1991

[58] L. Carin, N. Geng, M. McClure, J. Sichina, and L. Nguyen, Ultra-wideband synthetic-aperture radar for mine-field detection," *IEEE Antennas Propag. Mag.*, vol. 41, no. 1, Feb. 1999.

[59] T. J. and Z. Zho, "Refraction and Dispersion Effects Compensation for UWB SAR Subsurface Object Imaging," *IEEE Trans. Geosci. Remote Sens.*, Vol.45, No. 12, March 2007

[60] A. Sullivan, R. Damarla, N. Geng, Y. Dong and L. Carin, "Ultrawide-Band Synthetic Aperture Radar for Detection of Unexploded Ordnance: Modeling and Measurements," *IEEE Trans. on Ant. and Prop.*, vol. 48, no. 9, Sept. 2000

[61] A. J. Witten, J. E. Molyneux and J. E. Nyquist, "Ground Penetrating Radar Tomography: Algorithms and Case Studies," *IEEE Trans. Geosci. Remote Sens.*, Vol.32, No. 2, Mar. 1994

[62] J. M. Bourgeois and G. S . Smith, "A Fully Three-Dimensional Simulation of Ground Penetrating Radar: FDTD Theory Compared with Experiment," *IEEE Transactions on Geoscience and Remote Sensing*, Vol. 34, No. 1, Jan. 1999.

[63] R. W. P. King and C. W. Hamson, Jr., "The Transmission of Electromagnetic Waves and Pulses into the Earth," *Journal of Applied Physics*, Vol. 39, No. 1, Aug. 1968

[64] A. Witten, I. J. Won and S. J. Norton, "Subsurface imaging with broadband electromagnetic induction," Inverse Problems, vol.13,no.6, August 1997

[65] T. Counts,A. Cafer Gurbuz, W. R. Scott, Jr, James H McClellan and Kandwook Kim, "Multistatic Ground Penetrating Radar Experiments," *IEEE Trans. Geosci. Remote Sens.*, vol.45, no. 8, August 2007

[66] R. Firoozabadi, E. L. Miller, C. M. Rappaport, and Ann W. Morgenthaler , "Subsurface Sensing of Buried Objects Under a Randomly Rough Surface Using Scattered Electromagnetic Field Data," *IEEE Trans. Geosci. Remote Sens.*, Vol. 45, No. 1, January 2007

[67] J. Fortuny-Guasch, "A Novel 3-D Subsurface Radar Imaging Technique," *IEEE Trans. Geosci. Remote Sens.*, vol. 40, No. 2, February 2002

[68] R. D. Brown, D. D. Mokry, J. M. VanDamme, M. C. Wicks, "Experimental HF radar for subsurface sensing," *7th International Conference on Ground-Penetrating Radar*, May, 1998

[69] S. Y. Semenov, A. E. Bulyshev, A. Abubakar,V. G. Posukh, Y. E. Sizov, Alexander E. Souvorov, Peter M. van den Berg, and Thomas C. Williams, "Microwave-Tomographic Imaging of the High Dielectric-Contrast Objects Using Different Image- 25 Reconstruction Approaches," *IEEE Trans. on Microwave theory And techniques*, Vol. 53, No. 7, July 2005

[70] L. Carin, J. Sichina, and J. F. Harvey, "Microwave Underground Propagation and Detection," *IEEE Trans. Microwave theory and techniques*, Vol. 50, No. 3, March 2002

[71] A. Khaleghi, "Diversity Techniques with parallel dipole antennas: radiation pattern analysis," *Progress in Electromagnetics Research*, PIER 64,23-42,2006

[72] J. S. Colburn, Y. Rahmat-Samii, M. A. Jensen, and G. J. Pottie, "Evaluation of personal communications dual-antenna handset diversity performance," *IEEE Trans. Veh. Technol.*, vol. 47, pp. 737-744, Aug. 1998.

[73] R. Narayanan, K. Atanassov, V. Stoiljkovic, and G. Kadambi, "Polarization Diversity Measurements and Analysis for Antenna Configurations at 1800 MHz," *IEEE Trans. on ant. and prop.*, vol. 52, no. 7, July 2004

[74] C. B. Dietrich, Jr., K. Dietze, J. R. Nealy and W. L. Stutzman, "Spatial, Polarization, and Pattern Diversity for Wireless Handheld Terminals," *IEEE Trans. on ant. and prop.*, vol. 49, no. 9, Sept. 2001

[75] J. Sarrazin, Y. Mah, S. Avrillon, and S. Toutain, "Collocated Microstrip Antennas for MIMO Systems With a Low Mutual Coupling Using Mode Confinement, " *IEEE Trans. on ant. and prop.*, vol. 58, no. 2, Feb. 2010

[76] A. M. D. Turkmani, A. A. Arowojolu, P. A. Jefford, and C. J. Kellet, An experimental evaluation of the performance of two-branch space and polarization diversity schemes at 1800 MHz, IEEE Trans. Veh. Technol., vol. 44, Mar. 1995

[77] P. L. Perini and C. L. Holloway, "Angle and Space Diversity Comparisons in Different Mobile Radio Environments," *IEEE Trans. on ant. and prop.*, vol. 46, no. 6, June 1998

[78] P. Mattheijssen, M. H. A. J. Herben, G. Dolmans, and L. Leyten, "Antenna-Pattern Diversity Versus Space Diversity for Use at Handhelds," *IEEE Trans. Veh. Technol.*,vol. 53, no. 4, July 2004

[79] A. Elsherbini and K. Sarabandi, "UWB High-Isolation Directive Coupled-Sectorial-Loops Antenna Pair," *IEEE Antennas and Wireless Propagation letters*, vol. 10, 2011

[80] Kamal Sarabandi, Mark D. Casciato, and Il-Suek Koh, "Efficient Calculation of the Fields of a Dipole Radiating above an Impedance Surface," *IEEE Trans. Antennas Propag.*, vol. 50, no. 9, Sept. 2002

[81] W. C. Chew and J. A. Kong, "Electromagnetic field of a dipole on a two-layer earth, " *Geophysics* vol. 46. no 3 march 1981

[82] T. TAMIR, "Radio Wave Propagation Along Mixed Paths in Forest Environments, " *IEEE Trans. Antennas Propag.*, vol. 25, no. 4, July 1977

[83] DaHan Liao, and Kamal Sarabandi, "Near-Earth Wave Propagation Characteristics of Electric Dipole in Presence of Vegetation or Snow Layer," *IEEE Trans. Antennas Propag.*, vol. 53, no. 11, Nov. 2005

[84] K. A. Norton, "The Calculation of Ground-Wave Field Intensity Over a Finitely Conducting Spherical Earth," *Proceeengs of the IRE* , December 1941, pp. 23-39.

[85] James R. Wait, "The Ancient and Modem History of EM Ground-Wave Propagation," IEEE Antennas and Propagation Magazine, 40, 5, October 1998, pp. 7-24.

[86] Krzysztof A. Michalski and Juan R. Mosig, "Multilayered Media Greens Functions in Integral Equation Formulations," *IEEE Trans. Antennas Propag.*, vol. 45, no. 3, March 1997

[87] Chang-Fa Yang, Chuen-Jyi Ko, and Boau-Cheng Wu, "A Free Space Approach for Extracting the Equivalent Dielectric Constants of the Walls in Buildings," *in Proc. IEEE Antennas and Propagation Society Int. Symp*, vol. 2.1996

[88] Daniel Pea, Rodolfo Feick, Hristo D. Hristov and Walter Grote, "Measurement and Modeling of Propagation Losses in Brick and Concrete Walls for the 900-MHz Band," *IEEE Trans. Antennas and Propag.*, vol. 51, no. 1, Jan 2003.

[89] DaHan Liao and Kamal Sarabandi, "Simulation of Near-Ground Long-Distance Radiowave Propagation Over Terrain Using Nystrm Method With Phase Extraction Technique and FMM-Acceleration" *IEEE Trans. Antennas and Propag.*, vol. 57, no. 12, Dec 2009.

[90] F. T. Dagefu and Kamal Sarabandi, "Analysis and Modeling of Near-ground Wave Propagation in the Presence of Building Walls," *IEEE Trans. Antennas Propag.*, vol. 59, no. 6, June. 2011

[91] J. Oh and K. Sarabandi, "A low-profile Omnidirectional planar antenna with vertical polarization employing two in phase elements," *General Assembly and Scientific Symposium*, 2011 XXXth URSI, pp. 1-4

[92] Jungsuek Oh, Jihun Choi, Fikadu T Dagefu and Kamal Sarabandi, Extremely Small Multi-Element Monopole Antenna With Enhanced Gain IEEE Trans. Antennas Propagation (Under review)

[93] M. Akcakaya and A. Nehorai, "Performance analysis of the Ormia ochracea's coupled ears," *J. Acoust. Soc.* Am. 124, October 2008

[94] Miles RN, Robert D, Hoy RR., "Mechanically coupled ears for directional hearing in the parasitoid fly Ormia ochracea," J Acoust. Soc Am. 1995 Dec;98(6):3059-70.

[95] N. Behdad, M. A. Al-Joumayly and M. Li, "Biologically Inspired Electrically Small Antenna Arrays With Enhanced Directional Sensitivity," *IEEE Antennas and wireless Prop. letters*, vol. 10, April 2011

[96] [Online]. Available: http://www.sorrac.com

[97] [Online]. Available: http://www.rohde-schwarz.us

[98] Neil R. Peplinski, Fawwaz T. Ulaby, and Myron C. Dobson ,"Dielectric Properties of Soils in the 0.3-1.3-GHz Range," *IEEE Trans. Geosci. Remote Sens.*, Vol.33, No. 3, May. 1994

[99] F. T. Ulaby, Richard K. Moore, and Adrian K. Fung, "Microwave remote sensing-Active and passive," Feb,1982

[100] J. O. Curtis, "Moisture Effects on the Dielectric Properties of Soils," *IEEE Trans. Geosci. Remote Sens.*, Vol. 39, No. 1, January 2001

[101] M. T. Hallikainen, F. T. Ulaby, M. C. Dobson, M. A. El-Rayes, and Lin-Kun Wu, "Microwave Dielectric Behavior of Wet Soil-Part I: Empirical Models and Experimental Observations," *IEEE Trans. Geosci. Remote Sens.*, Vol. GE-23, No. 1, January 1985

[102] M. C. Dobson, F. T. Ulaby, M. T. Hallikainen, and M. A. El-Rayes, Microwave Dielectric Behavior of Wet Soil-Part II: Dielectric Mixing Models, *IEEE Trans. Geosci. Remote Sens.*, Vol. GE-23, No. 1, January 1985

[103] W. J. Chudobiak, Barry A. Syrett and H.M. Hafez, "Recent Advances in Broad-Band VHF and UHF Transmission Line Methods for Moisture Content and Dielectric Constant Measurement," *IEEE Trans. on Instrumentation and measurement*, vol. IM-28, no. 4, Dec. 1979

[104] D. Wobschall, "A Theory of the Complex Dielectric Permittivity of Soil Containing Water: The Semidisperse Model," *IEEE Transactions On Geoscience Electronics*, January 1977

[105] J.E. Hipp, "Soil Electromagnetic Parameters as Functions of Frequency,Soil Density, and Soil Moisture," *proceedings of IEEE*, January 1974

[106] D. Liao, and Kamal Sarabandi, "Terminal-to-Terminal Hybrid Full-Wave Simulation of Low-Profile, Electrically-Small, Near-Ground Antenna," *IEEE Trans. Antennas Propag.*, vol. 56, no. 3, March 2008

[107] W. K. Toh, Z. N. Chen, X. Qing, and T. S. P. See, "A planar UWB diversity antenna," *IEEE Trans. on Ant. & Prop.*, vol. 57, no. 11, pp. 3467-3473, Nov. 2009.

[108] K. Wei, Z. Zhang, W. Chen, and Z. Feng, "A novel hybrid-fed patch antenna with pattern diversity," *IEEE Antennas Wireless Propag. Lett.*, vol. 9, pp. 562-565, 2010.

[109] K. Rosengren and P.-S. Kildal, "Radiation efficiency, correlation, diversity gain and capacity of a six-monopole antenna array for aMIMO system: theory, simulation and measurement in reverberation chamber," *IEE Proc.-Microw. Ant. Prop.* Vol. 152, No. 1, Feb. 2005

[110] M. Sonkki, E. Antonino-Daviu, M. Ferrando-Bataller and E. T. Salonen "Planar Wideband Polarization Diversity Antenna for Mobile Terminals," IEEE Ant. and Wireless Prop., Vol. 10, 2011

[111] M. Schwartz, W. R. Bennet and S. Stein, "Communication Systems and Techniques," *IEEE press*, 1996

[112] [Online].Available http://www.emagware.com/

[113] S. Blanch, J. Romeu, and I. Corbella, "Exact representation of antenna system diversity performance from input parameter description", *Electron. Lett.*, 2003, 39, pp. 705-707.

[114] T. K. George, N. Lenin , M. Sreenivasan "Wide-band dual sleeve antenna", *IEEE Trans. on Ant. & Prop.*, 2006, vol. 54